



FACHBEREICH MATHEMATIK UND NATURWISSENSCHAFTEN
FACHGRUPPE PHYSIK
BERGISCHE UNIVERSITÄT WUPPERTAL

Track Reconstruction in the ATLAS Experiment
The Deterministic Annealing Filter

Diplomarbeit
von
Sebastian Fleischmann

Contents

1	Introduction	1
2	Physics at hadron colliders	3
2.1	The Standard Model of particle physics	3
2.2	Physics beyond the Standard Model	5
3	The ATLAS Experiment	7
3.1	Aims and Design concepts	7
3.2	Inner Detector	9
3.2.1	Pixel Detector	11
3.2.2	Silicon-Strip-Detector (Semiconductor Tracker, SCT)	11
3.2.3	Straw Tube Detector using Transition Radiation (TRT)	12
3.3	Calorimeter	13
3.4	Muon Spectrometer	14
4	Track reconstruction	15
4.1	Pattern recognition	15
4.2	Track parameterization	17
4.3	Estimation of track states	18
4.3.1	Global χ^2 fits	19
4.3.2	Recursive track fitting: The Kalman filter	19
4.4	Adaptive track fitting methods	23
4.4.1	Elastics Arms and Elastic Tracking Algorithms	24
4.4.2	Deterministic Annealing Filter	26
4.4.3	Multi-Track-Fitter	30
5	Software Implementation	31
5.1	The ATLAS reconstruction framework ATHENA	31
5.2	Inner Detector track reconstruction	32
5.2.1	Extrapolation process and track representation	33
5.3	Deterministic Annealing Filter implementation	35
5.4	Extension of silicon tracks into the TRT using deterministic annealing .	38
5.5	ATLAS fast track simulation fatRas	41
5.5.1	Track simulation	42

5.5.2	Noise creation	43
5.6	Further validation tools	44
6	Validation and performance studies	47
6.1	Refitting of tracks in the Inner Detector	48
6.2	Performance of the TRT local pattern recognition in fatRas simulated events	52
6.2.1	Improvements of the implementation: Cut in straw direction for TRT measurements	52
6.2.2	Impact of extrapolation problems	53
6.2.3	Initial roadwidth of the TRT extension algorithm	54
6.2.4	Intrinsic roadwidth and cut parameter λ	59
6.2.5	Modified normalization of assignment probabilities	61
6.2.6	Annealing Schedules	68
6.2.7	Noise Occupancy in the TRT	72
6.2.8	Momentum dependency and comparison of two kind of measurement groupings in the TRT	74
6.3	Performance tests with full simulation	76
7	Conclusion and Outlook	79
A	Details on the track reconstruction algorithms	81
A.1	Kalman filter in gain matrix formalism	81
A.2	Properties of assignment probabilities	81
B	Supplements to the DAF studies	85
B.1	List of extra packages used in the studies and reconstruction parameters	85
B.2	Additional figures	85
C	Reference of the developed ATHENA packages	93
C.1	Reconstruction algorithms	93
C.1.1	TrkDeterministicAnnealingFilter	93
C.1.2	TRT_TrackExtensionTool_DAF	93
C.1.3	TrkMeasurementUpdater	94
C.2	Event Data Model classes and their related tools	94
C.2.1	TrkCompetingRIOsOnTrack	94
C.2.2	TrkCompetingRIOsOnTrackTool	95
C.2.3	InDetCompetingRIOsOnTrack	95
C.2.4	InDetCompetingRIOsOnTrackTool	96
C.3	Validation tools	96
C.3.1	TrkValInterfaces	96
C.3.2	TrkValAlgs	97

C.3.3	TrkValTools	97
C.3.4	InDetTrackValidation	99
C.4	fatRas simulation	99
List of Figures		101
Abbreviations		103
Bibliography		105

1 Introduction

Particle physics studies the building blocks of matter and the interactions between them. In the last century a very detailed picture of the subatomic world was developed and a theory – the Standard Model of particle physics – exists which can explain nearly all observations made in this area. But one particle needed by the theory has not yet been observed and theoretical considerations suggest phenomena beyond the Standard Model. Many concurrent theories exist as extensions of the Standard Model needing new experimental observations to decide between them.

Modern experiments in high energy physics use huge colliders to accelerate particles and investigate the reaction products. ATLAS is one of the two general purpose detectors being built at the Large Hadron Collider (LHC) in Geneva, Switzerland. The inner part of the detector consists of a tracking system for the measurement of the trajectories of charged particles.

The tracking system is structured in layers which measure the positions where the particle trajectories intersect those layers. The physics analysis on the other hand mainly needs the momentum and direction of the particle at the estimated creation or reaction point, or even better the four-momentum of the particle. It is therefore needed to determine these parameters from the initial measurements. This is part of the so-called *track reconstruction* process.

Powerful track reconstruction is particularly important for experiments at the LHC. Due to the high frequency of bunch crossings and the high luminosity several events will be observed in the detectors at the same time. The proton-proton collisions additionally produce underlying particle jets which increase the track multiplicity further. The LHC experiments will search for new particles and processes in energy ranges which have not been accessible by accelerators yet. One therefore has to deal with high backgrounds while even small deficits or artifacts can reduce the signal or may produce additional background after event selection.

The track reconstruction does not only contain the estimation of the track parameters, but also a pattern recognition deciding which measurements belong to a track and how many particle tracks can be found. Track reconstruction at ATLAS suffers from the high event rate at the LHC resulting in a high occupancy of the tracking devices. Additionally one part of the inner tracker, the so-called Transition Radiation Tracker (TRT), shows a left/right ambiguity for each measurement which has to be solved during local pattern recognition.

A special algorithm was developed in 1999 to handle noise and ambiguities during the track fit. The *Deterministic Annealing Filter* extends the frequently used Kalman

Filter with the concept of competition between measurements. Furthermore an annealing process is introduced to avoid local optima of measurement assignment and track fit. The DAF can therefore help to reduce limitations of the track reconstruction performance, e. g. at high noise levels and dense jets. This algorithm was implemented in the ATLAS offline reconstruction software within this thesis. The performance of the algorithm was studied and results are presented.

2 Physics at hadron colliders

All experiments in high energy physics are guided by the fundamental questions, what the building blocks of matter are and which rules their interactions describe. The Standard Model of particle physics is the current view of the microscopic world. It has been very successful over the last decades to explain almost all observed phenomena in particle physics. It does not contain effects of gravity, though, which is one reason why theorists believe that the Standard Model can only be part of a larger theory. On the other hand gravity effects are extremely small in the environment of particle physics and can usually be neglected. The experiments currently under construction are expected to find the last missing particle of the Standard Model and very likely hints on physics beyond.

2.1 The Standard Model of particle physics

This chapter will give a short phenomenological introduction into the Standard Model of particle physics. It is only meant as an overview of the basic concepts, a more detailed presentation can e.g. be found in [AH03] and [AH04].

The Standard Model of particle physics is basically a combination of two theories, Quantum Chromodynamics (QCD) and the electro-weak theory. Both belong to the group of Quantum Field Theories (QFT), which are enhancements and a combination of quantum mechanics and relativistic field theory.

A basic principle of each Quantum Field Theory are gauge symmetries. From classical electrodynamics (see e. g. [Jac02]) gauge transformations are well known. For example one can add an arbitrary constant to the electric potential and therefore “gauge” the potential without changing the physical properties of the related electromagnetic field. A theory, given by a set of equations of motion, shows a gauge symmetry, if one solution of the theory is transformed into a new solution for each member of a group of gauge transformations.

The concept gets even more important, because it follows from NOETHER’s theorem that every symmetry of a theory is connected to a constant of motion. Conserved quantities on the other hand are very important for phenomenological considerations.

In the Standard Model all building blocks of matter are fermions with spin $\frac{1}{2}$. Dirac deduced in 1928 the existence of antiparticles when he tried to generalize the Schrödinger wavefunction to relativistic quantum mechanics for spin- $\frac{1}{2}$ particles. Negative-energy solutions automatically arise in the extension, which he interpreted

as “holes” relative to the vacuum. Anti-particles therefore have the same mass and identical properties as their related particles, but the signs of electric charge and other quantum numbers are reversed. Anderson discovered the positron as the anti-particle of the electron in 1932. The data given about the fermions refers to the particles in the following.

The fermions in the Standard Model can be divided in three “families” of two leptons and two quarks each. The families are identical copies in their basic properties beside their mass. Each family can be seen as a doublet of quarks, one with electric charge $+2/3$ and one with $-1/3$ and a doublet of leptons, one with electric charge -1 and a related electrically neutral neutrino. The following table lists the Standard Model fermions including their masses (values taken from [Y⁺06]).

I mass/MeV		II mass/MeV		III mass/MeV		electrical charge
$\begin{pmatrix} \nu_e \\ e^- \end{pmatrix}$	$\begin{matrix} 0 \\ 0.511 \end{matrix}$	$\begin{pmatrix} \nu_\mu \\ \mu^- \end{pmatrix}$	$\begin{matrix} 0 \\ 105.66 \end{matrix}$	$\begin{pmatrix} \nu_\tau \\ \tau^- \end{pmatrix}$	$\begin{matrix} 0 \\ 1776.99^{+0.29}_{-0.26} \end{matrix}$	$\begin{matrix} 0 \\ -1 \end{matrix}$
$\begin{pmatrix} u \\ d \end{pmatrix}$	$\begin{matrix} 1.5 - 3.0 \\ 3 - 7 \end{matrix}$	$\begin{pmatrix} c \\ s \end{pmatrix}$	$\begin{matrix} 1250 \pm 90 \\ 95 \pm 25 \end{matrix}$	$\begin{pmatrix} t \\ b \end{pmatrix}$	$\begin{matrix} 174200 \pm 3300 \\ 4200 \pm 70 \end{matrix}$	$\begin{matrix} 2/3 \\ -1/3 \end{matrix}$

Using the gauge principle of local gauge theories one can derive the existence of bosons from first principles. The bosons belong to the gauge fields needed to obtain a consistent theory with interactions between the fermions. The bosons can be seen as mediator particles communicating the interactions.

The QCD – describing the strong force between quarks – introduces 8 gluons corresponding to a SU(3) symmetry. Related to the symmetry is a charge, the so-called “color”, which exists in three states: Red, blue, green. Leptons are color-neutral and do not participate in strong interactions. The quarks *and* gluons carry color charge, however, making it possible for gluons to interact with each other.

The self-interaction of gluons together with the coupling strength of the strong force has big impacts on the behavior of color-bound states. The strong coupling-constant α_s is small if quarks and gluons are near to each other giving them so-called “asymptotic freedom” at small distances. The coupling strength increases at larger distances making it impossible to use concepts from perturbative theory. The special properties of QCD yield to *confinement* of particles carrying color charge. Quarks are only observed in color-neutral bound states; as quark/anti-quark pairs – called mesons – with color and related anti-color and quark triplets – the baryons – with all three colors. If one tries to split such a bound state, the potential energy will increase until new quark-antiquark pairs are created from the vacuum. As a consequence quarks and gluons produced in elementary processes, which may even be accessible to direct perturbative calculations, induce several mesons or baryons in a process called

“hadronization”. One therefore observes so-called “jets” of particles in the detectors and always has to deal with non-perturbative QCD effects in high energy physics.

Quantum Electro Dynamics (QED) was the first big step towards the Standard Model of particle physics. It is a combination of classical electrodynamics with quantum mechanics and describes the electromagnetic interactions between electrical charged particles by the exchange of photons (γ). The observation of particle decays revealed the existence of another interaction besides the strong force and electromagnetism between all fermions; the so-called weak force. The electromagnetic and the weak force could be formally unified into electro-weak theory by Glashow, Salam and Weinberg in 1967. Its underlying gauge symmetry is a $SU(2)_L \times U(1)_Y$ symmetry. It introduces four gauge bosons which are identified with the mediator particles γ, Z^0, W^\pm of electromagnetic and weak interaction.

The gauge bosons of the $SU(2)_L \times U(1)_Y$ symmetry cannot acquire masses by explicit mass terms in the Lagrangian, but the Z^0 and W^\pm of electro-weak theory have masses resulting in a limited range of the weak force, as observed by experiments. The masses are introduced by the so-called “Higgs-mechanism” using spontaneous symmetry breaking. The Higgs-mechanism needs another field which is connected to another boson, the “Higgs boson”. It has not been observed yet, but the results of former experiments suggest that it should be observable at the LHC, if the Standard Model is correct.

As a specialty of the electro-weak theory its eigenstates are not identical to the mass eigenstates of the fermions. The theory can be formulated in a way that the eigenstates of the leptons are identical, but the quark eigenstates have to mix. The Cabibbo-Kobayashi-Maskawa (CKM) matrix describes this mixing of mass eigenstates to eigenstates of the weak interaction. The mixing is not very large, though, but it allows for decays of the fermions of the second and third family into fermions of the first family. This would not be possible without the mixing, because the weak interaction just mediates within one family of its eigenstates. Decays from one family to another are suppressed due to the small mixing, which is the reason for the rather long lifetimes of hadrons containing b quarks.

2.2 Physics beyond the Standard Model

Some important questions remain in the Standard Model, e. g. the hierarchy problem: Why is the “weak scale”, given by the masses of the Z and W bosons, many orders of magnitude below the Planck scale M_{Pl} . Furthermore first hints exist for deviations from the Standard Model, e. g. hints for non-vanishing neutrino masses, which are massless in the Standard Model.

Supersymmetric theories are one class of extensions of the Standard Model. Quadratic divergences as they occur in theories like the Standard Model can be avoided using a supersymmetry between fermions and bosons [Dre96]. The enhancement of

the Standard Model with supersymmetry doubles the number of particles at least, because it is not possible for one particle of the Standard Model to be a superpartner of another. Even the minimal supersymmetric Standard Model (MSSM) has about 120 parameters mostly connected to the breaking of supersymmetry. Supersymmetry must be broken spontaneously to give superparticles TeV scale masses. The enormous number of parameters has to be reduced by different models which are promising candidates. Benchmark scenarios are used to calculate mass spectra and branching ratios of decay chains which can be tested in experiment. In several models the lightest supersymmetric particle is stable and a good candidate for dark matter which is suggested by cosmological studies.

There are several other theories beyond the Standard Model, though. Various Technicolor models for example exist in which the masses of the W and Z bosons are dynamically created by composite Higgs particles similar to the dynamics in QCD. Many models are already strongly constrained by existing observations and predict new particles which should be observable at the energy range of the LHC. The LHC experiments will therefore be able to give hints which theories and models need further attention and will also exclude some models.

3 The ATLAS Experiment

ATLAS (A Toroidal Lhc ApparatuS) is a multi-purpose experiment in high energy physics (HEP) at the Large Hadron Collider (LHC) at CERN – the European Organization for Nuclear Research – astride the French-Swiss border near Geneva. LHC is foreseen to be operational in 2007 and will accelerate and collide protons with center of mass energies up to 14 TeV. The accelerator uses part of the infrastructure remaining from the former LEP collider including the tunnel with 27 km circumference.

The particle beams are brought to collision at four dedicated points of the ring, where the detectors of the experiments are located. Two of them host the huge multi-purpose experiments ATLAS and CMS (Compact Muon Solenoid). At two other collision points are LHCb – with focus on B-hadron physics – and ALICE – designed for heavy ion collisions to study the quark-gluon-plasma – located. The TOTEM experiment is integrated into the CMS detector to measure the total proton-proton cross section.

ATLAS is the largest LHC detector with a length of approximately 46 m, a diameter of 22 m and a weight of 7000 tons.

3.1 Aims and Design concepts

The general aim of the ATLAS experiment was to cover a wide range of topics in particle physics from Standard Model (SM) physics, like SM Higgs search and top quark studies, to Super SYmmetry (SUSY) and the search for other signatures of “new” physics, like extra dimensions. The search for the Standard Model Higgs boson will be a central part of the physics analysis of the ATLAS experiment to solve one of the big remaining questions in particle physics. Many physicist believe to find hints of physics beyond the Standard Model at ATLAS and the LHC. The ATLAS Detector and Physics Performance Technical Design Report [ATL99] provides a comprehensive overview of the physics processes to be studied with the ATLAS detector.

Its overall design follows the classical layout of many modern HEP experiments. The innermost part contains a tracking system for the precise measurement of charged particles which is kept in a strong solenoid magnetic field of about 2 Tesla. It is surrounded by electromagnetic and hadron calorimeters to stop and measure the energy of particles. A muon tracker builds the outermost part of the detector, because muons cannot be stopped in the calorimeters. The muon spectrometer is contained in a toroidal field of up to 4 Tesla. To provide a hermetic coverage up to angles close to the beam pipe

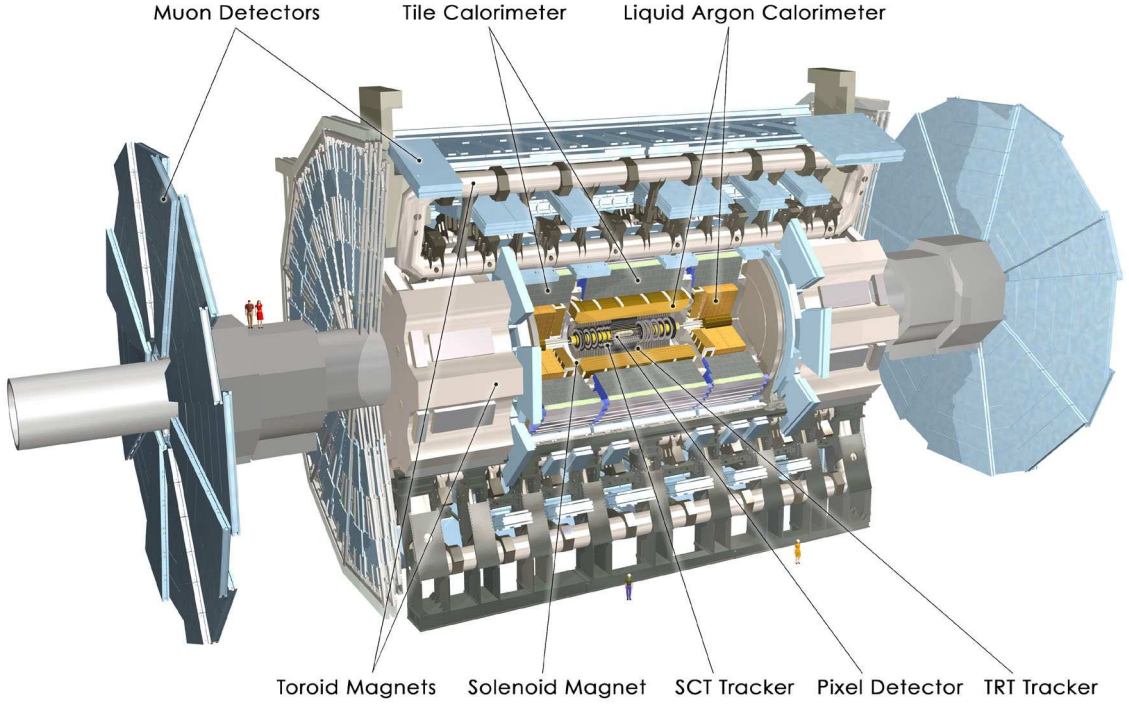


Figure 3.1: *Sketch of the ATLAS detector*

the general shape consists of a barrel part, which is cylindrically arranged around the beam pipe and two end cap parts in form of several “disks” perpendicular to the beam pipe (see figure 3.1).

Tagging of B-hadrons or even D-hadrons is important for studies of the top-quark properties and for suppression of backgrounds of many other processes. To fulfill the demands of all studies the ATLAS detector was designed to have excellent tracking capabilities, the ability to identify leptons and high energy and position resolution in the calorimeters.

The global coordinate frame of the ATLAS detector was chosen to be a right-handed cartesian coordinate system with its origin at the detector’s center, the positive X axis pointing to the center of the LHC ring and the positive Y axis pointing upward. The Z axis then points along the beam pipe. One introduces cylindrical coordinates (R, ϕ, Z) where

$$R = \sqrt{X^2 + Y^2} \quad (3.1)$$

$$\phi = \tan^{-1}(Y/X) \quad (3.2)$$

$$\theta = \cot^{-1}(Z/R) \quad (3.3)$$

with the parameter ranges $\phi \in [-\pi, \pi[$ and $\theta \in [0, \pi]$. The pseudorapidity

$$\eta = -\log \tan(\theta/2) \quad (3.4)$$

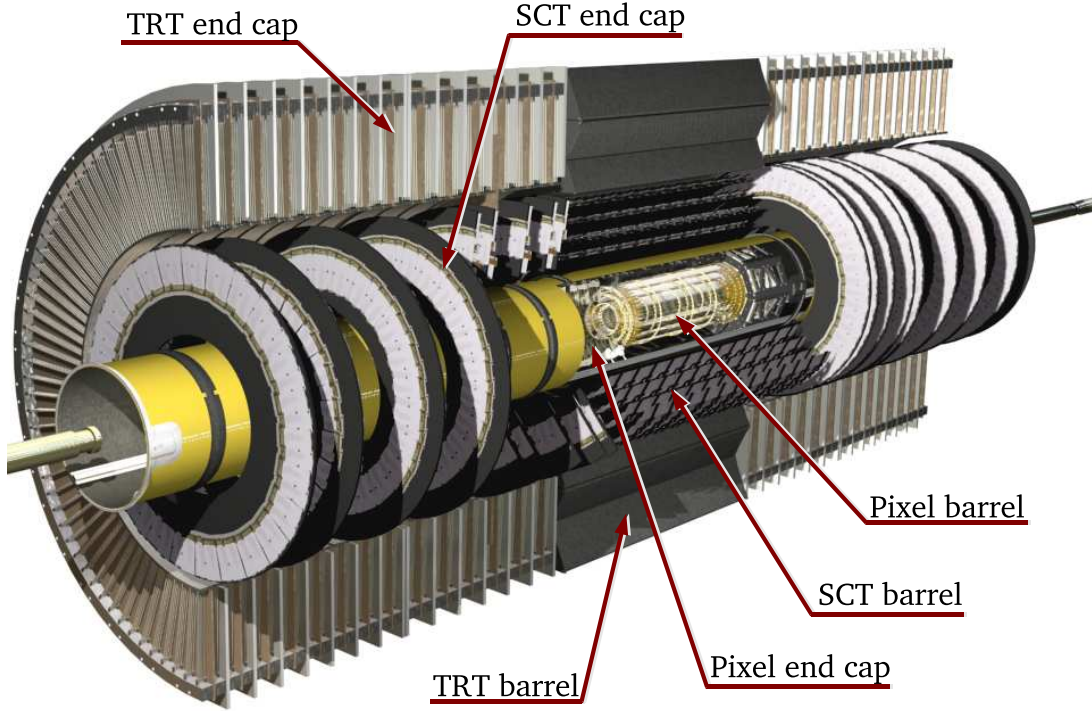


Figure 3.2: *Drawing of the ATLAS Inner Detector*

with $\eta \in [-\infty, \infty]$ is often used instead of θ itself.

3.2 Inner Detector

The *Inner Detector* of ATLAS consists of two semiconductor detectors, the Pixel detector and a silicon strip detector (SCT). The silicon detectors are surrounded by a drift tube detector (TRT) which is able to identify electrons and pions by transition radiation. Figure 3.2 sketches the Inner Detector including the barrel region in the middle and the end cap regions of SCT and TRT alongside. The end cap disks of the Pixel detector are partially contained in the barrel part of SCT and TRT.

Two contrary demands had to be fulfilled by the design of the Inner Detector; the sub-detectors should have as little material as possible to reduce effects of multiple scattering, etc. on the trajectories of the particles and on the other hand have to be very radiation hard. The high luminosity of the LHC will produce high radiation levels especially at the innermost layers of the detector and the sub-systems should resist high doses through their expected lifetime without loss of functionality.

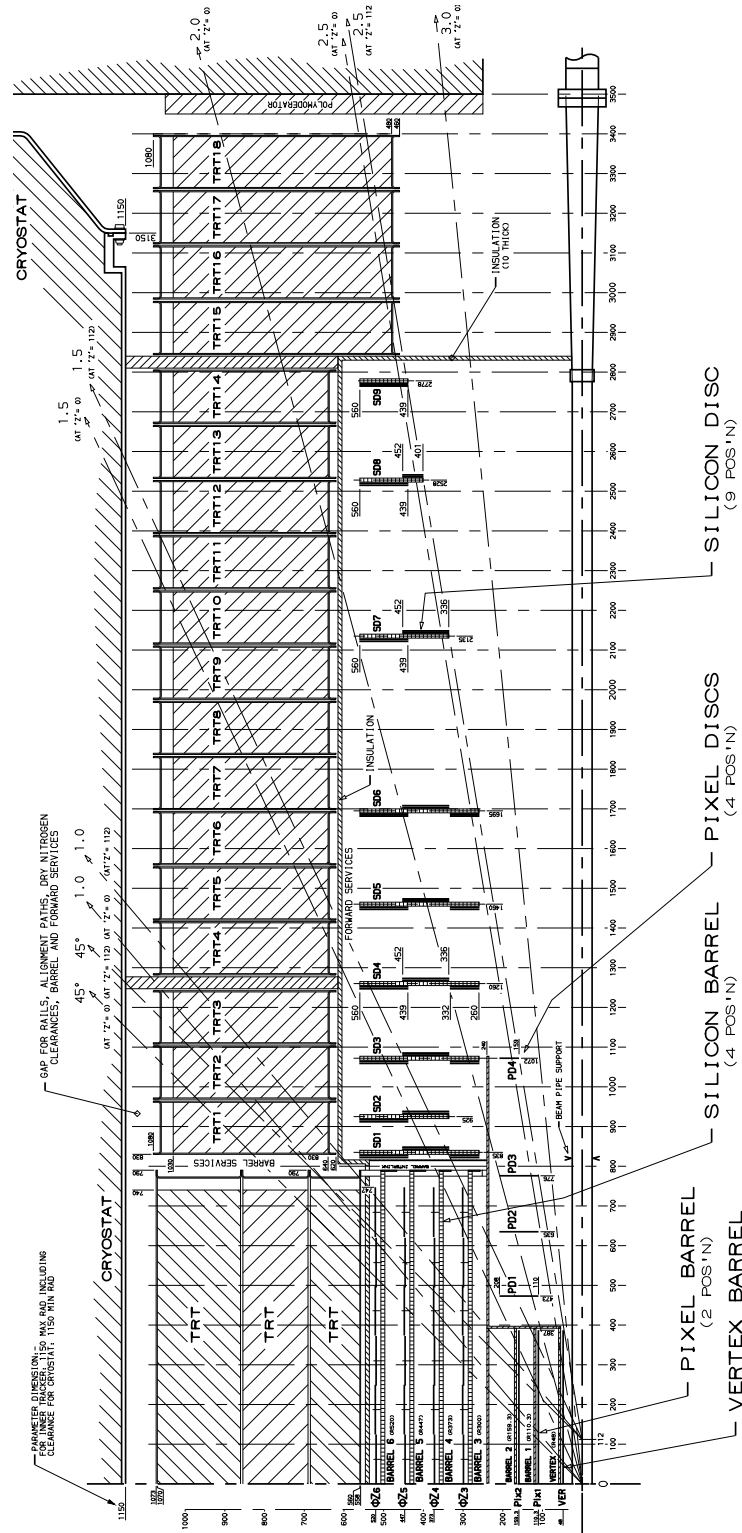


Figure 3.3: *Cross-sectional view of the Inner Detector: X – Z view of one half of the detector including the lines of different pseudorapidity η (from [ATL97a, page 6]).*

3.2.1 Pixel Detector

The *Pixel detector* was designed to provide high spatial resolution measurements very near to the interaction point. This high resolution is needed for precise estimation of impact parameters and lifetime tagging of particles. The pixel detector delivers full 3-dimensional measurements (2-dimensional in the plane of the detector modules) of the trajectories of charged particles. Tracks through the Inner Detector produce on average three measurements in the Pixel detector.

The measurement technique is based on semiconductors which are used as depleted diodes in reverse-biasing. The sensitive silicon layer is connected to the readout electronics by bump-bonds. 16 chips (2×8) with 18×160 pixels each are mounted on one Pixel module. The module carries the readout electronics, a module controller and the connection interfaces. They are installed in staves in the barrel part and sectors in the end cap disks in a way that modules overlap to have no gaps in the detector layers. All modules have identical layout. The barrel part embodies 1456 modules in three layers and the endcap disks 144 modules each, summing up to about 80 000 000 readout channels.

The pixels on a chip have dimensions of $400 \mu\text{m} \times 50 \mu\text{m}$ resulting in a resolution of $60 \mu\text{m} \times 12 \mu\text{m}$. A single particle will usually activate more than one pixel per chip, i. e. a clustering of adjacent pixels is needed during reconstruction. The readout is analog by measuring the time over threshold of a linear discharge of channels. This allows for charge interpolation between adjacent pixels to improve the spatial resolution. Pixel modules in the barrel part are oriented with the direction of high resolution in $R\phi$ direction and low resolution in Z direction. In the end caps the low resolution direction is oriented along R .

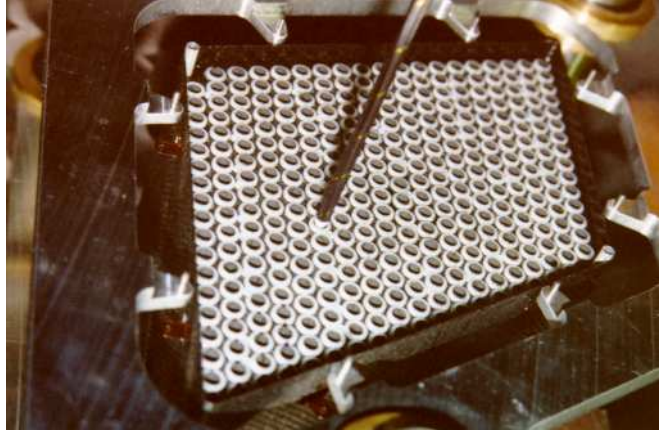
3.2.2 Silicon-Strip-Detector (Semiconductor Tracker, SCT)

The second semiconductor-based sub-detector of the Inner Detector is the *Semiconductor Tracker* (SCT). The measurement technique is very similar to the Pixel detector, but measurements are only 1-dimensional in the plane of the detector modules as silicon strips are used instead of pixels. Modules are double-sided with a small stereo angle of 40 mrad between the strips to get at least a rough estimate of the track position in the second coordinate.

The clusters of activated strips on both sides of the back-to-back module have to be matched during reconstruction. Therefore ambiguities arise when 3-dimensional information is extracted from the measurements, if more than one cluster exists per module, which is usually the case¹. 768 channels are used in each side of a back-to-back module with a size of $80 \mu\text{m} \times 120 \text{ mm}$ resulting in a resolution of $16 \mu\text{m} \times 580 \mu\text{m}$.

¹Back-to-back clusters are just combined to 3-dimensional information in the trigger reconstruction and in global pattern recognition. The precise track fit in offline reconstruction uses clusters on back-to-back modules as two separated measurements.

Figure 3.4: *Barrel TRT module:* The drift tubes are surrounded by a polypropylen radiator for generation of transition radiation and arranged in a honeycomb structure. The photograph shows a prototype module during straw insertion (from [ATL97a, page 614]).



3 module layouts exist for the end cap part and 1 layout for the barrel region. The strips on one layer of the barrel modules are parallel to each other, whereas the strips in the end cap modules are expanded to be more dense near the beam pipe.

The double-sided modules are arranged in four concentric barrel layers and nine end cap discs. 2112 barrel modules and 2×988 end cap modules are used. The higher precision is reached again in $R\phi$ direction in the barrel part and lower precision along R in the end caps.

3.2.3 Straw Tube Detector using Transition Radiation (Transition Radiation Tracker, TRT)

The outermost part of the Inner Detector is represented by the *Transition Radiation Tracker* (TRT). The TRT uses a completely different measurement technique than the Pixel and SCT detectors. It is composed of drift tubes surrounded by a radiator for the production of transition radiation, which can be used to identify electrons. The so-called “straws” of the TRT consist of $30\ \mu\text{m}$ thick gold-plated anode wires in the center of tubes with 2 mm radius which are filled with a gas mixture (70% Xe + 27% CO₂ + 3% O₂) for ionization. Electrons more likely generate transition radiation photons which are seen as higher charge deposition in the detector, giving so-called “high-threshold” hits.

In the barrel part straws have a maximum length of 150 cm arranged in three cylindrical rings around the SCT detector with straw direction parallel to the beam pipe. The straws are split at the center to reduce the occupancy and read out at each end, i. e. they form a section with $Z < 0$ and $Z > 0$, respectively. For the same reason are the first six radial layers only active over the last 36 cm in Z . The distance of straws is on average 6.8 mm in both directions. The barrel contains about 50 000 straws in 73 layers from which 36 straws are hit on average by a track through the barrel part.

The TRT end caps consist of 20 wheels each with radial straws of 39 cm length covering a radial range from 64 cm to 103 cm. The wheels are divided in layers with 768 straws and the space between successive layers is filled with thin polypropylen foils for generation of transition radiation. 245 760 straws are contained in the end caps in total. The production of additional wheels for the outermost layers including longer straws has been staged [A⁺04].

The distance of the trajectory from the wire can be determined by a drift time measurement. The ions created by a charged particle in the gas reach a constant speed when drifting to the wire, depending on the gas mixture, the gas pressure, and the voltage between tube and wire. One therefore gets a nearly linear relation between measured drift time and drift radius. The $R-t$ relation can be experimentally determined at test beams and a 3rd grade polynomial is used as approximation in the reconstruction. A resolution of about 170 μm is expected perpendicular to the wire.

The measurement of the distance of a particle track from a wire yields ambiguities which have to be solved during track reconstruction. From a single TRT measurement it cannot be decided on which side of the wire the particle passed by. This *left/right ambiguity* can be solved, if the information of several measurements is combined, though. Additional complications may arise, if a potential sagging of the wire due to gravitational effects has to be considered. But the wire tension in the TRT is assumed to be strong enough such that one can neglect sagging.

3.3 Calorimeter

Calorimeters are used to measure the energy of particles by stopping them completely in material. Therefore they consist of passive material to induce material interactions and active detector parts to measure the particle shower. Besides a precise energy measurement calorimeters need be fine grained in their spatial resolution. A full, hermetic coverage of the calorimeter system is needed to identify missing transverse energy from neutrinos and potential new weakly interacting particles, which is an important signature of many processes. ATLAS uses two different technologies for calorimetry: Lead and liquid argon and a combination of iron absorbers with plastic scintillators.

The Liquid Argon calorimeter is used for electromagnetic calorimetry in the range $|\eta| < 3.2$. Additionally it is used for hadronic calorimetry from $|\eta| = 1.4$ up to $|\eta| = 4.8$. Liquid argon is the active material circumfluent an “accordion” structure of lead absorbers and Kapton electrodes [ATL96a]. This technique has been proven to be very radiation hard. Several parts of the calorimeter system are based on the Liquid Argon technique; the electromagnetic barrel and end cap, the hadronic end cap and the forward calorimeter.

The Tile Calorimeter [ATL96b] surrounds the Liquid Argon calorimeters and is used for hadron calorimetry. Scintillating tiles are embedded in steel absorbers and read

out by wavelength shifting fibres. A 3-dimensional segmentation is reached with a $\Delta\eta \times \Delta\phi$ segmentation of 0.1×0.1 and 0.2×0.1 , respectively.

3.4 Muon Spectrometer

Muons with momenta above 3 GeV cannot be stopped in the calorimeter and are the only charged particles to leave the detector. Several important event signatures have high momentum muons in their final states and muons are therefore used for trigger purposes. Hence the muon spectrometer consists of two kinds of trigger chambers and of two kinds of precision chambers for tracking. The toroid magnet system and the muon detector chambers are interwoven at the outermost part of the ATLAS detector. The magnetic field for $|\eta| \leq 1$ is produced by the large air-core toroid magnet consisting of eight coils surrounding the hadron calorimeter. The η region $1.4 \leq |\eta| \leq 2.7$ is covered by two smaller end cap toroids inserted into the end of the barrel magnet.

Track coordinates are measured in the principal bending direction of the magnetic field by Monitored Drift Tubes (MDTs) and at large pseudorapidities by Cathode Strip Chambers (CSCs). The measurement technique of the MDTs is very similar to the drift radius measurement in the TRT. The MDTs consist of 2×3 or 2×4 layers of aluminum tubes with 30 mm diameter filled with a gas mixture and a central tungsten-rhenium wire, which reach a resolution of typically $80 \mu\text{m}$ each. The CSCs on the other hand are multiwire proportional chambers. Their spatial resolution is sensitive to the inclination of tracks and the Lorentz angle, but resolutions better than $60 \mu\text{m}$ are possible.

The trigger system uses Resistive Plate Chambers (RPCs) in the barrel and Thin Gap Chambers (TGCs) in the end caps. Both provide high time resolution to be able to identify individual bunch crossings and a second-coordinate measurement of tracks orthogonal to the precision measurements of MDTs and CSCs. The RPCs are gaseous detectors formed by a narrow gas gap between two parallel resistive plates. A high, uniform electric field between the plates initiates an avalanche when muons pass through the chamber. Orthogonal pick-up strips provide the spatial resolution of 1 cm at a time resolution of 1 ns. The TGCs are similar to multiwire proportional chambers, but use a very small distance between cathode and anode wires. Readout strips are used to measure the second coordinate. The whole muon system consists of 32 CSCs, 1194 MDTs, 596 RPCs and 192 TGCs giving 1 200 000 readout channels (cp. [ATL97b]).

4 Track reconstruction

The reconstruction of tracks generated by charged particles in high energy physics experiments consists of various steps which will be briefly described in the following sections. A detailed summary can be found in [RF00] and [Man04]. The very basic steps like the hardware-oriented signal processing and conversion of raw data into data objects of the reconstruction software will not be presented here. It is assumed that one starts with measurements on different detector surfaces which already contain calibrations like signal calibrations and alignment corrections to the detector modules.

At the beginning of track reconstruction stands a pattern recognition procedure, which groups measurements belonging to a track candidate. In general this procedure will produce many “ghost” track candidates not belonging to a true particle trajectory. Such ghosts have to be identified and dropped later. The process of track fitting therefore does not only include the best estimation of track parameters for a given set of measurements, but it also has to be used to estimate the quality of the fit.

One distinguishes global and local pattern recognition methods for track finding. Global methods try to identify all tracks at the same time. They produce a list of track candidates and can be regarded as global transformations of the entire set of measurements into track parameter space. In local methods, on the other hand, a single track candidate is processed each time. Local methods usually take a “seed” as starting point and try to find additional measurements belonging to this candidate. Therefore global pattern recognition methods are often followed by a local pattern recognition during the track fit to solve ambiguities e.g. in drift tube detectors or to further reject noise measurements.

Pattern recognition and track fitting methods may even be used several times after each other to be able to reconstruct the “whole picture”. It is sometimes needed for example to use the information obtained in a track fit to recalibrate the measurement data.

4.1 Pattern recognition

Histogramming methods are widely used for global pattern recognition. A straight-line track going through the origin does not change its angle to one of the axis for example. If one fills a histogram with the angles of all measurements of an event, the measurements belonging to a straight-line track will peak in the histogram. This concept can easily be generalized to helical tracks using a conformal transformation.

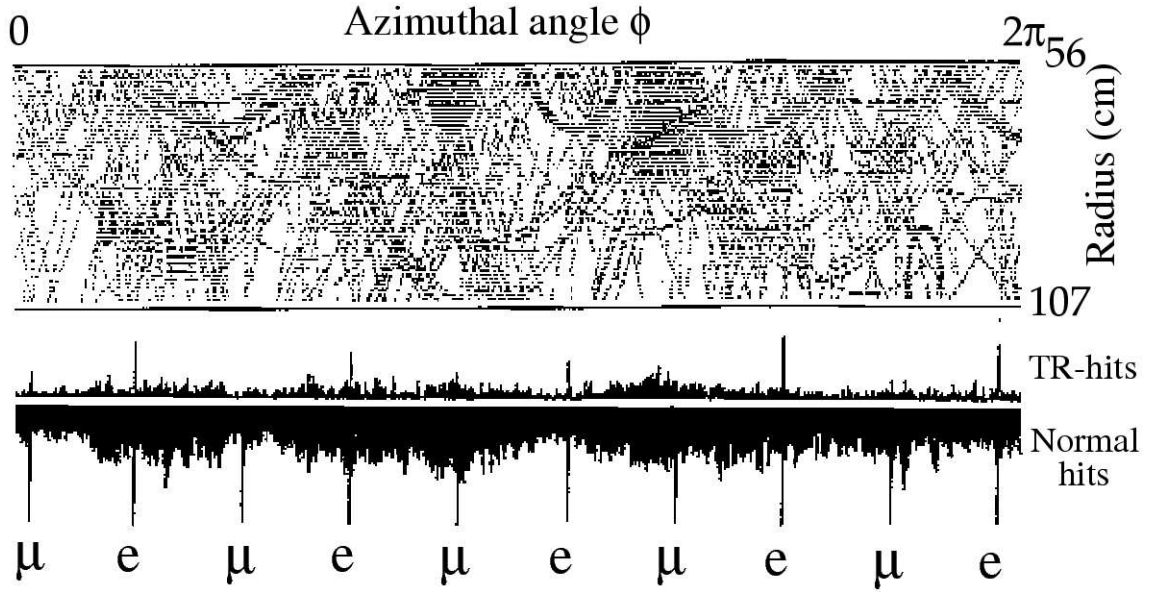


Figure 4.1: *Histogramming for pattern recognition in the ATLAS TRT: $R\phi$ view and histogram for muon and electron tracks with pile-up background (from [ATL97a, p. 597]).* The upper part of the histogram contains the ϕ position of high threshold hits generated by transition radiation from electrons and the lower part normal tracking hits in the TRT. This technique allows one to identify high momentum tracks in the TRT and to distinguish between electrons and other particles.

The ATLAS Inner Detector Technical Design Report [ATL97a] provides an example for such a histogram for measurements in the TRT (figure 4.1).

This simple histogramming does only work if the tracks are to good approximation straight-line or helical, otherwise the histogrammed variable will not be a constant for the tracks and no clear structure can be seen in the histogram.

Another method often used in high energy physics experiments is the so-called HOUGH-transform. In this case the measurement positions are transformed from measurement space into parameter space of the tracks¹. Each point in the parameter space belongs to a specific track, whereas a single measurement is described by a line or in general a curve. The point where all curves of the measurements belonging to one track cross corresponds to the track parameters of that track. The HOUGH-transformed measurements can again be histogrammed and the track parameters of the track candidate extracted from the peaks in the histogram.

¹The parameter space corresponds to the vector space (or a subspace) of track parameters and the measurement space to the n -tuple of measurement coordinates.

4.2 Track parameterization

The track parameterization in high energy physics experiments mostly assumes a homogenous magnetic field with field direction parallel to the beam axis. In the ATLAS Inner Detector this is at least approximately given. If one uses a parameterization with local coordinates at each point in space, the resulting helical parameterization can be seen as a local approximation of the true trajectory of charged particles in an arbitrary magnetic field.

Starting with the assumption of a static, homogenous magnetic field one gets a helical path of a charged particle which can be seen as follows. A charged particle in a static magnetic field $\vec{B}(\vec{r})$ without electric field moves under the influence of the LORENTZ force

$$\vec{F}_L \propto q\vec{v} \times \vec{B} \quad (4.1)$$

where \vec{v} is the velocity of the particle and q its charge. The trajectory has to obey the (relativistic) equations of motion

$$\frac{d\vec{p}}{dt} = c^2 \kappa q \vec{v}(t) \times \vec{B}(\vec{r}(t)) \quad (4.2)$$

where κ is a proportionality factor, $\vec{r}(t)$ the spatial position of the particle at time t in the laboratory frame and c the velocity of light (cp. [Jac02, pp 676]). This ordinary differential equation can be transformed into a geometrical form, which uses the path length s as variable.

$$\frac{d^2 \vec{r}}{ds^2} = \frac{\kappa q}{|\vec{p}|} \frac{d\vec{r}}{ds} \times \vec{B}(\vec{r}(s)) \quad (4.3)$$

If one now assumes a homogenous magnetic field along the z -axis ($\vec{B}(\vec{r}) = \vec{B}_0 = B_0 \vec{e}_z$) equation 4.3 can be solved by a helix:

$$\begin{pmatrix} x \\ y \\ z \end{pmatrix} (s) = \begin{pmatrix} x^0 + R_H \cdot \left(\cos(\alpha_0 + hs \cdot \cos \frac{\lambda}{R_H}) - \cos \alpha_0 \right) \\ y^0 + R_H \cdot \left(\sin(\alpha_0 + hs \cdot \cos \frac{\lambda}{R_H}) - \sin \alpha_0 \right) \\ z^0 + s \cdot \sin \lambda \end{pmatrix} \quad (4.4)$$

where $\vec{r}^0 = (x^0, y^0, z^0)^\top$ is the starting point at $s = s^0$; $\lambda = \sin^{-1}(dz/ds)$ is the slope angle, $R_H = \frac{|\vec{p}| \cos \lambda}{|\kappa q B_0|}$ the radius of the helix and $h = -\text{sign}(qB_0)$ its sense of rotation. Using this helix solution one has to make a choice for the five dimensional track parameters \vec{x} to be fitted. ATLAS uses several parameterizations in parallel, which are chosen appropriate to the reference surface. The perigee parameters $d_0, z_0, \phi_0, \theta, \frac{q}{p}$ are commonly used to express the track state next to the origin of the global coordinate system using the perigee point $P = (x_P, y_P, z_P)$, which is defined as the point of closest approach of a track to the global z axis.

d_0	signed transverse impact parameter	$d_0 = \pm \sqrt{x_P^2 + y_P^2}$
z_0	longitudinal impact parameter	$z_0 = z_P$
ϕ_0	azimuth angle of the track direction at P	
θ	polar angle of the track direction at P	$\cot \theta = \frac{p_z}{\sqrt{p_x^2 + p_y^2}} = \frac{p_z}{p_T}$
$\frac{q}{p}$	charge signed inverse momentum	$\frac{q}{p} = \frac{q}{ p }$

4.3 Estimation of track states

For a given set of measurements $\vec{m}_k|_{k=1,\dots,n}$ on detector surfaces k the track parameters \vec{x} on a chosen reference surface need to be estimated, i.e. a so-called track fit is performed. Each fit requires an underlying *track model* describing the mapping \vec{f} from the track parameters \vec{x} into the measurement space (as seen above a helix may serve as a track model in a homogenous magnetic field).

$$\vec{c} = \begin{pmatrix} \vec{m}_1 \\ \vdots \\ \vec{m}_n \end{pmatrix} = \vec{f}(\vec{x}^t) + \vec{\epsilon} \quad (4.5)$$

where \vec{x}^t is the 5-dimensional² vector of the true track parameters and $\vec{\epsilon}$ the vector of random measurement errors. The measurement errors are assumed to be unbiased, i.e. having vanishing expectation value $\langle \vec{\epsilon} \rangle = \vec{0}$ and the covariance matrix

$$\mathbf{V} = \left\langle (\vec{c} - \langle \vec{c} \rangle) (\vec{c} - \langle \vec{c} \rangle)^\top \right\rangle = \left\langle \left(\vec{c} - \vec{f}(\vec{x}^t) \right) \left(\vec{c} - \vec{f}(\vec{x}^t) \right)^\top \right\rangle \quad (4.6)$$

The purpose of the track fit is to find an unbiased estimation \vec{x} of the true track parameters \vec{x}^t for a given set of measurements $\vec{m}_k|_{k=1,\dots,n}$. Beside the track parameters on the reference surface (e. g. a plane through the origin) one is usually also interested in the track states on the measurement surfaces to get the residuals between measurement and estimated track state.

In general two basic kinds of track fitters are used,

- global fitters using the Least Squares Method (LSM)
- local fitters utilizing recursive filters

Both methods are usually equivalent and have optimal properties for Gaussian errors, but in general it is easier to introduce material effects like multiple scattering into recursive filters. The basic properties of global and local methods are described in the following sections.

²Independent from the underlying track model, the equations of motion have 6 integration constants (mostly initial position and momentum of the particle), which reduce to 5 degrees of freedom, if one assumes a reference surface in space.

4.3.1 Global χ^2 fits

Global fitters define a metric for the distance between fitted track and measurements they try to minimize. In the Least Squares Method the dependency of the estimated track positions on the surfaces from the estimated track parameters (i.e. the track model) is linearly approximated³ around an expansion point \vec{x}_0

$$\vec{f}(\vec{x}) \approx \vec{f}(\vec{x}_0) + \mathbf{A} \cdot (\vec{x} - \vec{x}_0) \quad (4.7)$$

with

$$\mathbf{A} = \left. \frac{\partial \vec{f}(\vec{x})}{\partial \vec{x}} \right|_{\vec{x}=\vec{x}_0}$$

and it is tried to minimize the function

$$M = \left(\vec{f}(\vec{x}) - \vec{c} \right)^\top \mathbf{V}^{-1} \cdot \left(\vec{f}(\vec{x}) - \vec{c} \right) \quad (4.8)$$

$$= \left(\vec{f}(\vec{x}_0) + \mathbf{A} \cdot (\vec{x} - \vec{x}_0) - \vec{c} \right)^\top \mathbf{V}^{-1} \cdot \left(\vec{f}(\vec{x}_0) + \mathbf{A} \cdot (\vec{x} - \vec{x}_0) - \vec{c} \right) \quad (4.9)$$

Formally this can be done by setting $\frac{\partial M}{\partial \vec{x}} \stackrel{!}{=} \vec{0}$. The introduction of material effects into the global fit is for example explained in [Cor06].

4.3.2 Recursive track fitting: The Kalman filter

In contrast to global fitters recursive filters add the measurements successively to the track. The track states are therefore not only known on a single reference surface, but for each surface of a measurement. This feature of recursive filters has some advantages for track fitting in high energy physics, because material effects like energy loss can easily be considered in the track fit.

The linear Kalman filter is used in control theory to analyse linear dynamic systems of the form

$$\frac{d\vec{x}(t)}{dt} = \mathbf{F}(t) \cdot \vec{x}(t) + \mathbf{G}(t) \cdot \vec{w}(t) \quad (4.10)$$

where $\vec{x}(t)$ is the system state vector, $\vec{w}(t)$ a random forcing function and $\mathbf{F}(t)$ and $\mathbf{G}(t)$ time-dependent matrices describing the system; the deterministic control input normally added is dropped here. Such an ordinary differential equation can formally be solved by

$$\vec{x}(t) = \Phi(t, t_0) \cdot \vec{x}(t_0) + \int_{t_0}^t \Phi(t, \tau) \mathbf{G}(\tau) \cdot \vec{w}(\tau) d\tau \quad (4.11)$$

³The linearization in the track parameters does not mean that the tracks themselves have to be linear, though.

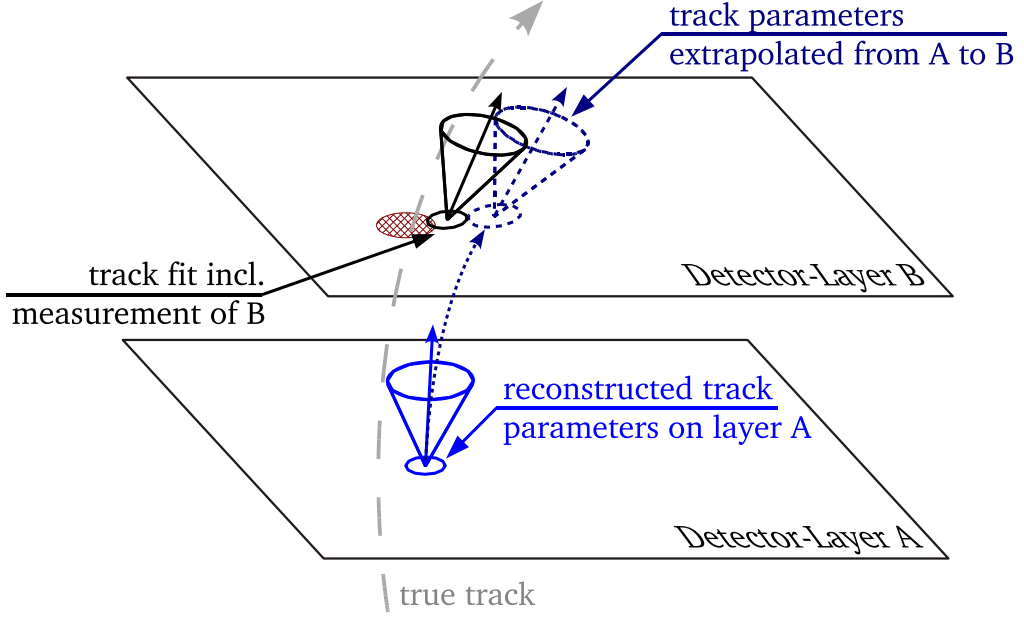


Figure 4.2: *Functional principle of the Kalman filter for track fitting:* The reconstructed track parameters on surface A are extrapolated to surface B. On Surface B the Kalman update is performed, which includes the measurement from detector layer B into the fit.

with the transition matrix $\Phi(t, t_0)$ obeying $\frac{d}{dt}\Phi(t, t_0) = \mathbf{F}(t)\Phi(t, t_0)$ or in a discrete form

$$\vec{x}_{k+1} = \Phi_k \cdot \vec{x}_k + \Gamma_k \cdot \vec{w}_k \quad (4.12)$$

with $\Phi_k = \Phi(t_{k+1}, t_k)$ and $\Gamma_k \cdot \vec{w}_k = \int_{t_k}^{t_{k+1}} \Phi(t_{k+1}, \tau) \mathbf{G}(\tau) \cdot \vec{w}(\tau) d\tau$ (cp. [Gel74, sec. 3.3]).

This situation can be applied to track fitting in high energy physics, if one uses the time evolution index k to enumerate the track states on the different detector surfaces. In general one considers a discrete system with states \vec{x}_k , a linear transformation Φ_k describing the evolution and a random disturbance \vec{w}_k with zero mean and covariance \mathbf{Q}_k which is the process noise (e.g. multiple scattering)

$$\vec{x}_k = \Phi_{k-1} \cdot \vec{x}_{k-1} + \vec{w}_{k-1}, \quad \vec{w}_k \propto \varphi(\vec{0}, \mathbf{Q}_k) \quad (4.13)$$

where $\varphi(\vec{\mu}, \mathbf{\Sigma})$ denotes a multivariate Gaussian distribution with mean $\vec{\mu}$ and covariance matrix $\mathbf{\Sigma}$. The measurement equation is assumed to be

$$\vec{m}_k = \mathbf{H}_k \cdot \vec{x}_k + \vec{\epsilon}_k, \quad \vec{\epsilon}_k \propto \varphi(\vec{0}, \mathbf{V}_k) \quad (4.14)$$

where $\vec{\epsilon}_k$ is again uncorrelated noise with variance \mathbf{V}_k corresponding to measurement uncertainties. The measurement matrix \mathbf{H}_k describes the mapping from track parameter space to measurement space, i. e. the actual measurement process. Equations

(4.13) and (4.14) combined and used for all k are comparable to the general track model equation (4.5), but in the Kalman formalism process noise like multiple scattering and measurement noise given by the detector resolution are separated.

The derivation of the discrete, linear Kalman filter can e. g. be found in [Gel74, sec. 4.2] and therefore just the result is stated here. The notation follows [Frü87]. The estimated state vector (track parameters) on detector layer k , including the knowledge up to layer j , is denoted by $\vec{x}_{k|j}$.

Figure 4.2 sketches the functional principle of the Kalman filter for a single step of the recursion. The estimated track parameters $\vec{x}_{k-1|k-1}$ on layer $k-1$ are extrapolated to detector layer k giving the *prediction* $\vec{x}_{k|k-1}$

$$\vec{x}_{k|k-1} = \Phi_{k-1} \cdot \vec{x}_{k-1|k-1} \quad (4.15)$$

with the covariance $\mathbf{C}_{k|k-1}$ of the predicted state

$$\mathbf{C}_{k|k-1} = \Phi_{k-1} \mathbf{C}_{k-1|k-1} \Phi_{k-1}^\top + \mathbf{Q}_{k-1} \quad (4.16)$$

The predicted state is then *updated* with the measurement from layer k using a linear combination of the expected measurement and the true measurement on layer k which are weighted by their weight matrices (inverse of the covariance matrices)

$$\vec{x}_{k|k} = \mathbf{C}_{k|k} \cdot ((\mathbf{C}_{k|k-1})^{-1} \cdot \vec{x}_{k|k-1} + \mathbf{H}_k^\top (\mathbf{V}_k)^{-1} \cdot \vec{m}_k) \quad (4.17)$$

with the covariance $\mathbf{C}_{k|k}$ of the updated state

$$(\mathbf{C}_{k|k})^{-1} = (\mathbf{C}_{k|k-1})^{-1} + \mathbf{H}_k^\top (\mathbf{V}_k)^{-1} \mathbf{H}_k \quad (4.18)$$

After n recursions of this process on all measurements $k = 1, \dots, n$ (the *forward filtering*) the estimate $\vec{x}_{n|n}$ contains the information of all n measurements, and it can be shown that the estimate is unbiased and has minimum variance. The states $\vec{x}_{k|k} |_{k=1, \dots, n-1}$ do not contain the whole information, though, but only the information up to the k^{th} measurement. If one needs the whole information on every measurement surface, e.g. to identify outlier measurements with large distance to the estimated track and reject noise measurements, another process can be performed afterwards, the so-called *smoothing*. After the forward filtering just another filter (the *backward filter*) is started in the backward direction (i.e. processing the measurements in the sequence $n, n-1, \dots, 2, 1$) and the results of the forward and the backward filter are combined as weighted means.

$$(\mathbf{C}_{k|n})^{-1} = (\mathbf{C}_{k|k})^{-1} + (\mathbf{C}_{k|k+1}^b)^{-1} \quad (4.19)$$

$$\vec{x}_{k|n} = \mathbf{C}_{k|n} \cdot ((\mathbf{C}_{k|k})^{-1} \cdot \vec{x}_{k|k} + (\mathbf{C}_{k|k+1}^b)^{-1} \cdot \vec{x}_{k|k+1}^b) \quad (4.20)$$

where $\vec{x}_{k|k+1}^b$ denotes the estimated state of the backward filter on layer k containing all measurements from n to $k+1$. These formulae can be interpreted as an update

step according to equations (4.17) and (4.18) with the backward filtered prediction as “measurement”.

The linear Kalman Filter can be generalized to the extended and the linearized Kalman Filter to drop the requirement of linear system equations (4.13) and measurement equations (4.14). In this work just the generalization to non-linear system equations is presented, because the measurement equation is normally just a simple projection in high energy physics experiments. If one assumes a system equation of the form

$$\vec{x}_k = \vec{f}_{k-1}(\vec{x}_{k-1}) + \vec{w}_{k-1}, \quad \vec{w}_k \propto \varphi(\vec{0}, \mathbf{Q}_k) \quad (4.21)$$

instead of equation (4.13), the formulae for updating and smoothing remain the same for the extended Kalman filter⁴, but the propagation of the track parameters needs to be done by numerical integration or TAYLOR expansion of the function $\vec{f}_k(\vec{x}_k)$ by replacing equation (4.15) by

$$\vec{x}_{k|k-1} = \vec{f}_{k-1}(\vec{x}_{k-1|k-1}) \quad (4.22)$$

and setting

$$\Phi_k = \left. \frac{\partial \vec{f}_k}{\partial \vec{x}_k} \right|_{\vec{x}_{k|k}} \quad (4.23)$$

in (4.16).

Goodness of fit

A quality criterion is needed to decide whether a track or a measurement should be taken into the further analysis. The χ^2 value, which is the normalized squared distance of the measurements to the fitted track, provides a measure commonly used for quality cuts. The χ^2 of the filtered state⁵ is given by

$$\chi_F^2 = \vec{r}_{k|k}^\top \mathbf{R}_{k|k} \vec{r}_{k|k} \quad (4.24)$$

if one defines the filtered residual $\vec{r}_{k|k}$ by

$$\vec{r}_{k|k} = \vec{m}_k - \mathbf{H}_k \cdot \vec{x}_{k|k} \quad (4.25)$$

where its covariance $\mathbf{R}_{k|k}$ is given by

$$\mathbf{R}_{k|k} = \mathbf{V}_k - \mathbf{H}_k \mathbf{C}_{k|k} \mathbf{H}_k^\top \quad (4.26)$$

⁴the linearized Kalman filter is more or less the same as the extended filter if the measurement equation is linear, just the expansion point of the propagation changes

⁵the χ^2 of the filtered state (χ_F^2) is equal to the χ^2 of the predicted state ($\chi_F^2 = \chi_P^2 = \vec{r}_{k|k-1}^\top \mathbf{R}_{k|k-1} \cdot \vec{r}_{k|k-1}$)

This is equivalent to the following expression in weighted means formalism

$$\chi_F^2 = \vec{r}_{k|k}^\top (\mathbf{V}_k)^{-1} \cdot \vec{r}_{k|k} + (\vec{x}_{k|k} - \vec{x}_{k|k-1})^\top (\mathbf{C}_{k|k-1})^{-1} \cdot (\vec{x}_{k|k} - \vec{x}_{k|k-1}) \quad (4.27)$$

The global χ^2 of the track can be obtained by summing up all the individual χ^2 of the filtered states, because the filtered residual vectors are uncorrelated and even independent in the case of Gaussian process (\vec{w}) and measurement noise ($\vec{\epsilon}$). This is not true for the χ^2 of the smoothed states, though. The χ_S^2 of the smoothed states on the other hand has a better discrimination power against outlier measurements than the filtered one, because it contains the information about the whole track. The global χ^2 of the track is even less powerful than the χ_F^2 of a measurement to identify individual outliers, because it is the sum of all χ_F^2 , but it is useful to identify ghost tracks made up of random noise measurements. χ_S^2 of the smoothed state $\vec{x}_{k|n}$ follows directly from equation (4.27) as

$$\chi_S^2 = (\vec{x}_{k|n} - \vec{x}_{k|k})^\top (\mathbf{C}_{k|k})^{-1} \cdot (\vec{x}_{k|n} - \vec{x}_{k|k}) + (\vec{x}_{k|n} - \vec{x}_{k|k+1}^b)^\top (\mathbf{C}_{k|k+1}^b)^{-1} \cdot (\vec{x}_{k|n} - \vec{x}_{k|k+1}^b) \quad (4.28)$$

Combinatorial Kalman Filter

The recursive feature of the Kalman filter can be exploited to introduce track finding directly into the fitting process. In this case one starts with a seed and tries to follow the track candidate through the detector. The prediction on the next active detector surface is used to search for compatible measurements. In general one will find more than one compatible measurement and the fit can in this case be split into several branches belonging to the different combinations. A selection criterion must be applied to the paths to keep the number of branches reasonable. One will drop paths which lead into regions where no compatible measurements can be found anymore while taking the possibility of detector inefficiencies into account and may add a selection based on the goodness of fit. Figure 4.3 gives a simple example for such a Kalman-based track search.

4.4 Adaptive track fitting methods

In an environment like the LHC, track fitting mostly suffers from measurements which are wrongly assigned to a track candidate. At the LHC one finds very dense jets and several events at the same time in the detector resulting in a high occupancy. One also expects a rather noisy background, which may in the case of δ -rays even be correlated with a track. For drift tube detectors like the ATLAS TRT or MDT one also gets mirror hits. Therefore track fitting algorithms need to be robust against wrong measurements or should even be able to decide themselves which measurements belong to a certain track candidate.

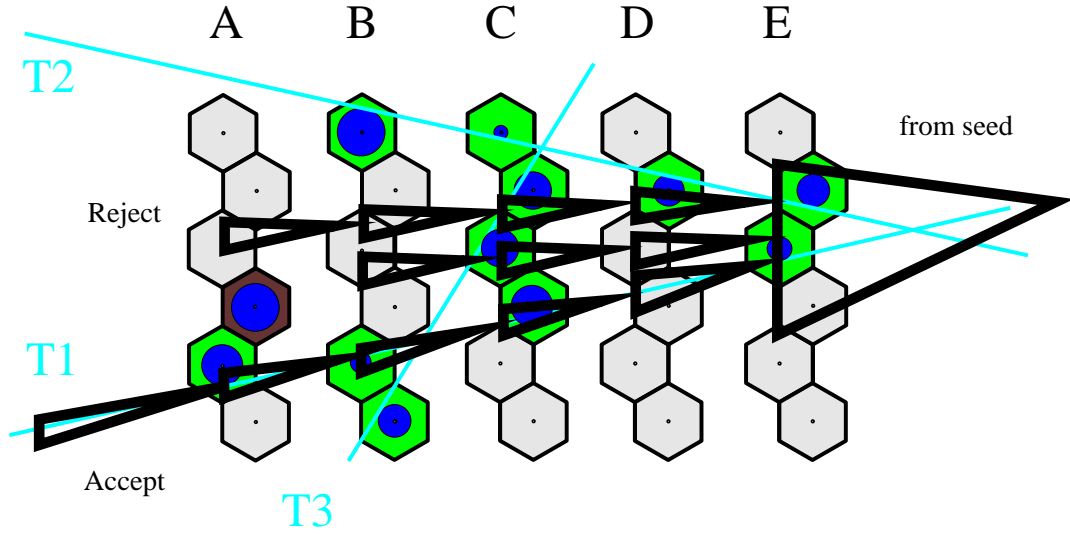


Figure 4.3: *Track finding with a Combinatorial Kalman Filter:* Illustration of the track search along different branches inside a drift tube detector starting from a track seed (from [Man97]).

The class of so-called *Adaptive Fitters* introduces special concepts into the track fitting process to solve the hit-to-track assignment in the best way. Like the standard track fitting methods split up in the two main classes of global fitters and recursive filters, the adaptive fitters can be classified in the classes of

- elastic tracking corresponding to the global fitters and
- non-linear filters

In both cases the standard algorithms are extended to take more than one measurements per detector layer into account and the optimization of the hit assignment problem is combined with the track fit.

A general problem of all optimization strategies are local optima which have to be avoided. Therefore many of the adaptive methods introduce techniques like *annealing procedures* which flatten out the “energy landscape” of the optimization problem in the beginning. A comprehensive overview of different adaptive methods can be found in [FS99].

4.4.1 Elastics Arms and Elastic Tracking Algorithms

Adaptive track fitters based on global methods use elastic arms to be adjusted to the measurements. They either define an energy function with explicit assignment probabilities for each measurement or an interaction potential between track and measure-

ments which directly takes the distance between measurement and elastic arm into account.

The Elastic Tracking algorithm (ETA) by Gyulassy and Harlander [GH91] defines an interaction energy as the sum over attractive interaction potentials (e.g. negative Lorentzian or Gaussian potentials) between each measurement and the track. The overall interaction energy is minimized in the fitting process, where the form of the potential automatically rejects outlier measurements being far-off from the track, because the interaction energy for an individual measurement vanishes with increasing distance. For small distances the potential should be approximately proportional to the squared distance to be equivalent to the Least Squares Method in the case of no noise and outliers.

The width of the interaction potential is large in the first iteration to smooth the energy surface and avoid local minima. It is then lowered to a value of a few standard deviations of the measurement error. The choice of the potential and the evolution of its width as well as the minimization method are crucial for the performance of the Elastic Tracking algorithm and need to be optimized for the given problem.

In contrast to the ETA the Elastic Arms algorithm (EAA) by Ohlsson, Peterson and Yuille [OPY92] introduces explicit assignment probabilities for each measurement. Its energy function is therefore a sum of the products of the squared distances times their assignment probabilities. The original algorithm as presented in [OPY92] and applied to the ATLAS geometry in [Lin95] fits all arms and measurements at the same time to find the best set of track parameters and assignment variables for the arms. Measurements which are not assigned to any arm contribute to the energy function with a penalty, which therefore determines the width of the arms.

By means of the BOLTZMANN distribution the energy function is transformed into a probability function which also introduces a “temperature” parameter. This is done to make the algorithm more robust against local minima by flattening the distribution for high temperatures at the beginning.

The extension presented in [FS99] deals with a single arm, but introduces a competition of measurements in one detector layer. This form of the EAA can be seen as the global fitter pendant to the Deterministic Annealing Filter. Therefore the formulae of the EAA are presented in this form here. One defines the energy function as

$$E(\{S_k, s_{ki}\}, \vec{x}) = \sum_k \left[S_k \left(\sum_{i=1}^{n_k} s_{ki} M_{ki} \right) + \lambda \cdot (S_k - 1)^2 \right] \quad (4.29)$$

where M_{ki} is the squared distance between the arm with track parameters \vec{x} and measurement i in detector layer k ; n_k represents the number of measurements in layer k . The assignment variable S_k denotes whether measurements on layer k are assigned or not and s_{ki} the assignment of individual measurements on this layer with $S_k = \sum_i s_{ki}$. The assignment variables s_{ki} and the track parameters \vec{x} are estimated by minimizing the energy function with respect to those variables. The second term in equation (4.29)

introduces a penalty for assigning no measurements in a layer (otherwise minimum or zero energy could always be reached by assigning no measurements at all). The cut-off parameter λ can be seen as the width of the “road” on which measurements are taken into account. Its choice can be crucial if many background measurements exist.

The optimization over all possible combinations of assignments can be simplified using methods from statistical mechanics. This results in the effective energy

$$E_{\text{eff}} = -\frac{1}{\beta} \sum_k \log \left(n_k e^{-\beta\lambda} + \sum_{i=1}^{n_k} e^{-\beta M_{ki}} \right) \quad (4.30)$$

introducing the “temperature” parameter $T = \frac{1}{\beta}$, which is lowered in the course of the optimization process ($T \rightarrow 0$). Formally this expression can be minimized by setting

$$0 \stackrel{!}{=} \frac{\partial E_{\text{eff}}}{\partial \vec{x}} = \sum_k \sum_{i=1}^{n_k} V_{ik} \frac{\partial M_{ki}}{\partial \vec{x}} \quad (4.31)$$

with the assignment probabilities

$$V_{ik} = \frac{e^{-\beta M_{ki}}}{n_k e^{-\beta\lambda} + \sum_{j=1}^{n_k} e^{-\beta M_{kj}}} \quad (4.32)$$

The track parameters \vec{x} are estimated for a first set $\{V_{ik}\}_{i=1, \dots, n_k, k \in \mathbb{N}}$ of assignment probabilities by minimizing the effective energy (4.30) with respect to \vec{x} at high temperature T . A new set of assignment probabilities can be calculated according to the estimated track parameters \vec{x} using (4.32). During the so-called “annealing” these steps are iterated while lowering the temperature parameter.

4.4.2 Deterministic Annealing Filter

The measurements are just used linearly even in the extended Kalman filter as can be seen from equation (4.17). The class of adaptive filters based on the Kalman filter also uses the residuals of the measurements with respect to the predicted track state – called *innovations* – to weigh the individual measurements which yields a non-linear filter. This section provides an introduction into the *Deterministic Annealing Filter* (DAF) as proposed by Frühwirth and Strandlie [FS99].

Nomenclature

The following nomenclature is used throughout this section:

\bar{x}_k real state vector (track parameters) on detector layer k

$\vec{x}_{k|j}$ estimated state vector (track parameters) on detector layer k including the knowledge up to layer j , therefore three cases can arise:

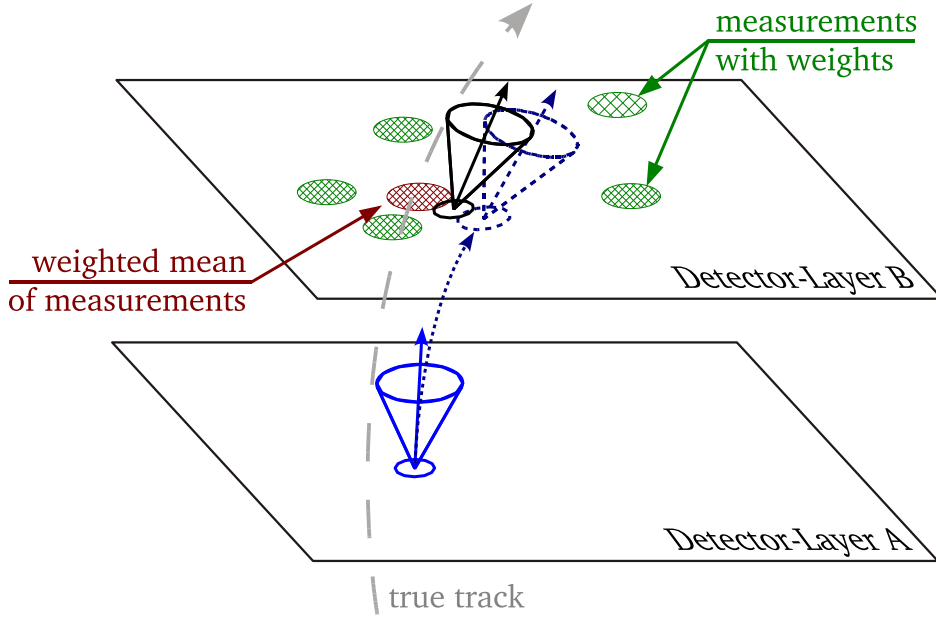


Figure 4.4: *Functional principle of the Deterministic Annealing Filter:* The Deterministic Annealing Filter uses the same principle as the Kalman filter, but several measurements per detector layer are taken into account by using their weighted mean.

1. $k > j$ track prediction
2. $k = j$ estimation of \bar{x}_k
3. $k < j$ smoothed state

$\mathbf{C}_{k|j}$ covariance matrix of the estimation $\bar{x}_{k|j}$

\vec{m}_k^i i th measurement in detector layer k

\mathbf{V}_k^i covariance matrix of \vec{m}_k^i

$\mathbf{G}_k^i = (\mathbf{V}_k^i)^{-1}$ weight matrix of \vec{m}_k^i

p_k^i assignment probability (or weight, not to be mixed up with the weight matrix) of \vec{m}_k^i , i.e. estimated probability that \vec{m}_k^i belongs to the track described by \bar{x}_k

If one has more than one measurement per detector layer or an ambiguous measurement all solutions can be taken into account by introducing assignment probabilities p_k^i for each measurement i in the layer k and by using the weighted mean of these as an *effective measurement*. The general formulae used for the calculation of the effective measurements \tilde{m}_k and the effective covariance matrices $\tilde{\mathbf{V}}_k$ are:

$$\left(\tilde{\mathbf{V}}_k\right)^{-1} \equiv \tilde{\mathbf{G}}_k = \sum_i p_k^i \mathbf{G}_k^i \quad (4.33)$$

$$\tilde{\mathbf{m}}_k = \tilde{\mathbf{V}}_k \cdot \left(\sum_i p_k^i \mathbf{G}_k^i \cdot \vec{\mathbf{m}}_k^i \right) \quad (4.34)$$

The index i runs over all competing measurements in detector layer k , where e.g. in the ATLAS TRT hits are counted twice, because they are interpreted as two measurements in each case, according to a solution where the track passes by “left” and “right” from the wire. The individual measurements are not only weighted by their assignment probabilities, but also the precision of the measurements – given by their covariances – is incorporated. Usually the measurements in one detector layer have roughly the same precision, therefore the formulae may be simplified by dropping the weight matrices in the sums. The effective measurements can be used in the usual Kalman formulae without any change. In contrast to the linear or extended Kalman filter the measurements are not included in a binary way (assigned or not assigned to the track) anymore, but can get every probability between 0 and 1. Figure 4.4 sketches the state update using the weighted mean of the competing measurements.

The remaining and most important part of the Deterministic Annealing Filter is the estimation of the assignment probabilities using the innovations of the individual measurements in competition. This has to be done in an iterative procedure, because the information about the track states is insufficient in the initial phase. After a first pass of the forward and backward filter, however, the smoothed track states provide an estimate of the track states including the information from all layers. Based on this information the assignment probabilities can be calculated and the process of Kalman filtering can be done again with the new effective measurements (figure 4.5).

Assuming the measurement probability density function to be Gaussian ($\vec{\epsilon}_k \propto \varphi(\vec{0}, \mathbf{V}_k)$, cp. equation (4.14)), the non-normalized assignment probabilities ϕ_k^i are proportional to a multivariate Gaussian distribution $\varphi(\vec{x}; \vec{\mu}, \mathbf{V})$

$$\phi_k^i \propto \varphi(\vec{\mathbf{m}}_k^i; \mathbf{H}_k \cdot \vec{x}_{k|n}^*, \mathbf{V}_k^i + \mathbf{H}_k \mathbf{C}_{k|n}^* \mathbf{H}_k^\top) \quad (4.35)$$

where $\vec{x}_{k|n}^*$ is the smoothed track state at layer k without involvement of the measurements on layer k and $\mathbf{C}_{k|n}^*$ its covariance matrix. Neglecting the term $\mathbf{H}_k \mathbf{C}_{k|n}^* \mathbf{H}_k^\top$ in this formula⁶ and introducing $\mathbf{V}_k^i \rightarrow T \mathbf{V}_k^i$ leads to

$$\phi_k^i = \frac{1}{(2\pi)^{\frac{\dim(\vec{\mathbf{m}}_k^i)}{2}} \sqrt{T \det \mathbf{V}_k^i}} \exp \left(-\frac{1}{2T} (\vec{\mathbf{m}}_k^i - \mathbf{H}_k \cdot \vec{x}_{k|n}^*)^\top (\mathbf{V}_k^i)^{-1} (\vec{\mathbf{m}}_k^i - \mathbf{H}_k \cdot \vec{x}_{k|n}^*) \right) \quad (4.36)$$

⁶On the one hand one can reason that the projected covariance of a smoothed state including the information of all measurements is in general much smaller than the covariance of a single measurement. On the other hand “looking at the DAF as an EM algorithm, the state is regarded as fixed during the expectation step (i.e. in the calculation of the weights), and it is therefore conceptually correct to neglect the stochastic nature of the state used in the weight calculations” [Str].

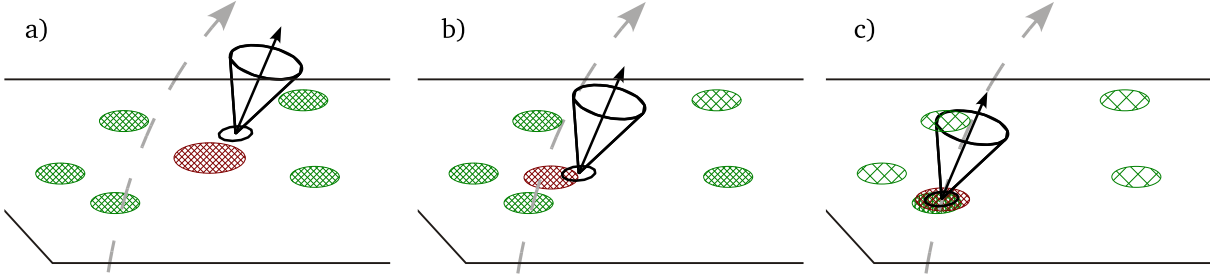


Figure 4.5: *Hit selection using Deterministic Annealing:* a) start of the annealing process at high temperature, all measurements get similar weights; b) assignment probabilities are updated according to the distance from the estimate at lower temperature; c) assignments are frozen out

The “temperature” parameter $T = \frac{1}{\beta}$ (dimensionless with $0 < \beta \leq 1$) is introduced by the deterministic annealing technique to avoid local optima. This factor effectively blows up the covariances of the competing measurements which means that even measurements being farther away from the initial track estimate are taken into account at high temperature.

The weights $\phi_k^i|_{i=1,\dots,n_k}$ are normalized according to

$$p_k^i = \frac{\phi_k^i}{\sum_j (\Lambda_k^j + \phi_k^j)} \quad (4.37)$$

taking the hypothesis into account that no measurement in layer k can be assigned to the track. This is done by the cut term $\sum_j \Lambda_k^j$ with

$$\Lambda_k^j = \frac{1}{(2\pi)^{\frac{\dim(\bar{m}_k^i)}{2}} \sqrt{T \det \mathbf{V}_k^i}} \cdot \exp\left(-\frac{\beta \cdot \lambda}{2}\right) \quad (4.38)$$

The parameter λ defines the cut-off value which is equivalent to a χ^2 -cut if the temperature T gets very low. The meaning of β and λ are analog to the parameters in equation (4.30) of the Elastic Arms Algorithm. The normalization of the assignment probabilities is therewith enhanced compared to the algorithm’s description in [FS99] following a strategy closer to the EAA being for example⁷ used in [SZ99] and [FS06]. Appendix A.2 contains plots showing the behavior of the assignment probability for different parameter values.

⁷The studies presented in [FS99] in fact use the enhanced normalization, too.

A simpler form of the normalization can be used, when differences within the covariances $\{\mathbf{V}_k^i\}_{i=1,\dots,n_k}$ of one detector layer k are neglected

$$p_k^i = \frac{\phi_k^i}{n_k \Lambda_k + \sum_j (\phi_k^j)} = \frac{e^{-\frac{1}{2T} \bar{r}_{k|n}^{*i\top} (\mathbf{V}_k^i)^{-1} \bar{r}_{k|n}^{*i}}}{n_k e^{-\frac{\beta \cdot \lambda}{2}} + \sum_j e^{-\frac{1}{2T} \bar{r}_{k|n}^{*j\top} (\mathbf{V}_k^j)^{-1} \bar{r}_{k|n}^{*j}}} \quad (4.39)$$

where $\bar{r}_{k|n}^{*i} = \vec{m}_k^i - \mathbf{H}_k \cdot \vec{x}_{k|n}^*$ are the residuals of the measurements. The factor n_k in front of the cut term $e^{-\frac{\beta \cdot \lambda}{2}}$ is deduced from the EAA. It is not so important for large values of λ when the cut is usually small compared to the terms in the sum over the competing measurements, but it gets more and more important for small λ . In this thesis it was tried to drop this factor based on the following argumentation. If one measurement i exists with, say, $\bar{r}_{k|n}^{*i} = \vec{0}$ its normalized assignment probability p_k^i will depend on the number n_k of competing measurements in the same group, even if all of them are infinitely away from the track prediction. In fact investigations in the ATLAS TRT showed this can yield in a curious structure in the distribution of assignment probabilities, which may reduce the track parameter resolution (see section 6.2.4). In some of the studies in this thesis the factor n_k was therefore dropped and the following normalization was therefore used

$$p_k^{i*} = \frac{\phi_k^i}{\Lambda_k + \sum_j (\phi_k^j)} = \frac{e^{-\frac{1}{2T} \bar{r}_{k|n}^{*i\top} (\mathbf{V}_k^i)^{-1} \bar{r}_{k|n}^{*i}}}{e^{-\frac{\beta \cdot \lambda}{2}} + \sum_j e^{-\frac{1}{2T} \bar{r}_{k|n}^{*j\top} (\mathbf{V}_k^j)^{-1} \bar{r}_{k|n}^{*j}}} \quad (4.40)$$

4.4.3 Multi-Track-Fitter

The Deterministic Annealing Filter may be extended to fit a bunch of track candidates at the same time. In this case the competition between measurements in being assigned to a single track is supplemented by a competition between tracks. Proposals for such an extension can be found in [SZ99] and [SF00].

The formulae of the Deterministic Annealing Filter presented above can be employed with little modifications. In particular the normalization of assignment probabilities (equation (4.37)) needs to be changed. It is summed over all tracks competing for a measurement to avoid the assignment of a single measurement to more than one track.

5 Software Implementation

This chapter describes the implementational considerations of the Deterministic Annealing Filter in the ATLAS software. A short introduction into the ATLAS reconstruction framework ATHENA will be given, followed by an overview of the offline reconstruction chain for the Inner Detector. It is explained how the Deterministic Annealing Filter (DAF) can be used to extend track candidates from the Silicon layers into the Transition Radiation Tracker. This chapter is closed by a presentation of the ATLAS fast track simulation fatRas which was used to validate the Deterministic Annealing Filter and to test its performance in a well-defined environment. The whole description in this chapter refers to release 12.0.0 of the ATLAS software.

5.1 The ATLAS reconstruction framework Athena

The ATLAS offline software framework ATHENA [ATL04] is based on the component-based architecture Gaudi which is used by the LHCb and the ATLAS experiments. The framework uses object-oriented C++ and introduces some basic concepts having an impact on the implementational considerations of the reconstruction software in general and the Deterministic Annealing Filter in particular.

- Abstract interfaces are used for all components of the code. This allows one to interchange parts of the software and reflects the hierarchy of data objects hiding specializations and implementational details from the users. A track fitter, for example, is just interested in the position of a measurement and its error, but it does not care whether the measurement was performed by the Pixel detector or the SCT. This reduces compile-time dependencies and makes the code more general.
- Data objects and the algorithmic part of the code are clearly distinguished. This allows one to interchange the algorithms at runtime without the need to recompile any code. It is possible for example to use a χ^2 -fitter instead of a Kalman filter just by modifying the job options controlling the reconstruction.
- Data objects should be constant, i. e. their basic properties cannot be modified after creation. This design principle can help to avoid clashes between different algorithms working with the same data objects; it is not required by the ATHENA framework itself though, but recommended by the Event Data Model.

This list is just a selection of concepts being most important for the DAF implementation. The Computing Technical Design Report [ATL05] provides a comprehensive overview of the ATLAS software.

The software distinguishes *Algorithms* and *AlgTools*. The former correspond to specific steps in the reconstruction chain and are called from the top steering algorithm of ATHENA according to the end-users job-options. They do not directly interchange data with each other, but read and write their data from the transient data store called StoreGate. The latter can be invoked from any Algorithm or other AlgTool and communicate directly through their interfaces. A track fitter for example is realized as an AlgTool getting the measurements to fit passed through a function call and returns the fitted track.

5.2 Inner Detector track reconstruction

For the Inner Detector reconstruction exist two monolithic packages called iPatRec and xKalman and a new modularized version following the design principles mentioned above. The new modularized tracking – referred to as “NewTracking” here – is based on the reconstruction chain as used by xKalman, but introduces many new algorithms like the Gaussian Sum Filter or the Deterministic Annealing Filter. The following sections describe the reconstruction chain of the NewTracking.

In general the Inner Detector reconstruction is designed as an inside-out tracking. 3-dimensional measurements from the Pixel and SCT detectors are used to form track candidates which are extended into the TRT afterwards. The full tracks are the input for vertex algorithms trying to reconstruct primary and secondary vertices. In the future it will be possible to start a second-stage pattern recognition in the TRT using all TRT measurements not yet assigned to a track to reconstruct conversions and other vertices in the outer layers. The reconstruction chain consists of the following steps

1. Data preparation. The raw data from the detector is transformed into **RawData-Objects** by bytestream converters. A **RawDataObject** (RDO) corresponds to a single measurement, e. g. a single pixel in the Pixel detector.
2. Clusterization. Neighboring Pixels and SCT strips are clustered into **Prep-RawData** (PRD; alias **ReconstructionInputObject**, RIO) to form groups of measurements on the same module which are believed to belong to the same energy deposition.
3. Space point formation. **SpacePoints** represent a 3-dimensional measurement, they are created directly from Pixel clusters or by combining two SCT clusters from stereo-layers. As described in section 3.2.2 the SCT modules consist of two sides with strips having a small stereo-angle between each other. Combining both sides allows one to give a rough estimate of a 3-dimensional track position.

As it is not known which combination of clusters from the two sides is correct, many fake **SpacePoints** will be created in this step. The small stereo angle of 40 mrad keeps the ghost rate lower compared to a setup with 90° stereo angle, though.

4. Track finding in the silicon detectors.

- a) Seeds for tracks are created from the **SpacePoints** by searching for **SpacePoints** lying on a straight line.
- b) Pixel and SCT **PrepRawData** (clusters) which are compatible with a seed are searched for and transformed into **RIO_OnTrack** objects. Special calibrations can be applied in the transformation from **PrepRawData** to **RIO_OnTrack** which need a rough track estimate. This is necessary for TRT measurements to solve the left/right ambiguity and for error calibration using the track intersection and track angle in the Pixel and SCT detectors. These corrected measurements are used in a track fit.
- c) Ambiguity processing. Ambiguities due to ganged pixels are solved and measurements assigned to several tracks are identified. In this process also “bad” tracks are sorted out.

5. Track extension into the TRT.

- a) TRT straws being compatible with extrapolated silicon tracks are fed into a local pattern recognition which takes into account the drift radius to decide on an extension candidate. The drift circles (**PrepRawData**) are transformed into **RIO_OnTrack** objects using the extrapolated track to calibrate the TRT measurements. The calibration includes the choice of the drift radius sign (“left” or “right” from the wire) and corrections based on the track prediction of the local z -coordinate along the wire.
- b) The measurements from the Pixel, SCT and TRT detectors chosen in the previous processes are fitted by a track fitter.
- c) Based on a scoring of the track it is decided whether the silicon-only track from step 4 or the extended track is used in the further analysis.

5.2.1 Extrapolation process and track representation

The task of extrapolating track parameters through the detector while embodying material effects like multiple scattering is performed by special **AlgTools**. Instead of the very detailed detector description used in full simulation, those **AlgTools** use a simplified tracking geometry for speed reasons. The tracking geometry in the Inner Detector reflects the whole material in the form of layers [Sal04].

The TrackingGeometry is fully connective to allow for a fast prediction of the path of a track through the detector volumes. Sensitive detector elements are grouped into layers within each volume and are represented by surfaces where the surface type, i. e. the geometrical properties and the coordinate system, is adapted to the detector type. The TrackingGeometry is created by parsing the full ATLAS detector description GeoModel. The detector material is not regarded continuously, but concentrated after each layer.

The whole extrapolation process in ATLAS has been divided into

1. navigation between volumes and layers
2. mathematical propagation of track parameters and their related error variances
3. integration of material effects

where different implementations for every function may exist. The mathematical propagation for example can be done analytically using a straight line or helix approximation or numerically using the detailed magnetic field map. The material of an active detector layer is always introduced in the extrapolation which leaves the layer, if the parameters are extrapolated along momentum and in the extrapolation reaching the layer, if extrapolated opposite momentum. Multiple scattering is included by enlarging the entries of the covariance matrix related to the direction of the track depending on its momentum. Adding straggling terms to the covariances complies with the Gaussian core of the scattering distribution which can be derived from Molière's theory of multiple scattering. Energy loss can occur mainly due to ionization, bremsstrahlung, direct pair production and photonuclear interactions. In wide ranges of the interesting track momenta the energy loss can be described by the Bethe-Bloch and the Bethe-Heitler formulae. Special AlgTools calculate the most probable value for the energy loss which is then included in the estimate of the track parameters by decreasing – or increasing, depending on the extrapolation direction – the track momentum. Additionally the covariances are adapted to take the uncertainties into account.

Iterative fitters, like the Kalman Filter and the DAF, therewith automatically include material effects during the extrapolation process. Global Least Squares fitter however have to introduce multiple scattering and energy loss by extra parameters in the objective function (cp. [Cor06]).

The reconstructed tracks themselves correspond to a data class named **Track** in the ATLAS software being a vector of track states on different detector surfaces (**TrackStateOnSurface**) provided by the tracking geometry. One **TrackStateOnSurface** itself can stand for several types of information about the track. The most widely used version is a measurement on the track containing a link to the **RIO_OnTrack** and to the **TrackParameters** estimated by the fitter. Other types are outliers, meaning measurements not taken into account in the track fit, because the fitter rejected them, or a **Perigee** containing only the track state at the origin. A full list of the different

kinds of `TrackStateOnSurfaces` and a comprehensive summary of the `Track` object can be found in [AAC⁺06]. This paper describes the data objects in the tracking realm complying with the Event Data Model (EDM).

5.3 Deterministic Annealing Filter implementation

This section briefly describes how the DAF was implemented in ATLAS NewTracking in the course of this work. All considerations were guided by the request to avoid code duplication as much as possible to reduce the later time and effort of maintenance. Additionally the implementation should be as flexible as possible to be able to incorporate enhancements.

Equations (4.33) and (4.34) on page 27 show how to integrate the Kalman Filter into the Deterministic Annealing Filter. The DAF implementation therefore makes use of the existing Kalman filter from package `TrkKalmanFitter`. To be able to use the existing fitter, a new data object named `CompetingRIOsOnTrack` was created. It is possible to run a track fitter with the new object, because a new pure abstract base class for `RIO_OnTrack` and `CompetingRIOsOnTrack` named `MeasurementBase` was introduced at the same time. This allows fitters to work completely with `MeasurementBase` without having to know about `CompetingRIOsOnTrack`.

A `CompetingRIOsOnTrack` contains one or more `RIO_OnTracks` of the same concrete type in one “effective detector layer” (i. e. possibly from more than one detector surface) which compete against each other in being assigned to a track.

The way this “effective detector layer” is defined depends strongly on the sub-detector type and even different definitions may exist for special reconstruction purposes. The single local parameters and local error representations enforced by the base class describe the mean values \tilde{m}_k and $\tilde{\mathbf{V}}_k$ according to the weights or assignment probabilities p_k^i associated with each `RIO_OnTrack`.

The `CompetingRIOsOnTrack` object is contained in a package of its own and is the abstract base class for derived classes in each detector sub-system. As figure 5.1 details, the base class contains only the vector of assignment probabilities and some basic information to handle a given number of hits while the associated `Surface` and the vector of `RIO_OnTrack` objects are implemented in the concrete classes. This separation allows the derived classes to give back also the specific type of `Surface` and `RIO_OnTrack`, avoiding extensive type identification at run-time (RTTI). The `CompetingRIOsOnTrack` object is general enough to be utilizable for other purposes than the DAF as well, e. g. they may be used for a future Multi-Track-Fitter implementation (see section 4.4.3).

Before the DAF fit can be started, a coarse pattern recognition has to be done which groups measurements compatible with a track candidate, but ruling out each other, into `CompetingRIOsOnTrack`. This pattern recognition is described in more detail for the TRT in section 5.4. Objects of the class `CompetingRIOsOnTrack` are created

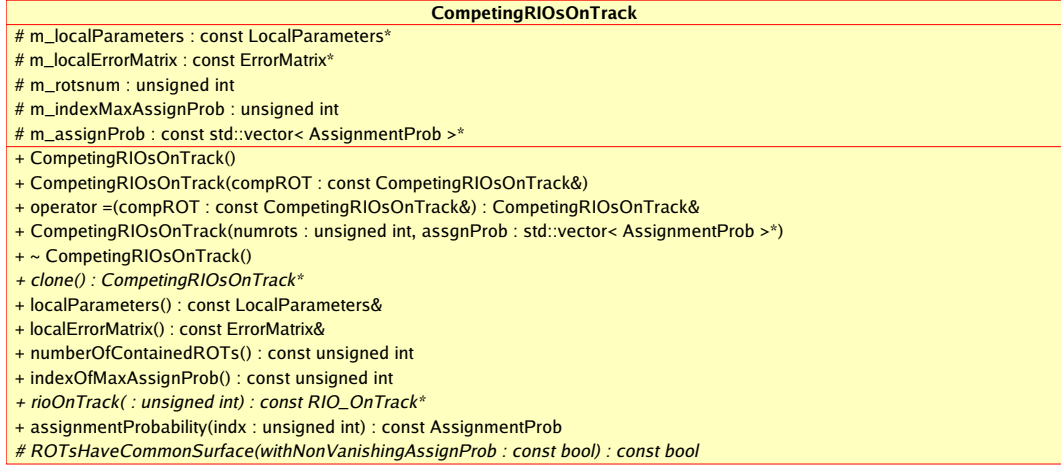


Figure 5.1: UML diagram showing the interface of *CompetingRIOsOnTrack* objects

by a special AlgTool (*CompetingRIOsOnTrackTool*) to ensure the data contained in one object to be consistent¹. In contrast to most EDM objects the *CompetingRIOsOnTrack* can be modified by the *CompetingRIOsOnTrackTool*, but only in a limited way: Just the assignment probabilities of the contained measurements can be changed afterwards. This specialty was introduced to avoid the need to recreate all *CompetingRIOsOnTrack* at each annealing iteration of the DAF.

The assignment probabilities themselves according to equations (4.36) and (4.37) are not calculated in the *CompetingRIOsOnTrackTool* (respectively its detector specific implementations), but in a separated AlgTool named *DAF_WeightCalculator*, because the calculations are independent from the detector type and it is possible to exchange the formulae by using another tool. Other types of weights and normalizations may be interesting for optimizations and extensions of the Deterministic Annealing Filter. The current implementation of the *DeterministicAnnealingFilter* uses the smoothed states $\vec{x}_{k|n}$ in the call of the *DAF_WeightCalculator* instead of the smoothed states $\vec{x}_{k|n}^*$ without involvement of the measurements on layer k . Since competition between measurements is just used for the TRT yet, where about 36 measurements exist, the difference is rather small and can be neglected. Future versions will correct this

¹Following a general design principle of the new ATLAS offline software, data objects should just contain data, but not any algorithmic code. This even excludes difficult consistency checks in the constructor of the objects. To ensure consistency EDM objects should only be instantiated through their related “maker tools”. The *CompetingRIOsOnTrackTool* on the other hand is just a wrapper for the detector specific implementations of the concrete tools. There exists one tool for each detector specific type of *CompetingRIOsOnTrack* (e. g. the *CompetingTRT_DriftCirclesOnTrackTool* for *CompetingTRT_DriftCirclesOnTrack*). This allows one to perform specialized tasks for each type (including tasks which need detector specific information not available in the general tracking realm) while client tools just use the wrapper *CompetingRIOsOnTrackTool* not needing to know the concrete type of the *CompetingRIOsOnTrack* object.

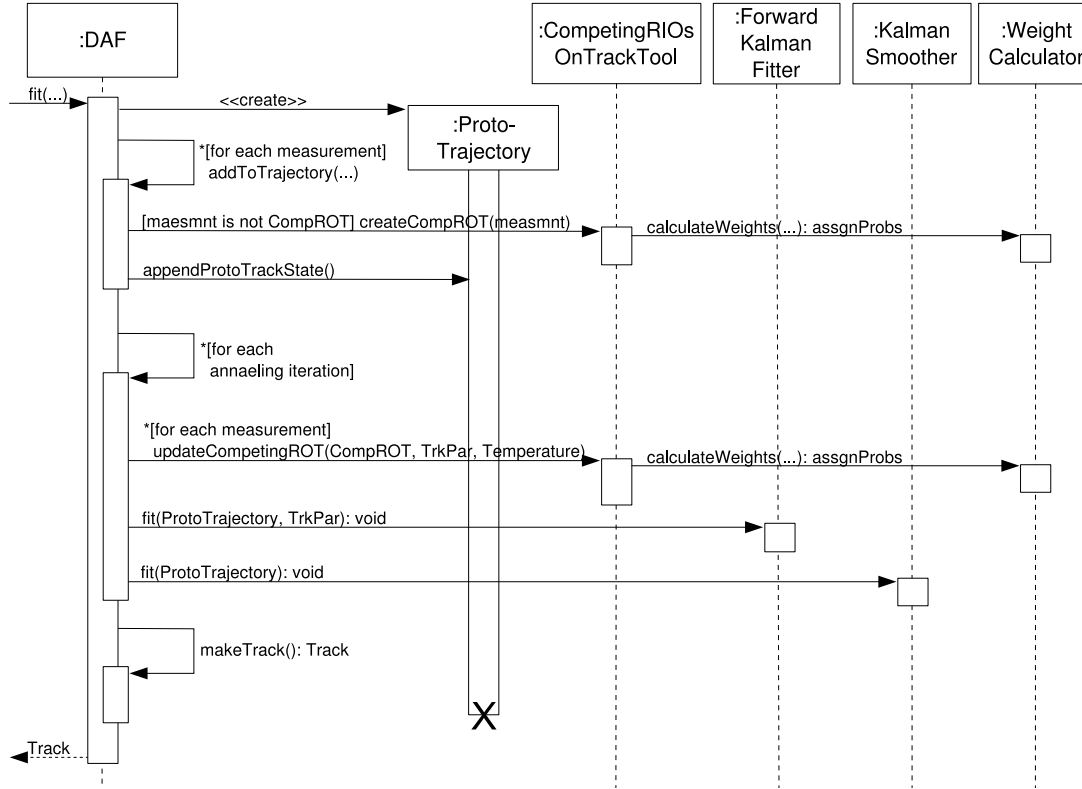


Figure 5.2: Simplified UML sequence diagram for the `DeterministicAnnealingFilter`:

variation.

In a first version of the implementation, the DAF called the `KalmanFitter` via the abstract interface `ITrackFitter` in every annealing iteration. As described in section 5.1 a tool is not allowed to change a `Track` after its creation. This means a new `Track` must be created in every iteration, creating a huge overhead due to deep-copies of rather heavy objects. To avoid this the DAF implementation was changed to call the sub-tools `ForwardKalmanFitter` and `KalmanSmoother` of `TrkKalmanFitter` directly and an internal trajectory object consisting of a new object named `ProtoTrackStateOnSurface` (defined in `TrkFitterUtils`) was created. This internal trajectory as a non-standard EDM object is used by `DeterministicAnnealingFilter` and `TrkKalmanFitter` during the annealing iterations and the outlier identification respectively; the final `Track` object is created only in the end. Figure 5.2 shows a simplified UML sequence diagram for the `DeterministicAnnealingFilter`.

The Deterministic Annealing Filter in its ATLAS implementation can be used as “stand-alone track fitter” without any further pattern recognition to refit tracks in the Inner Detector. In this case the `DeterministicAnnealingFilter` itself transforms measurements in the TRT into `CompetingTRT_DriftCirclesOnTrack` and therefore introduces competition between the “left” and “right” solution of each measurement.

Even this simple application of the DAF technique can be used to improve the fit quality of tracks. The investigations in section 6.1 show examples for this kind of tests.

To get the full functionality of the DAF for TRT reconstruction it is needed, though, to replace the standard pattern recognition, which assigns a unique drift circle per layer, and to perform a simple pattern recognition in the TRT finding all measurements being compatible with a track prediction from the the silicon layers. This pattern recognition is described in the next section.

5.4 Extension of silicon tracks into the TRT using deterministic annealing

As explained in section 5.2, the Inner Detector reconstruction starts with a track reconstruction in the Pixel and SCT detectors and tries to extend those tracks into the TRT afterwards. This section describes how tracks can be extended into the TRT using the DAF.

The previous steps of the track reconstruction provide a collection of `Tracks` just containing measurements from the silicon layers. The following steps are performed for each of these tracks:

1. Extension finding
 - a) A “road” of `DetectorElements`² through the TRT is built based on the extrapolated positions of the silicon track.
 - b) Measurements found on the road are grouped into clusters of mutually exclusive measurements along the path of the track prediction. A `CompetingTRT_DriftCirclesOnTrack` object is created for each cluster, setting the assignment probabilities according to the initial temperature of the annealing scheme and the distance to the extrapolated track.
2. Extension processing
 - a) The silicon track and the related vector of `CompetingTRT_DriftCirclesOnTrack` are fitted using the `DeterministicAnnealingFilter`.
 - b) Based on a scoring of the track it is decided whether the silicon-only track or the extended track is used in the further analysis.

The grouping of measurements into clusters of mutually exclusive measurements is a crucial task for the DAF-based reconstruction in the TRT. In contrast to the Pixel

²`DetectorElements` correspond to small units of the sub-detectors, e. g. a Pixel module or a layer of TRT straws in one of the TRT modules.

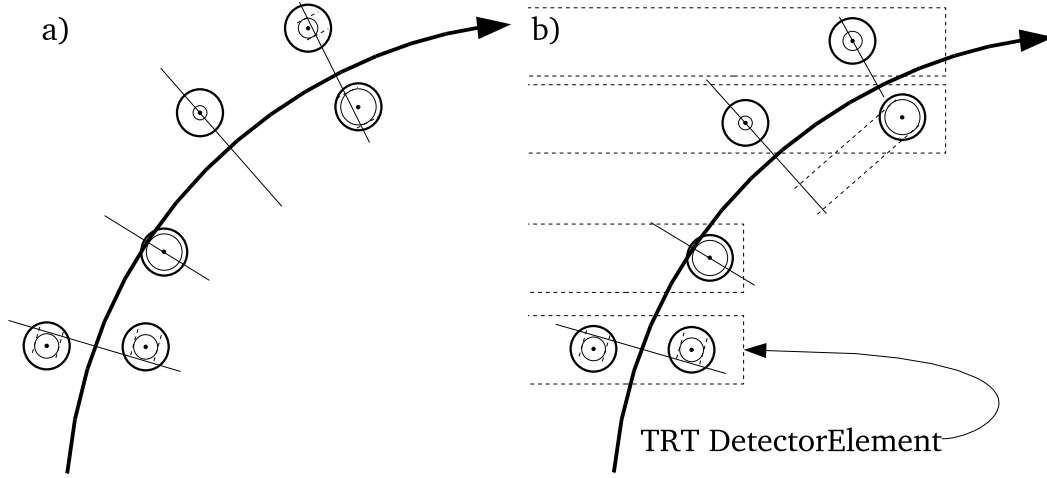


Figure 5.3: *Strategies for the grouping of mutually exclusive measurements in the barrel TRT:* a) shows the result for the more sophisticated method with “effective” detector layers perpendicular to the track prediction; b) **DetectorElement**-wise grouping of the same measurements fails in the region where the track is not perpendicular to the **DetectorElements** (indicated by the dashed boxes) anymore. In both cases the drift radii of the measurements are projected on a common surface of each group. The common surfaces for each group are drawn as solid lines and the applied projections are represented by dashed lines.

and SCT detectors where the layers are canonically given by the detector modules, it is not self-evident where the effective layers of mutually exclusive measurements lie in the barrel TRT. For high- p_T tracks which are only little bent and therefore nearly perpendicular to the layers of TRT straws given by the **DetectorElements**, the choice of one **CompetingTRT_DriftCirclesOnTrack** per **DetectorElement** seems to be intuitive. For lower p_T tracks the “correct” choice is not so easy to take.

In the end-cap TRT all measurements of the same **CompetingTRT_DriftCirclesOnTrack** lie on one of the “wheels”, giving a clear allocation. For the barrel TRT two grouping strategies exist:

- a) grouping in “effective” detector layers perpendicular to the track prediction
- b) **DetectorElement**-wise grouping, appropriate for high- p_T tracks

The results for both strategies in the case of a low- p_T track are sketched in figure 5.3.

In both cases the drift radii projected on a surface are common for all measurements of the **CompetingTRT_DriftCirclesOnTrack**. Usually the associated surface of the measurement (**TRT_DriftCircleOnTrack**) with the highest assignment probability will be used as common surface to keep inaccuracy due to the projection small. The

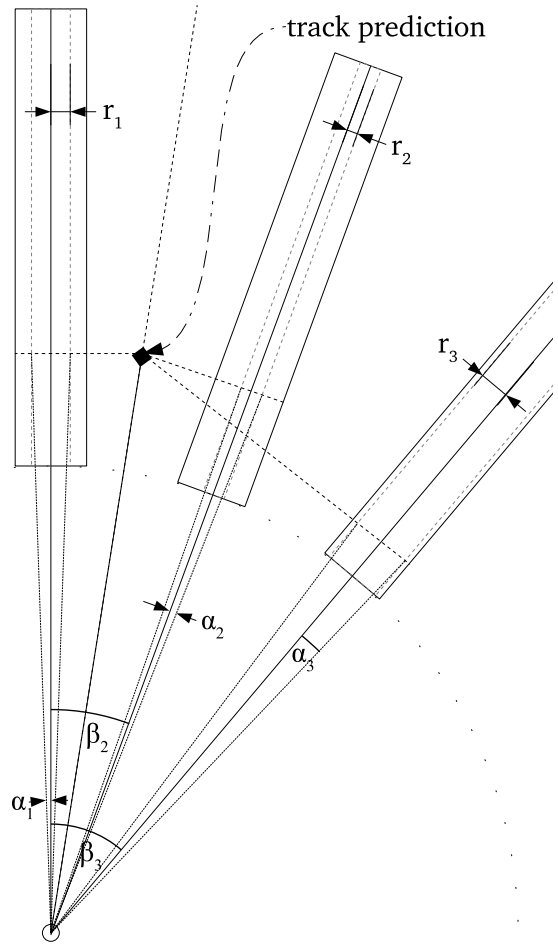


Figure 5.4: *Calculation of the mean measurement in the TRT end-caps:* Using the radial component of the track prediction the drift radii are transformed into polar coordinates.

associated surface of a `CompetingTRT_DriftCirclesOnTrack` may therefore change in the course of the annealing procedure.

The straws in the barrel TRT are all parallel to each other simplifying the projection. The projection of measurements from different straws onto a common surface is more complicated for the TRT end-caps. The straws are radially oriented in wheels, so it was decided to represent the mean measurement in polar coordinates on a disc surface. For the calculation of the mean measurement in polar coordinates the knowledge of the track prediction (more precisely its radial component) is required as figure 5.4 shows. If only the two measurements belonging to a single straw remain with non-vanishing assignment probabilities the associated surface of this straw will be used, so no projection is needed anymore. The transformation of the drift radius measurements into polar coordinates can just be done approximately and it should therefore be avoided if possible. In the end caps measurements are therefore already neglected and their probability is set to zero by the `CompetingTRT_DriftCirclesOnTrackTool`, if their assignment probability is small ($p_k^i \leq 10^{-5}$).

The `DeterministicAnnealingFilter` itself contains a strategy to handle down-

weighted `CompetingRIOsOnTrack`. If the sum of assignment probabilities $\sum_i p_k^i$ within a group of competing measurements is very small, the covariance of their effective measurement will be huge. This may lead to numerical problems in the Kalman-steps. The DAF therefore ignores `CompetingRIOsOnTrack` with $\sum_i p_k^i < 10^{-20}$ during the Kalman filtering and smoothing. But the assignment probabilities of these measurements are also recalculated in each annealing iteration, making it possible to re-introduce them, when the track prediction is adjusted.

As shown in figure 5.2, the `DeterministicAnnealingFilter` converts the intermediate proto-trajectory into a complete `Track` after the last annealing iteration. The track states belonging to a `Track` can be marked as “Outlier” if they were not used during the track fit. Due the assignment probabilities this definition is fuzzy for the DAF and it was chosen, that `CompetingRIOsOnTrack` with $\sum_i p_k^i < 0.2$ are marked as Outliers on the final `Track`. `CompetingRIOsOnTrack` with $\sum_i p_k^i < 10^{-20}$ after the last annealing iteration are dropped and not written to the output `Track`. This is needed, because the number of outlier measurements belonging to the track would be very large for the DAF-based TRT track extension if far-off outliers were kept. The number of outliers however is used in the track scoring and to identify electron tracks with energy loss. The artificially high number of outliers would spoil this.

5.5 ATLAS fast track simulation fatRas

Validation of tracking algorithms is not a trivial task, since many different parts of the code, like extrapolation, detector and material description and track fit, interact with each other in a complicated way. Additionally many different kinds of detectors with different measurements (2-dimensional pixel position, 1-dimensional silicon strips, drift radii, etc.) have to be combined needing various transformations of coordinate frames. Especially the drift time information of the TRT introduces many possible problems: It just gives a distance from a (potentially sagged) wire, but no information along the wire, which is needed though for calibration. A powerful validation framework to test all parts of the tracking code in a clean and well-defined environment is therefore absolutely necessary.

The so-called ATLAS fast track simulation fatRas was developed under the direction of A. Salzburger to provide such a validation framework. fatRas uses the same extrapolation and navigation tools as the reconstruction. Problems in the navigation through layers and volumes including the difficult task of consideration of material interactions can directly be identified [SWFL06].

The simulation allows one to simulate many tracks with well-defined parameters very fast to do detailed tests on the performance of track fitters. The fatRas simulation provides several modes of operation to check diverse parts of the reconstruction chain and to separate the influences of the reconstruction steps:

- extrapolation in validation mode for tests of navigation, extrapolation and material interaction
- simulation of measurements with user-defined detector resolution
- creation of a simulated `Track` object as truth reference or for tests of track fitters using a pure refit without pattern recognition
- simulation of detector noise including data post-processing as input for pattern recognition to validate the whole reconstruction chain
- various input methods for simulated tracks:
 - single track events with different particle hypothesis
 - simulation of tracks originating from a vertex
 - input from event generators to simulate physics events

In the course of this thesis the post-processing as a preparation for pattern recognition was implemented and some work was done on the simulation of measurements. Both parts of `fatRas` will be explained in the following sections.

5.5.1 Track simulation

The simulation of tracks in `fatRas` makes use of the extrapolator tools of the reconstruction framework (see section 5.2.1) with some modifications. The tools for the integration of material effects are replaced by special versions implementing a Monte Carlo simulation for multiple scattering and energy loss. It is also possible to use a modified version of the `TrackingGeometry` in `fatRas`.

The track parameters on the active detector layers provided by the modified extrapolation are converted into full `Tracks` by a special track creator tool. Based on the track parameters measurements are created on the detector surfaces. `PrepRawData` and `RIO_OnTrack` objects are both created including measurement smearing. This means the position of the measurement is shifted relative to the simulated track position. In the Pixel and SCT detector smearing is done according to a flat distribution with width equal to the Pixel dimensions and the SCT strip width, respectively. In the SCT positions are just smeared perpendicular to the strip direction regarding the strip rotation in the SCT end caps. A Gaussian distribution with standard deviation equal to the detector resolution is applied in the TRT. Holes on the track can also be simulated to take detector efficiencies into account.

The `Tracks` created in this simulation step can already be refitted by an arbitrary track fitter for studies without pattern recognition and they contain the truth parameters for comparisons between simulation and reconstruction. The track parameters

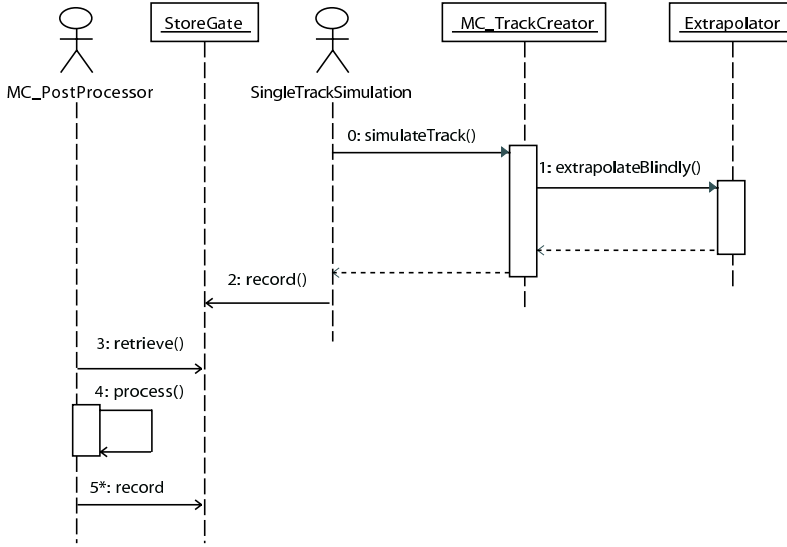


Figure 5.5: *Simplified UML sequence diagram for the fatRas simulation:* The track simulation and the post-processing algorithm are illustrated as actor nodes. Data exchange between them is done through the transient data store StoreGate (from [SWFL06]).

obtained in a refit have realistic variances because the measurement smearing propagates to the track parameters, even though effects of inefficiencies in the pattern recognition are not included.

5.5.2 Noise creation

Full studies of the track reconstruction process including pattern recognition need a post-processing of the simulated **Tracks**. The “raw measurements” in form of **PrepRawData** are extracted from the simulated **Tracks** and written into different StoreGate collections which can be accessed by the pattern recognition algorithms. Figure 5.5 illustrates the simulation steps in form of an UML sequence diagram.

The post-processing can also simulate noise measurements during the distribution of **PrepRawData** into the StoreGate collections. Arbitrary noise occupancies can be simulated in each sub-detector. The noise levels specify the probability for a noise measurement per pixel, silicon strip or drift tube, respectively. In the Pixel and SCT detector noise measurements are just added to the measurements produced by simulated tracks. They are uniformly distributed over the whole active detector elements. In the TRT it is decided for each straw tube individually, whether noise is created or not. If a noise measurement is simulated in a certain tube, all measurements belonging to tracks are masked. This means the track **PrepRawData** are not moved to the measurement collections, but to a special collection which is just needed for memory management. Similarly only one measurement will be used further on, if more than one track in an event produced a measurement in the same tube. The drift radii of the noise measurements are simulated according to a flat distribution between 0 mm and the tube radius of 2 mm.

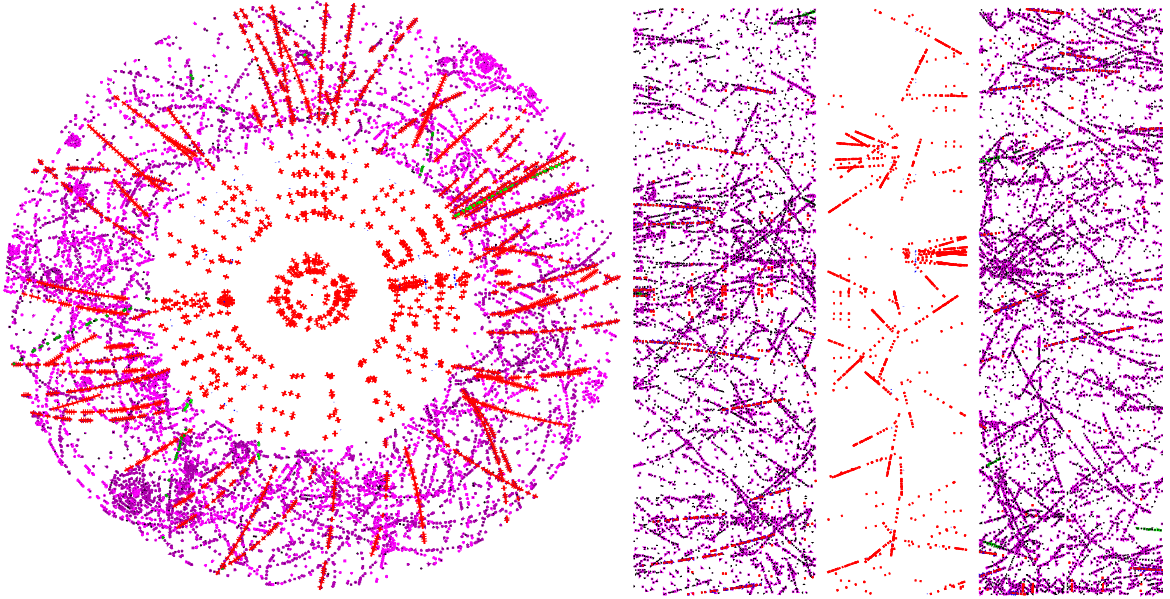


Figure 5.6: *Track plots of a top event: $X - Y$ view of the barrel part (left) and $\phi - Z$ view of the endcap part of the TRT (right). Measurements in the Pixel and SCT layers can be seen in the center of each plot.*

5.6 Further validation tools

For a detailed analysis of the track fit performance and the identification of problems some data output and visualization tools were developed. Only two of these tools will be presented here briefly. A more comprehensive reference can be found in appendix C.

The fatRas simulation can create a reference `Track` containing the true track parameters and the measurements (as `RIO_OnTrack`, i. e. they contain the information about the left and right solution for drift circles) created by the simulation. A very detailed study of the reconstruction performance is therefore possible by comparing the simulated `Track` object with the reconstructed one. Using the full ATLAS Monte Carlo simulation (based on Geant 4) comparisons on track and measurement level are much more difficult, since the truth objects have another structure as the reconstruction objects and do not contain the whole data needed for all validation purposes³. To

³Full simulation and its truth information do not allow to do a detailed comparison, because in full simulation just weights exist, which describe how much a generated track (just given by its perigee parameters) contributed to a measurement (as `PrepRawData`). Track parameters of the simulated tracks are just available at the creation point of a particle within its decay chain. Therefore track parameters on arbitrary surfaces are only available using a later extrapolation within the reconstruction framework; due to multiple scattering the extrapolated parameters may differ from the ones derived by Geant 4 and it is not possible to get a reliable estimate of the sign of the simulated drift radius in the TRT.

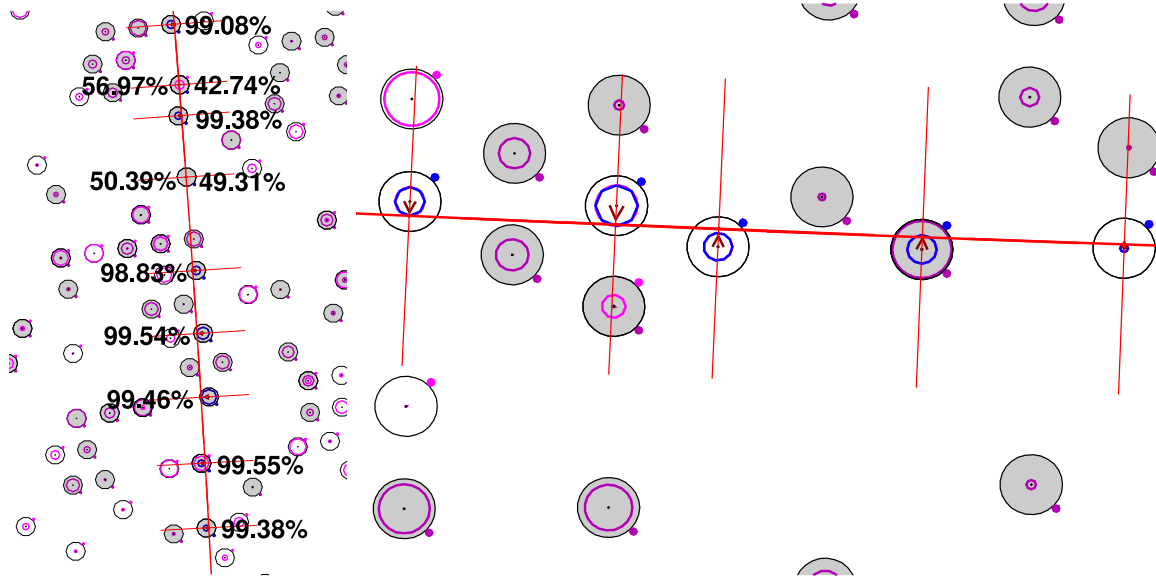


Figure 5.7: *Track plots ($X - Y$) in the barrel TRT:* DAF reconstructed track including assignment probabilities (left) and single track surrounded by noise measurements (right). Drift tubes are drawn as black circles including the straw position. Purple circles represent drift radii of raw measurements (`PrepRawData`). Blue circles illustrate drift radii of measurements (`RIO_OnTrack`) used in the track fit where the red arrowhead points in the direction of the chosen left/right solution. The small, filled circles near to the tubes indicate whether the measurements belong to the straw section with $Z > 0$ or $Z < 0$; tubes containing measurements with $Z < 0$ are additionally grey shaded. Assignment probabilities vanishing within the precision shown are omitted in the left plot. The reconstructed track itself is given by the red line with lines perpendicular to the track direction at the positions of track states.

exploit this advantage of `fatRas` for tracking validation a special tool was developed which compares two tracks `TrackStateOnSurface`-wise. Following the well-known “diff” command this tool was called `TrackDiff`.

In its current version the `TrackDiff` tool prints detailed reports about the compared track states into the message stream in `VERBOSE` mode and summaries of the number of differences at the end of its execution. It also allows one to write information about each difference into a ROOT ntuple. This includes missing or faked measurements including the recognition of measurements marked as outliers and comparisons on measurement level, like the left/right solution for TRT hits.

Another tool developed for detailed validations of track reconstruction in the Inner Detector is a visualization tool, named `TrackPlotter`. This tool is implemented as a stand-alone (i. e. not dependent on the ATHENA framework) ROOT-based application. It takes the data to be plotted from a ROOT ntuple which can be created by the

tracking validation ntuple tools, also developed in the course of this thesis. The **TrackPlotter** uses a 2-dimensional projection like the ATLAS standard visualization tool ATLANTIS. Tracks and measurements as **PrepRawData** and **RIO_OnTrack** can be visualized with the **TrackPlotter** in a $X - Y$ view (appropriate for the barrel TRT) and a $\phi - Z$ view (appropriate for the end cap TRT) including a Graphical User Interface. The **TrackPlotter** provides a more detailed view in the Inner Detector than the event display ATLANTIS which is needed for special validation tasks (figure 5.7).

6 Validation and performance studies

Most performance studies of the Deterministic Annealing Filter in ATLAS were done on fatRas simulated events (see section 5.5). Several reasons exist for this choice:

- As described in section 5.6 it is not possible to do all kinds of comparisons between simulation and reconstruction with the truth objects derived from the Geant 4 simulation. For example one cannot check whether the correct solution for left/right ambiguities of TRT measurements was found. Some of those numbers are very important criteria for the reconstruction quality and give hints where problems remain.
- fatRas allows one to simulate large numbers of tracks with well-defined properties rather quickly. Different simulation parameters can easily be modified to validate track fitters under varying conditions. The noise occupancy in the sub-detectors for example is a fundamental parameter for pattern recognition and track fit.

The studies presented here do not cover every performance study and validation one can think of. They are just meant as a first estimate of the track reconstruction performance using the Deterministic Annealing Filter in comparison to the classical way. Even before reliable estimates of the performance can be given, it is needed to validate the implemented data classes and algorithms. This task is very complex for track fitters in ATLAS because diverse kinds of measurements have to be considered and track fitting strongly depends on other tasks like extrapolation which may fail. On the other hand the DAF itself and also the algorithms used for coarse pattern recognition offer a variety of parameters which have to be adjusted. This chapter also presents studies of the dependency of the reconstruction performance on some of those parameters.

All studies were performed with ATHENA release 12.0.2 using some additional package versions which are listed in appendix B.1. The annealing procedure was restricted to the TRT, i. e. measurements in the Pixel and SCT layers were always used with full weight.

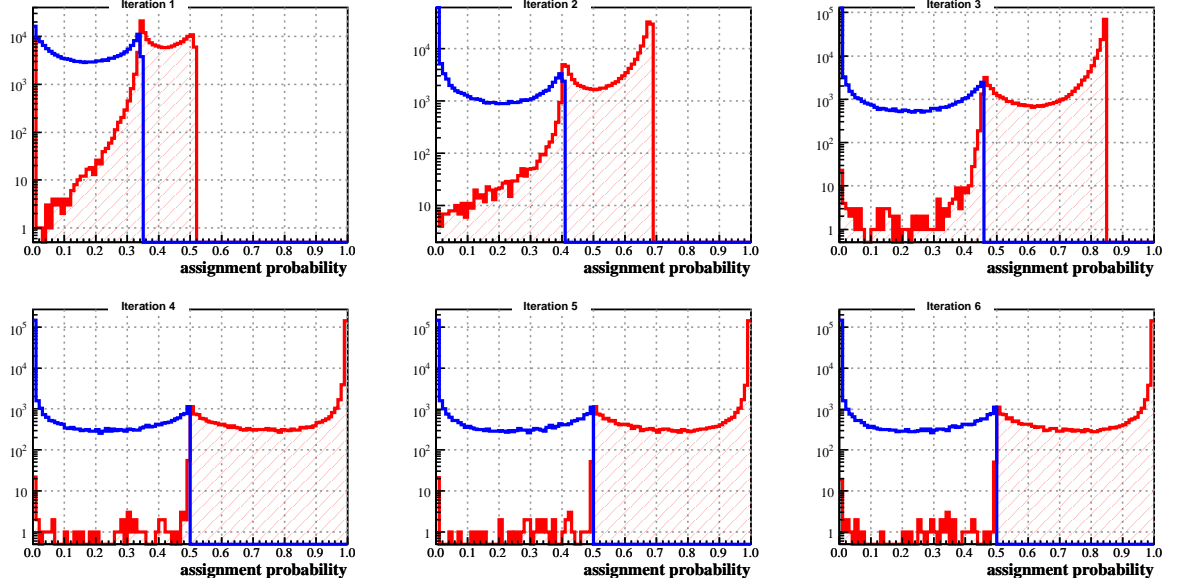


Figure 6.1: *Distribution of the maximum and minimum assignment probability for each group of competing measurements in the TRT: Blue histogram without shading: Minimum assignment probability $\min_{i=1}^{n_k} p_k^i$; red histogram with dashed area: Maximum assignment probability $\max_{i=1}^{n_k} p_k^i$. The histograms show the evolution of the assignment probabilities in the course of the annealing iterations using the schedule $T = 81 \rightarrow 9 \rightarrow 4 \rightarrow 1 \rightarrow 1 \rightarrow 1$. 5000 muon tracks with $|\eta| < 0.5$ and total momentum of 10 GeV were refitted using annealing for TRT measurements.*

6.1 Refitting of tracks in the Inner Detector

A very basic test of the track fit can be done by taking the simulated tracks and refitting them with the DAF. In this case one avoids influences of the coarse pattern recognition and the fit itself can be validated. The annealing is less important because no noise measurements exist, but the quality of left/right decisions is tested.

In the following tests the truth tracks as created by fatRas were fed into the Deterministic Annealing Filter with smeared true track parameters as initial parameters. The smearing of the initial parameters is needed, because the DAF otherwise would start with a too good estimate which does not only affect the initial assignment probabilities, but also the fit of the track parameters. Other studies revealed that even a pure Kalman fit is biased towards the true solution, if the initial parameters are perfect. This dependency on the initial parameters of the Kalman fitter and DAF implementation need further studies in the future. It is introduced due to the fact that one needs to do an update of the initial track parameters with the first (mostly the innermost) measurement (see equations (4.17) and (4.18)). In principle one has to assign infinite covariance (or zero weight) to the initial parameters to avoid their

influence which is obviously not possible. A sufficiently small weight is used instead, but its choice is still critical.

Figure 6.1 shows the distribution of assignment probabilities in the course of the annealing iterations. The probabilities for both solutions (i. e. left and right solution for each TRT measurement) are given in red (maximum) and blue (minimum) respectively. At first one observes an increase in the maximal possible probability due to the drop in temperature. At the same time the separation between maximum and minimum values gets stronger. This behavior is exactly as expected from the normalization. Naively one would expect a single peak at 1.0 for the maximum assignment probability (from the true measurements) and a single peak at 0.0 for the minimum assignment probability (the mirrored measurements). The distribution shows a small excess around 0.5 for the maximum and for the minimum value, though, which can be explained by measurements with very small drift radii. For drift radii of the order of the detector resolution the left and right solution cannot be distinguished and both solutions are used equally, resulting in a vanishing drift radius of the effective measurement. Figure 6.2 verifies this explanation; it presents the drift radius of a measurement versus its maximum probability.

In this example six iterations with the annealing schedule $T = 81 \rightarrow 9 \rightarrow 4 \rightarrow 1 \rightarrow 1 \rightarrow 1$ were used. The number of iterations could be reduced here without loss of resolution, because no noise and other disturbances exist. The reconstructed transverse momentum p_T of tracks reaches the final value as soon as the nominal temperature $T = 1$ is used (figure 6.3).

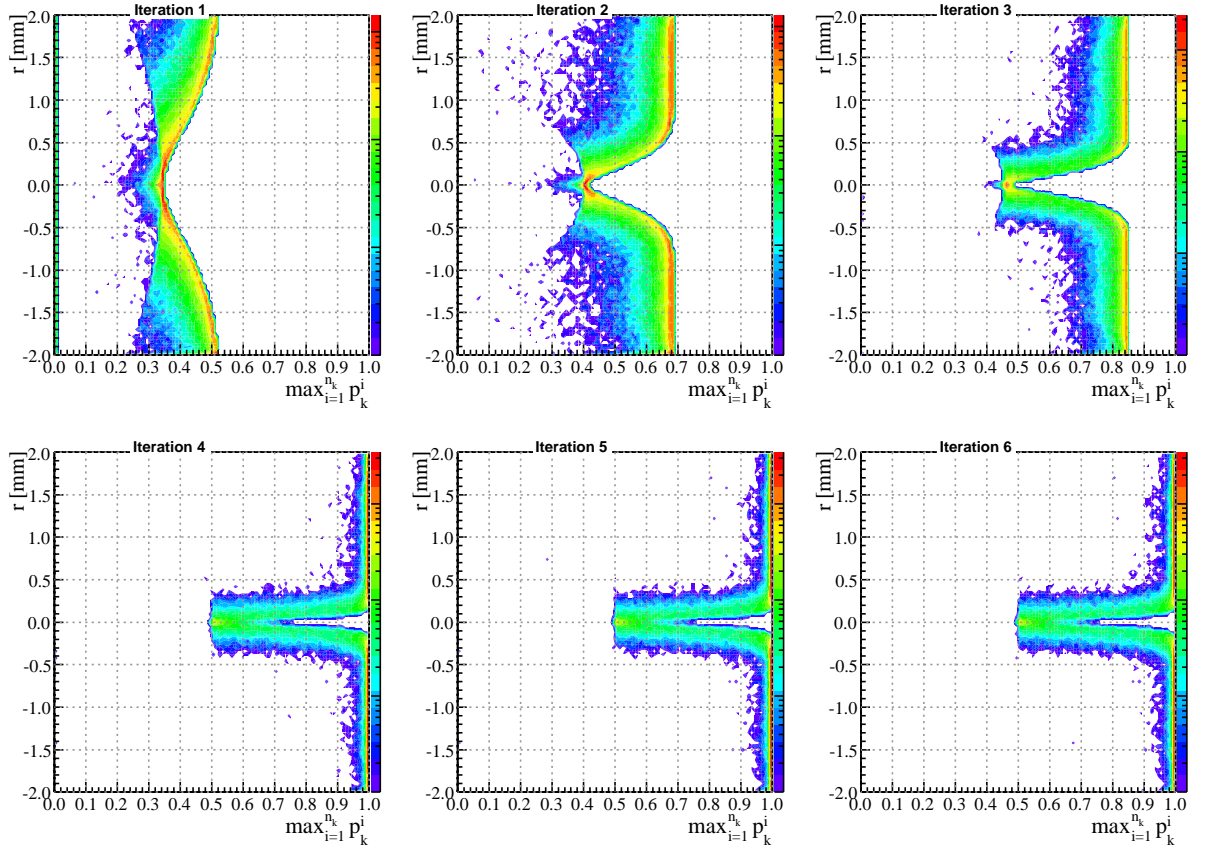


Figure 6.2: *Drift radius versus maximum assignment probability for each group of competing measurements in the TRT: The same data sample as in figure 6.1 was used. The color palette representing the number of entries in logarithmic scale is shown right of each plot.*

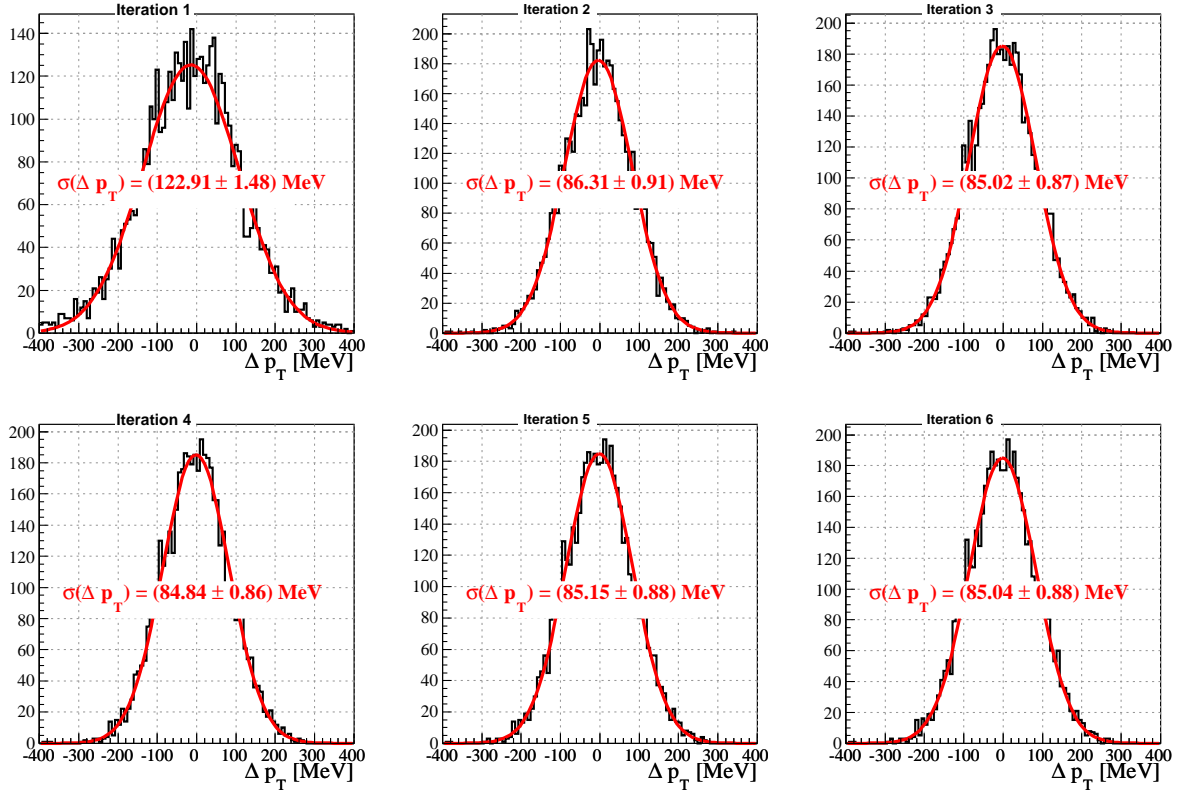


Figure 6.3: p_T resolution ($\Delta p_T = p_T^{\text{reco}} - p_T^{\text{sim}}$) for 10 GeV muon tracks in the Barrel TRT (same data sample as figure 6.2). The reconstructed p_T is improved as the temperature is lowered and TRT measurements get more and more impact on the track fit.

6.2 Performance of the TRT local pattern recognition in fatRas simulated events

As described in section 5.2 the first stage of the Inner Detector reconstruction starts with seed tracks from the Silicon layers and tries to extend them into the TRT. This is a showcase for the DAF, because a large number of ambiguities in the TRT has to be dealt with while a good estimate of track parameters exists using Silicon information only.

The studies presented in the following sections use fatRas simulated single muon events. If not mentioned explicitly a noise level of 0.200 was used, meaning in 20% of all TRT tubes a noise measurement was added and a true measurement of the simulated track was masked (i. e. removed from the collection of measurements used in pattern recognition and track fit), if it existed. Multiple scattering and energy loss were taken into account in simulation. In general 5000 events were simulated and reconstructed for each parameter value in the TRT barrel with $|\eta| < 0.5$.

6.2.1 Improvements of the implementation: Cut in straw direction for TRT measurements

After the first version of the DAF was implemented in ATHENA, the development of several improvements was guided by problems and performance decreases encountered in the validation process. An example of such a development which had a significant impact on the quality of the local pattern recognition and track fit is presented here.

TRT measurements are treated 1-dimensionally in the ATLAS offline software, using just the radius in the plane perpendicular to the TRT tube's straw and neglecting the local z -coordinate along the straw. The dimensions of the tube – length and diameter – are incorporated in its associated surface boundary. In the DAF reconstruction usual checks during extrapolation on the surface boundaries are disabled to allow for bad track predictions in the beginning, which lie in between two tubes. The calculation of assignment probabilities according to equations (4.36) and (4.37) on the other hand uses just the information perpendicular to the straw. As a result no information about the length of the measurement's tube was used in the DAF reconstruction at first. This is not a big problem for the DAF procedure, because wrong measurements are downweighted according to their drift radius, but the noise level is effectively increased, because the barrel part of the TRT is divided into two sections by splitting the straws in the middle, giving TRT measurements with positive and negative global z -coordinate, respectively.

The effect of neglecting the local z information can be seen in the left part of figure 6.4. The points show the position of noise measurements in TRT tubes where no true measurement was simulated, but which were used by the DAF with an assignment probability $\sum_i p_k^i > 0.5$. The number of fake measurements is enhanced in the

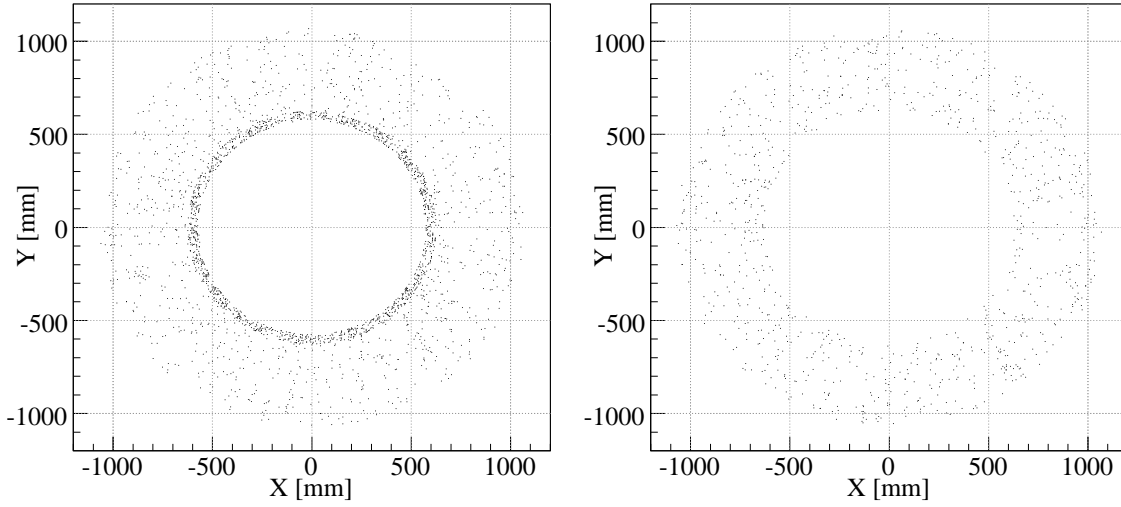


Figure 6.4: *Impact of local z -cut on positions of fake measurements in the TRT:* Radial position of fake measurements in the barrel TRT without (left) and with (right) cut on the local z -coordinate of the track prediction. The points represent noise measurements in TRT tubes where no true measurement was simulated, but which were used by the DAF with an assignment probability $\sum_i p_k^i > 0.5$. The cut especially reduces the number of fake measurements in the innermost TRT layers, where the straws are shorter and do not cover the whole barrel.

innermost TRT layers, where the straws are shorter and do not cover the whole barrel. This problem could be fixed by setting the assignment probability of both the left and right solution of a measurement to 0, if the track prediction is more than four standard deviations out of the tube's z -dimension. The right part of figure 6.4 contains the same plot using this rather simple cut. One could think of a more sophisticated solution, for example with some kind of annealing, but as the z -coordinate of the track is not directly affected by the TRT measurements itself the given solution seems to be sufficient.

6.2.2 Impact of extrapolation problems

The extrapolation of track parameters through the detector is a critical task of track reconstruction. Especially the Kalman filter technique relies on a good estimate of the error variances, because those are used in each state update (compare section 4.3.2). The extrapolation process has to take into account multiple scattering by increasing the variances and energy loss by adapting the expected track parameters and their variances. Problems and bugs in this part of the reconstruction code have a direct influence on the quality of the track fit and may even prevent a successful fit at all.

The DAF is much more sensitive to extrapolation problems than the standard methods due to the iterated filtering and smoothing in the course of the annealing. An overestimate in energy loss for example will pull the reconstructed momentum more and more away from the true value. This always has to be kept in mind when comparing the results of different track reconstruction methods. In particular in the start-up phase of the experiment, when material distributions are not perfectly known, this sensitivity may be a drawback of the DAF.

An example is given in figure 6.5. The material consideration was faulty, because the material in the SCT was counted twice during back extrapolation (i. e. outside-in extrapolation). Therefore forward filtering and backward smoothing diverged. Introducing the TRT measurements into the reconstruction made the results even worse, because the filtering process got more and more unstable. The impact of this bug is bigger for the DAF than for the standard Kalman-based algorithm.

6.2.3 Initial roadwidth of the TRT extension algorithm

Section 5.4 describes how tracks from the Pixel and SCT layers are extended into the TRT. One parameter of the basic algorithm is the initial width of the “road” on which compatible TRT measurements are searched for. If this roadwidth is chosen too small, measurements which belong to the particle’s track will not be considered and are lost for the reconstruction. A large roadwidth on the other hand is not wanted either, since the number of wrong measurements, which do not belong to the track, would be increased and may disturb the further reconstruction.

Classes of inefficiencies and fake measurements

The number of missing measurements not assigned to a track and the number of fake measurements wrongly assigned to a track provide better insights into the quality of the local pattern recognition than the track parameter residuals alone. For the TRT the local pattern recognition is complicated and likewise the definition of missing and faked measurements. In this thesis six classes of inefficiencies and fakes are defined, but other reasonable definitions may exist as well.

An *outlier* is defined as a measurement found in the neighborhood of the track candidate, but being too far away from the estimated path to be used in the track fit. Those measurements are kept on the track, because they can be hints for rapid energy loss, e. g. of electrons. As the DAF just specifies an assignment probability for each measurement the definition of outliers depends on a cut. A convenient choice would be the sum of all probabilities within a group of competing measurements on layer k : (mark `CompetingRIOsOnTrack` as outlier) $\iff \sum_i p_k^i < 0.5$. The sum is used here, because for true measurements with small drift radii the left and right solution – which have individual assignment probabilities – both get values around 0.5, but nearly sum up to 1.0 (cp. figures 6.1 and 6.2).

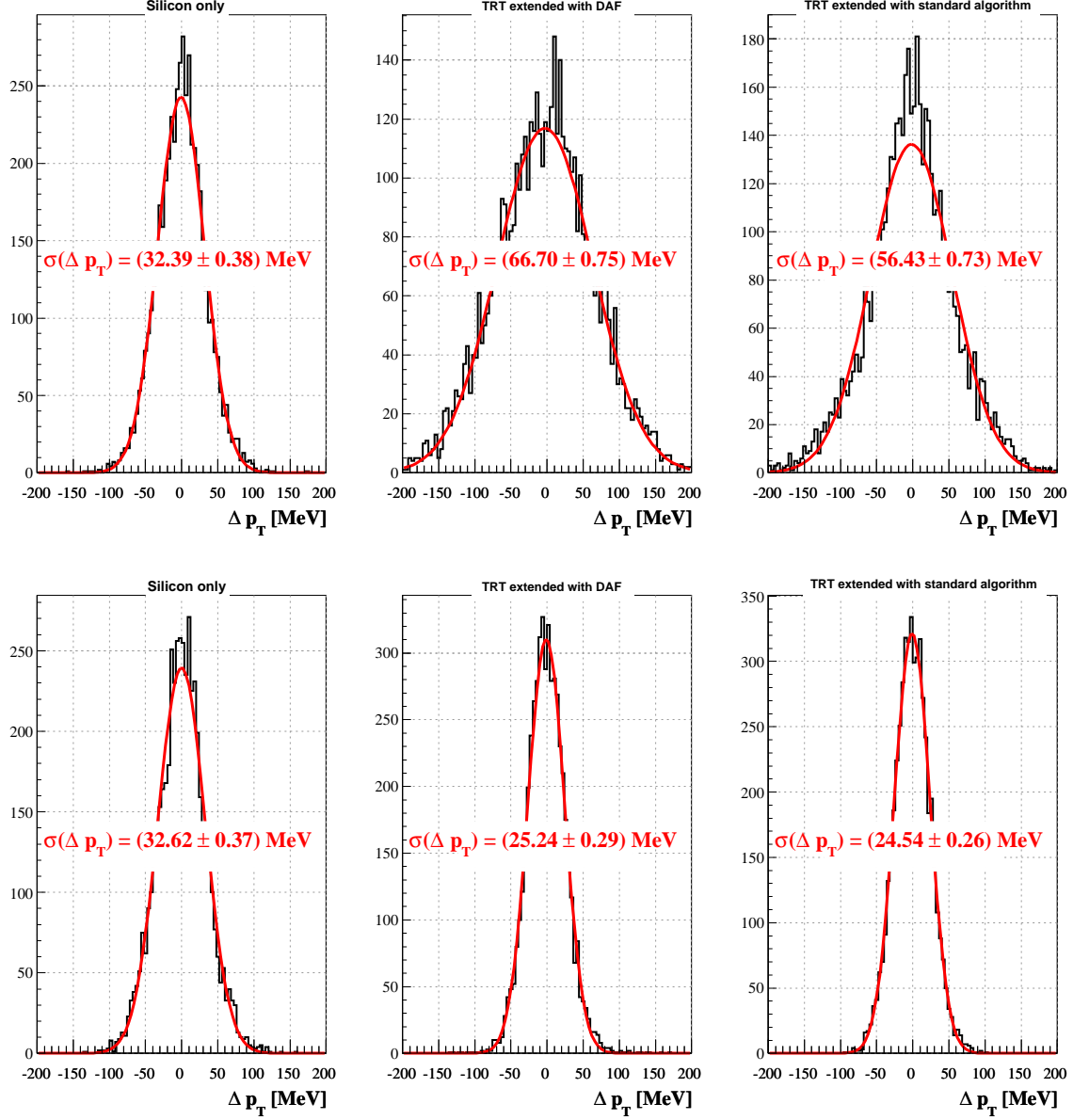


Figure 6.5: *Impact of extrapolation problems on p_T resolution:* The histograms show the p_T residuals ($\Delta p_T = p_T^{\text{reco}} - p_T^{\text{sim}}$) for 3 GeV muon tracks in the Barrel TRT. From left to right: Reconstructed p_T using Pixel and SCT measurements only, including TRT measurements using the DAF-based algorithm, including TRT measurements using the standard Kalman-based algorithm. The upper row states the results with a problem in the SCT material counting and the lower row the fixed version (DAF parameters like λ were not adjusted, therefore results are worse than shown in the following studies).

The standard TRT extension algorithm uses a special trick if TRT measurements are found in tubes which should have been hit by a track candidate, but have drift radii not compatible with the estimated path. In such a case it is assumed that the true measurement was masked by noise or another track, e. g. by δ -electrons. The drift radius information is neglected then and the error variance blown up to $\frac{\text{tube diameter}}{\sqrt{12}}$ corresponding to a flat distribution. Those measurements are called “no-drift-time” in the following. Such a concept does not exist for the DAF, but for comparison `CompetingRIOsOnTrack` were counted as “no-drift-time”, if $\frac{\max_i p_k^i}{\sum_i p_k^i} < 0.7$.

Based on this information were the six following classes of inefficiencies and fakes defined:

Missing measurements belong to tubes not contained in the reconstructed track even though the tube was hit by the true track. True measurements which are masked by noise are not counted here.

Wrong outliers exist, if a true measurement not masked by noise, was marked as an outlier.

Flipped drift sign occurs if the wrong left/right solution was taken. No-drift-time measurements are not counted here.

False No-drift-time denotes “no-drift-time” measurements in tubes without noise. This means the drift radius should have been used.

Fakes are measurements not marked as outliers, in drift tubes not hit by the true track.

Wrong drift radius is used, if a true measurement was masked by noise and the noise measurement is used in the track fit, i. e. not marked as outlier. No-drift-time measurements are ignored, because they use no drift radius at all.

Figure 6.6 shows the number of inefficiencies and fakes per track for 3 GeV single muon events with an initial roadwidth of 2 and 4 mm, respectively. The different inefficiency and fake classes are cumulative for each track and defined in the following way; for the inefficiencies:

- a. Missing
- b. Missing+Wrong outlier
- c. Missing+Wrong outlier+Flipped drift sign
- d. Missing+Wrong outlier+Flipped drift sign+False No-drift-time

and for the fake measurements:

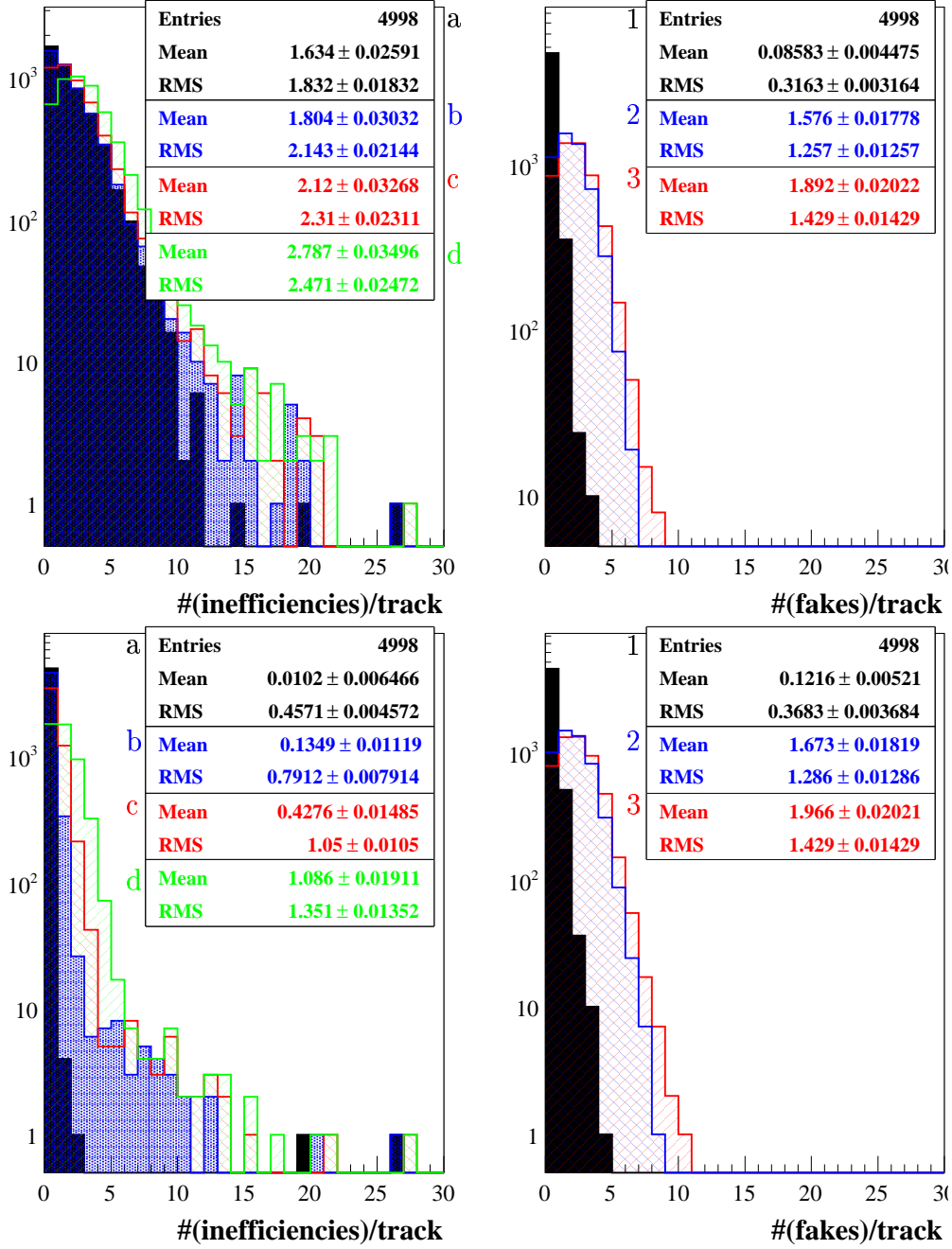


Figure 6.6: Inefficiencies and fake measurements in the TRT for 2 and 4 mm initial roadwidth, respectively: 3 GeV single muon events using the DAF with annealing scheme $T = 81 \rightarrow 9 \rightarrow 4 \rightarrow 1 \rightarrow 1 \rightarrow 1$ and $\lambda = 6.63$. The different inefficiency and fake classes are cumulative for each track: Inefficiencies: Missing (a: black), Missing+Wrong outlier (b: blue), Missing+Wrong outlier+Flipped drift sign (c: red), Missing+Wrong outlier+Flipped drift sign+False No-drift-time (d: green). Fake measurements: Fakes (1: black), Fakes+Wrong drift radius (2: blue), Fakes+Wrong drift radius+Flipped drift sign (3: red). Above: 2 mm roadwidth, below: 4 mm roadwidth.

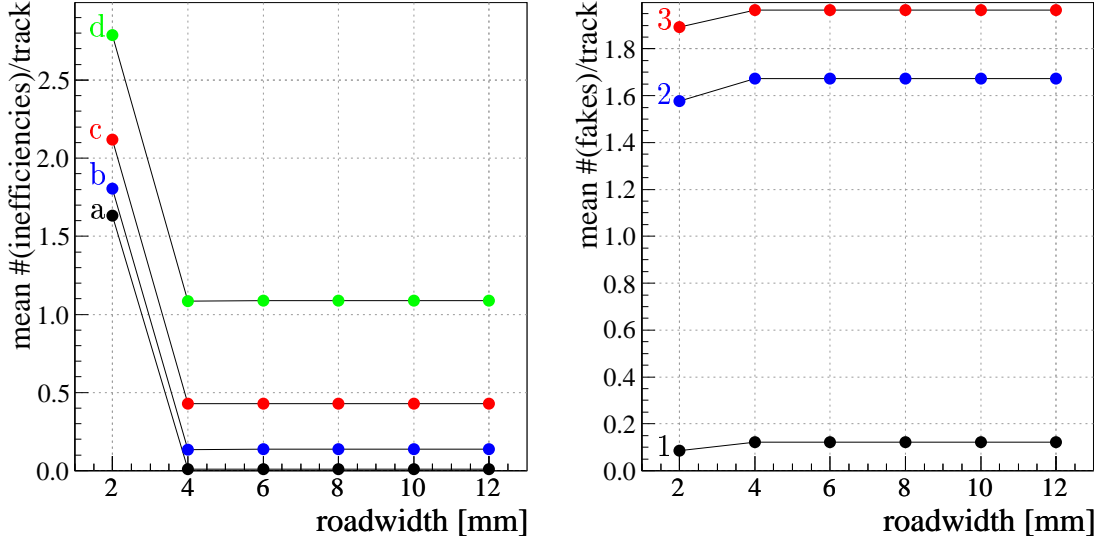


Figure 6.7: *Inefficiencies and fake measurements in the TRT vs. initial roadwidth:* The same 3 GeV single muon events are used for all data points. Mean values and other parameters correspond to the ones given in figure 6.6. The same color coding is used here.

1. Fakes
2. Fakes+Wrong drift radius
3. Fakes+Wrong drift radius+Flipped drift sign

One can see, that a roadwidth of 2 mm is not sufficient. The number of missing measurements represented by the black histogram increases rapidly for the smaller roadwidth¹. Figure 6.7 summarizes the results for roadwidths between 2 mm and 12 mm. Above a roadwidth of 4 mm no dependency can be seen anymore. Therefore an initial roadwidth of 4 mm to 6 mm seems to be sufficient. In the further studies it was chosen to use a width of 10 mm though, because no increase in the fake rates is detectable. It has to be investigated whether a larger roadwidth significantly increases the CPU-time needed.

¹The initial roadwidth is a parameter of the `TRT_TrackExtensionTool_DAF` performing the basic extension finding (see section 5.4). `CompetingRIOsOnTrack` are kept on the track if the sum of their assignment probabilities is not vanishing ($\sum_i p_k^i > 1 \cdot 10^{-20}$) and will be marked as outliers if $\sum_i p_k^i < 0.2$ (independently from the definition of outliers used in this chapter). If measurements are completely missing on the reconstructed track they are either far-off from the estimated track or were not included by the `TRT_TrackExtensionTool_DAF`. The “Missing” class is therefore the one sensitive to the initial roadwidth.

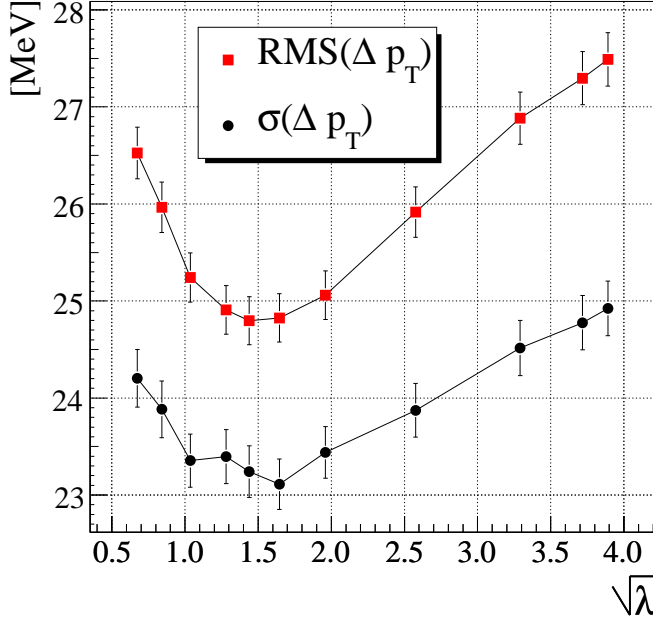


Figure 6.8: p_T resolution vs. $\sqrt{\lambda}$ for 3 GeV muon tracks: The p_T resolution is given in terms of the standard deviation σ of a Gaussian fit and the root mean square (RMS) over the whole range.

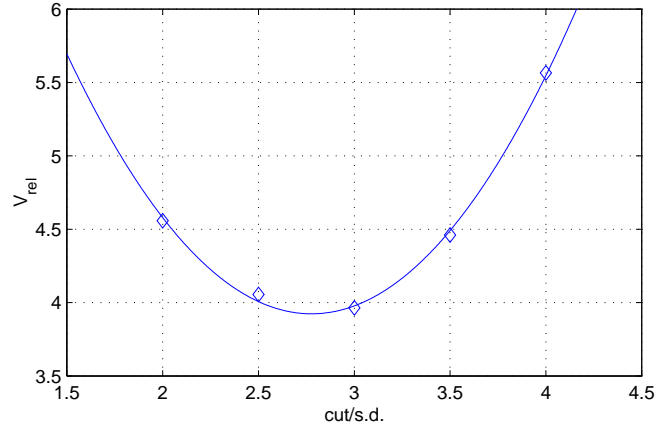
6.2.4 Intrinsic roadwidth and cut parameter λ

The normalization of assignment probabilities according to equation (4.37) with cut value (4.38) introduces a parameter λ defining the “intrinsic roadwidth” of the Deterministic Annealing Filter. At very low temperatures the parameter λ is equivalent to a χ^2 cut. The choice of λ is crucial for the reconstruction quality especially at high noise levels and therefore is investigated in detail in the following sections.

The p_T residuals $\Delta p_T = p_T^{\text{reco}} - p_T^{\text{sim}}$ were chosen as a benchmark for the reconstruction performance. The strongest impact of TRT measurements can be seen in the transverse momentum due to the large range of distances of the TRT measurements from the origin which allows one to precisely estimate the curvature of the track. The track parameters of simulated and reconstructed tracks are compared as perigee at the origin, i. e. the center of the detector near the expected collision point. The impact of the TRT measurements on the estimate of the other track parameters is smaller because of multiple scattering on the path between the reaction point and the TRT detector.

The standard deviation σ of Gaussian fits to the Δp_T distributions (cp. e. g. figure 6.3) as well as the root mean square (RMS) are used for comparison. The Gaussian fit was focused on the environment around its mean and quantifies the width of the central part of the distribution. The RMS on the other hand was calculated over

Figure 6.9: *Generalized variance vs. cut (from [FS99]):* Frühwirth and Strandlie use a relative generalized variance (comparable to a χ^2 between the true and reconstructed track parameters) to quantify the quality of the reconstruction. The given “cut” is equivalent to $\sqrt{\lambda}$ as defined in this thesis. The diagram states generalized variance vs. cut including a parabola fit.



the full range and takes mavericks into account². Those outliers are sometimes most interesting to adjust parameters of the algorithms and to find pathological cases.

The p_T resolutions determined by a Gaussian fit and by RMS are plotted against $\sqrt{\lambda}$ in figure 6.8. One observes the resolution to improve with decreasing $\sqrt{\lambda}$ down to a value around 1.5. This corresponds to stronger cuts which reduce the intrinsic road-width and the number of wrong measurements. For even smaller values the resolution gets worse again. Frühwirth and Strandlie observed a similiar behavior in their investigations of the Deterministic Annealing Filter in their simplified model. Figure 6.9 quotes results presented in [FS99]. The minimum value is shifted though, which may be explained by slight differences in the formulae and by dissimilar parameter ranges of the simulation.

All studies of inefficiencies and fakes use the definitions given on page 56, equivalent to figure 6.6. Figure 6.10 illustrates the dependency of the mean number of inefficiencies and fakes per track on $\sqrt{\lambda}$. It is clear to see how the number of wrongly assigned measurements is reduced by the stronger cut. At the same time the number of measurements being wrongly downweighted increases rapidly below $\sqrt{\lambda} \approx 2.0$ as expected.

An undesirable feature at low λ unveils figure 6.11. The diagram shows the assignment probabilities at $\lambda = 2.7055$ ($\sqrt{\lambda} = 1.6448$) corresponding to a χ^2 probability of 0.10. The maximum assignment probability within a group of competing measurements – within one `CompetingRIOsOnTrack` – is plotted for different numbers of measurements included in the group. The diagram is repeated for each of the annealing iterations $T = 81 \rightarrow 9 \rightarrow 4 \rightarrow 1 \rightarrow 1 \rightarrow 1$. More than four measurements, related to more than two drift tubes, are very seldom and therefore not easily visible in this illustration. Figure 6.12 therefore repeats the assignment probabilities after the final

²The fit is not as sensitive to statistical properties of the data sample as the RMS, but as a drawback it is more sensitive to external parameters of the analysis like the binning. For comparisons to other results the Gaussian fit seems to be the better choice, but for comparisons within the same sample of simulated events the RMS may be superior.

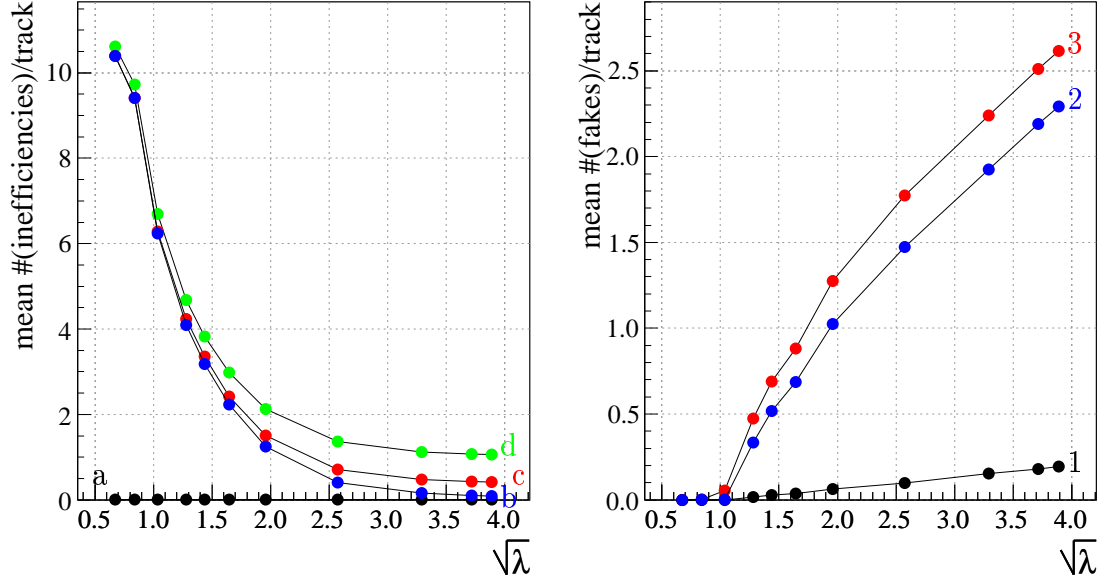


Figure 6.10: *Inefficiencies and fake measurements in the TRT vs. $\sqrt{\lambda}$:* 3 GeV single muon events using the DAF with annealing scheme $T = 81 \rightarrow 9 \rightarrow 4 \rightarrow 1 \rightarrow 1 \rightarrow 1$. The different inefficiency and fake classes (see page 56) are cumulative for each track.

iteration for two, four and six measurements per group in separate diagrams. The figure demonstrates that assignment probabilities do not follow the same distribution for the different numbers of contained measurements. The reason for this behavior is the factor n_k in front of the cut-term in the normalization, equation (4.39). This topic is discussed in detail on page 30. Based on these observations another normalization, equation (4.40), was proposed. The following section presents results using the modified normalization formula.

6.2.5 Modified normalization of assignment probabilities

The previous investigations revealed some problems at small parameter values of λ with the normalization normally used for the DAF. A modified normalization

$$p_k^{i*} = \frac{\phi_k^i}{\Lambda_k + \sum_j (\phi_k^j)} = \frac{e^{-\frac{1}{2T} \tilde{r}_{k|n}^{i\top} (\mathbf{V}_k^i)^{-1} \tilde{r}_{k|n}^i}}{e^{-\frac{\beta \cdot \lambda}{2}} + \sum_j e^{-\frac{1}{2T} \tilde{r}_{k|n}^{j\top} (\mathbf{V}_k^j)^{-1} \tilde{r}_{k|n}^j}} \quad (6.1)$$

was proposed and its effect will be studied in this section.

The distribution of assignment probabilities after the last iteration (figure 6.13) looks identical for different numbers of contained measurements after implementation

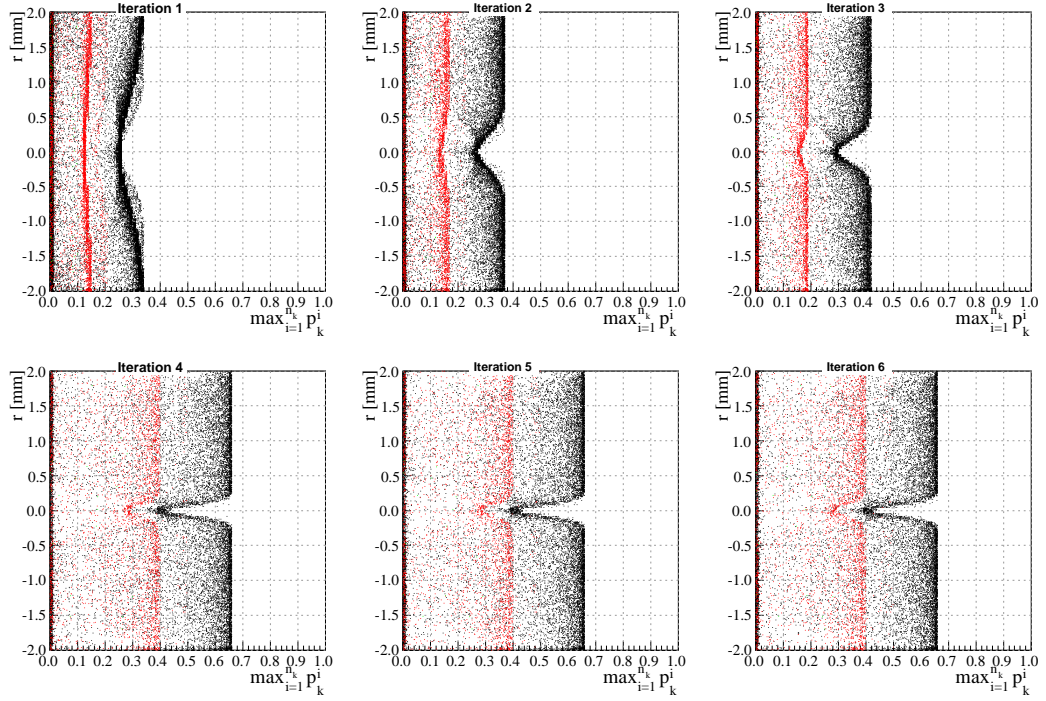


Figure 6.11: *Drift radius vs. assignment probability with $\sqrt{\lambda} = 1.6448$:* Groups with different numbers of contained measurements vary in color: One tube (2 “measurements”), black; two tubes (4 “measurements”), red; three tubes (6 “measurements”), green; four tubes (8 “measurements”), blue (more than 4 “measurements” are very seldom and therefore hard to see here, see figure 6.11 for a detailed view). The diagrams correspond to the iterations in the annealing schedule $T = 81 \rightarrow 9 \rightarrow 4 \rightarrow 1 \rightarrow 1 \rightarrow 1$.

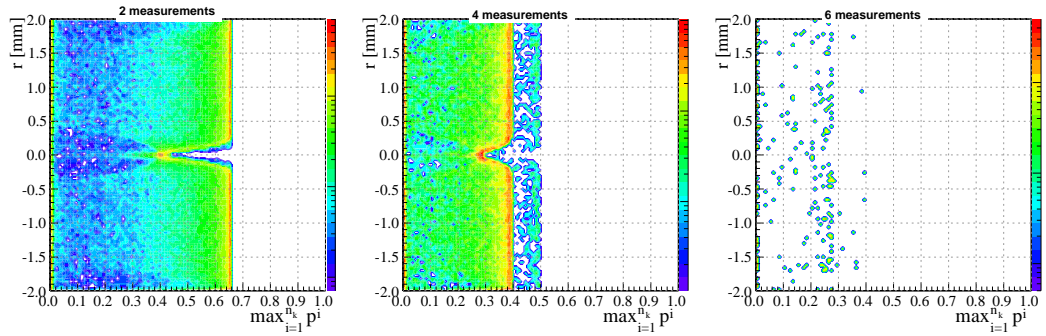


Figure 6.12: *Drift radius vs. assignment probability with $\sqrt{\lambda} = 1.6448$ after last iteration:* The probabilities shown in iteration 6 of figure 6.11 are given here (from left to right) for one tube (2 “measurements”), two tubes (4 “measurements”) and three tubes (6 “measurements”) in separate diagrams.

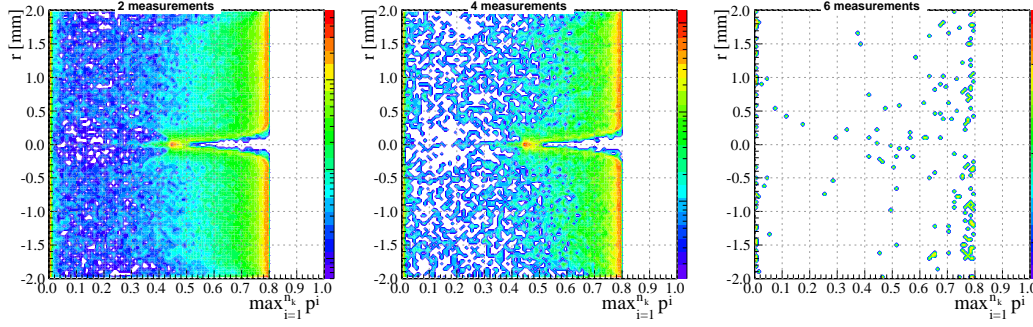


Figure 6.13: *Drift radius vs. assignment probability after last iteration with modified normalization:* Assignment probabilities at $\sqrt{\lambda} = 1.6448$ (from left to right) for one tube (2 “measurements”), two tubes (4 “measurements”) and three tubes (6 “measurements”).

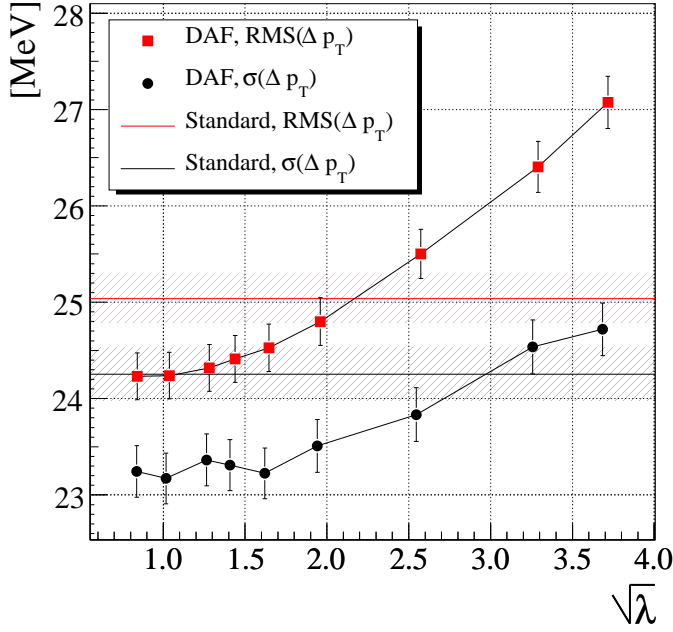


Figure 6.14: p_T resolution vs. $\sqrt{\lambda}$ for 3 GeV muon tracks with modified normalization: The p_T resolution is given in terms of the halfwidth σ of a Gaussian fit and the root mean square (RMS) over the whole range. The same values are given for the standard algorithm by the dashed lines.

of the modified normalization. Simultaneously the maximal possible value increases compared to the old normalization (cp. figure 6.12). It still does not reach 1.0, but remains smaller than about 0.8, though. This may be problematic, because the error variances of TRT measurements are therewith effectively enlarged by 25%. One can think of rescaling all probabilities by a factor $e^{-\frac{\beta \cdot \lambda}{2}} + 1$ to acquire a maximum of 1.0. Further studies in the future will show how such a rescaling affects the reconstruction. The following analyses remain with the modified normalization according to equation (6.1).

Figure 6.14 illustrates in direct comparison to figure 6.8 the dependency of the p_T resolution for 3 GeV muon tracks on the intrinsic roadwidth parameter λ . The

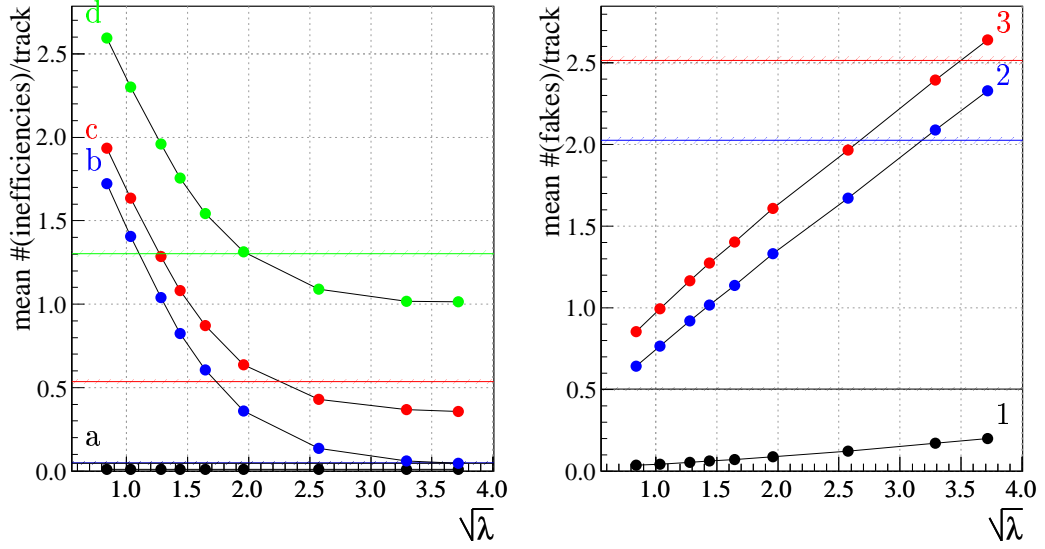


Figure 6.15: *Inefficiencies and fake measurements in the TRT vs. $\sqrt{\lambda}$ with modified normalization:* 3 GeV single muon events using the DAF with annealing scheme $T = 81 \rightarrow 9 \rightarrow 4 \rightarrow 1 \rightarrow 1 \rightarrow 1$. The different inefficiency and fake classes (see page 56) are cumulative for each track. The results of the standard algorithm on the same simulated events are given for comparison as dashed lines in identical color coding.

resolution is slightly better, but within the errors identical, for $\sqrt{\lambda} \gtrsim 2.0$. However at smaller values of $\sqrt{\lambda}$ the p_T resolution is significantly improved. No anew degradation of the resolution is observed at small λ . This means no lower limit for λ can be derived from the resolution graphs only. The diagram also contains the resolution reached by the standard algorithm on the same simulated events as dashed lines. Again the resolution is significantly improved for $\sqrt{\lambda} < 2.0$.

For a further interpretation of the results one can again investigate the number of inefficiencies and fake measurements in the TRT (figure 6.15). Both the reduction in fake measurements and the augmentation in inefficiencies with decreasing λ are less dramatic than using the usual normalization. The better resolution up to very small values of λ shows that the higher number of wrongly downweighted measurements is acceptable and less harmful than more fake measurements. Tracks through the barrel part of the Inner Detector hit approximately 34 drift tubes at mean and due to this high number of measurements there are usually not more than 10% of true measurements wrongly downweighted in a track. In general the properties of the

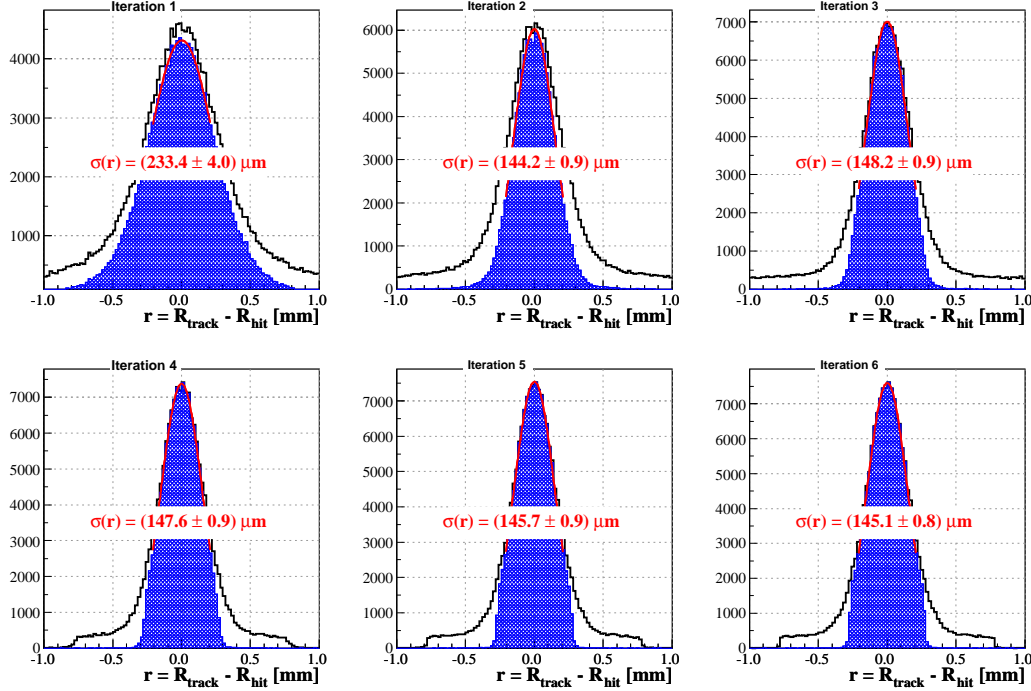


Figure 6.16: *Measurement residuals in the TRT in course of the annealing iterations:* Residuals $r = R_{\text{track}} - R_{\text{measurement}}$ of the drift radius R for 3 GeV muon tracks using the modified normalization with $\sqrt{\lambda} = 1.6448$. The histograms are related to the iterations $T = 81 \rightarrow 9 \rightarrow 4 \rightarrow 1 \rightarrow 1 \rightarrow 1$. The black line corresponds to all groups of competing measurements (using the measurement with highest assignment probability for each group), even the ones downweighted by the DAF and the shaded area to groups with $\sum_i p_k^i > 0.5$. At low temperature it is visible how groups with vanishing probability ($\sum_i p_k^i < 1 \cdot 10^{-20}$) are dropped at 0.8 mm distance. A Gaussian fit was performed just on the inner part of the distribution of measurements within the shaded area.

modified normalization seem to be better at small λ than the normal one³.

The numbers of inefficiencies and fakes are not sufficient to explain why one does not find any degradation of the p_T resolution at very small λ . Naively one would expect the resolution to get worse again, because more and more correct measurements are downweighted and the assignment probabilities in general get lower. The measurement

³The multiple structures in the distribution of assignment probabilities for the usual normalization affect the graphs of inefficiencies and fakes negatively. Figure B.1 in the appendix shows the diagrams of inefficiencies and fakes vs. $\sqrt{\lambda}$ again for two cut values of the outlier definition. The assignment probabilities can get very small for small λ and the cut defining which measurements are counted as outliers gets more and more important for the appearance of the diagram. Changing the cut from $\sum_i p_k^i < 0.5$ to $\sum_i p_k^i < 0.2$ alters the graphs completely in the old normalization (figure B.1). With the new normalization the differences are less radical even at very small $\sqrt{\lambda}$ (figure B.2), showing that the assignment is much more stable.

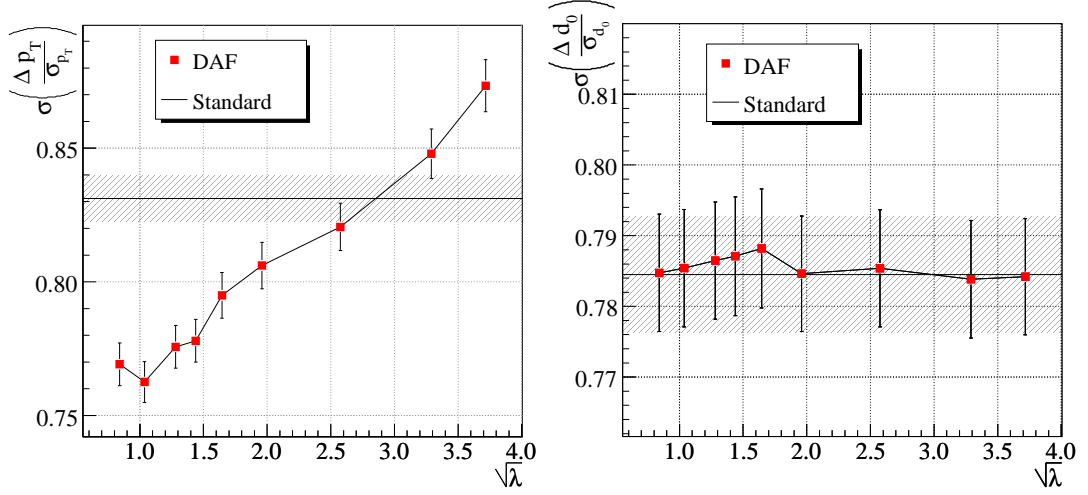


Figure 6.17: Standard deviation of p_T and d_0 pull vs. $\sqrt{\lambda}$: p_T pull (left) and d_0 pull (right) for 3 GeV muon tracks using the modified normalization. The respective values of the standard Kalman-based algorithm are given by the dashed lines for comparison.

residuals in the TRT (figure 6.16) may provide another explanation. In an optimal least squares fit and Gaussian errors of the measurements the residuals $r = R_{\text{track}} - R_{\text{measurement}}$ (where R is the drift radius in the TRT and in general $\vec{r}_{k|k} = \mathbf{H}_k \cdot \vec{x}_{k|k} - \vec{m}_k$) are Gaussian distributed with a halfwidth equal to the detector resolution (i. e. its error variance). In the simulation used for this study a detector resolution of $160\mu\text{m}$ was assumed.

It is obvious that the distribution of residuals is not Gaussian anymore for small λ , because one cuts into the tails of the Gaussian. Especially the outer parts of the distribution are far from being Gaussian. The inner part mostly keeps its Gaussian shape and a Gaussian fit to this part reveals a width being significantly below the simulated detector resolution⁴. Using such a cut can therefore result in a better momentum resolution, because the measurements with smaller deviations are weighted stronger. On the other hand one has to pay the price of destroying some of the optimal statistical properties of the estimator.

A property which is affected by very small λ is the estimate of the track parameter's variance. One criterion for the quality of the estimate is the *pull*. It is defined as the residual of a value divided by its error ($\text{pull}(q) = \frac{\Delta q}{\sigma_{\Delta q}} = \frac{q^{\text{reco}} - q^{\text{sim}}}{\sigma_q^{\text{reco}}}$ for any track

⁴The results of the fit have to be interpreted carefully, though, because even the inner part is not perfectly Gaussian and one finds χ^2/n_{dof} around 25/17 for the fit. Figure B.4 in the appendix contains the same histograms as figure 6.16 using a cut of $\sum_i p_k^i > 0.2$ instead of $\sum_i p_k^i > 0.5$ for the measurements considered by the Gaussian fit. As expected the standard deviation of the former is larger, but it is still below the detector resolution.

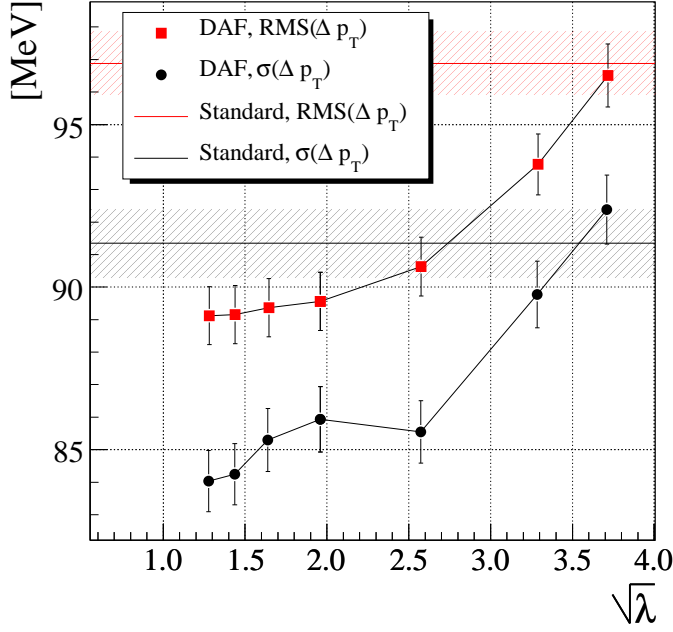


Figure 6.18: p_T resolution vs. $\sqrt{\lambda}$ for 10 GeV muon tracks with modified normalization: The p_T resolution is given in terms of the halfwidth σ of a Gaussian fit and the root mean square (RMS) over the whole range. The same values are given for the standard algorithm by the dashed lines.

parameter q). If the error variance of the track parameters is estimated perfectly, the pull of the track parameters should be distributed Gaussian around zero with a standard deviation of one. In figure 6.17 the standard deviation σ of a Gaussian fit to the pull distributions for the track parameters p_T and d_0 is plotted against $\sqrt{\lambda}$. The width of the pull deviates in both parameters strongly from the expected value of 1, i. e. the error variance of the track parameters is overestimated. No dependency on λ can be seen in the d_0 pull, whose value is in good agreement to the one determined by the standard Kalman-based algorithm used in ATHENA. The p_T pull, however, shows a strong dependency on λ and gets worse for smaller values of the intrinsic roadwidth.

From the p_T pull one can conclude that the parameter λ of intrinsic roadwidth should not be chosen too small to avoid problems due to the loss of optimal properties of the estimator. Anyhow problems with the pull of the track parameters remain both in the DAF and in the standard algorithms. These complications need further investigation to optimize the track reconstruction performance. This can be an issue of the track fit itself, but it may also be related to the extrapolation process or the simulation.

All studies were performed on 3 GeV muon tracks so far with 20% noise level in the TRT as benchmark point. The same analysis was repeated with 10 GeV tracks as comparison. In general the relative improvement compared to the standard Kalman-based algorithms is larger for 10 GeV tracks. This can be explained by multiple scattering between the origin, where the perigee track parameters are expressed at, and the innermost layer of the TRT. The effect of multiple scattering is the smaller the higher the momentum is and the impact of the TRT measurements on the perigee parameters increases likewise. Currently the DAF enhances the TRT reconstruction

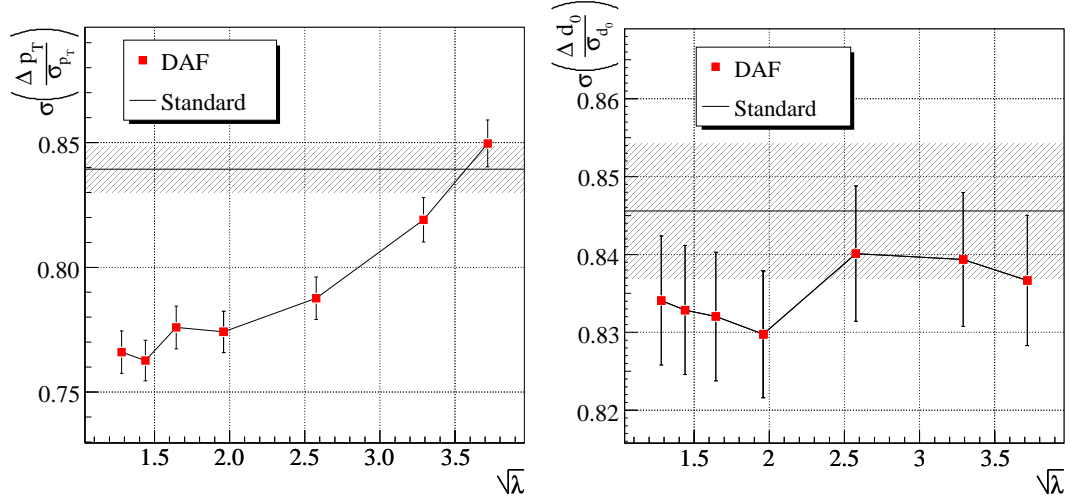


Figure 6.19: Standard deviation of p_T and d_0 pull vs. $\sqrt{\lambda}$ for 10 GeV muon tracks: p_T pull (left) and d_0 pull (right) using the modified normalization. The respective values of the standard Kalman-based algorithm are given by the dashed lines for comparison.

only and differences between the DAF and the standard algorithm are mainly due to a different handling of noise and ambiguities in the TRT. The results with 10 GeV tracks are consistent to the results with 3 GeV tracks and the p_T resolution can be improved by more than 5% (figure 6.18) compared to the standard algorithm. The error variances of the track parameters (figure 6.19) are similarly overestimated as for 3 GeV muon tracks.

6.2.6 Annealing Schedules

Annealing is an essential part of the Deterministic Annealing Filter and the so-called annealing schedule needs to be adjusted carefully. The schedule of temperatures used in the annealing iterations provides a variety of alternatives and just a selection can be presented here. The following annealing schedules have been examined:

- A. $T = 1000 \rightarrow 200 \rightarrow 81 \rightarrow 9 \rightarrow 4 \rightarrow 1 \rightarrow 1 \rightarrow 1$
- B. $T = 200 \rightarrow 81 \rightarrow 9 \rightarrow 4 \rightarrow 1 \rightarrow 1 \rightarrow 1$
- C. $T = 200 \rightarrow 81 \rightarrow 9 \rightarrow 4 \rightarrow 1 \rightarrow 0.1 \rightarrow 0.1$
- D. $T = 81 \rightarrow 9 \rightarrow 4 \rightarrow 1 \rightarrow 1 \rightarrow 1$
- E. $T = 81 \rightarrow 9 \rightarrow 1 \rightarrow 1$
- F. $T = 9 \rightarrow 1 \rightarrow 1$

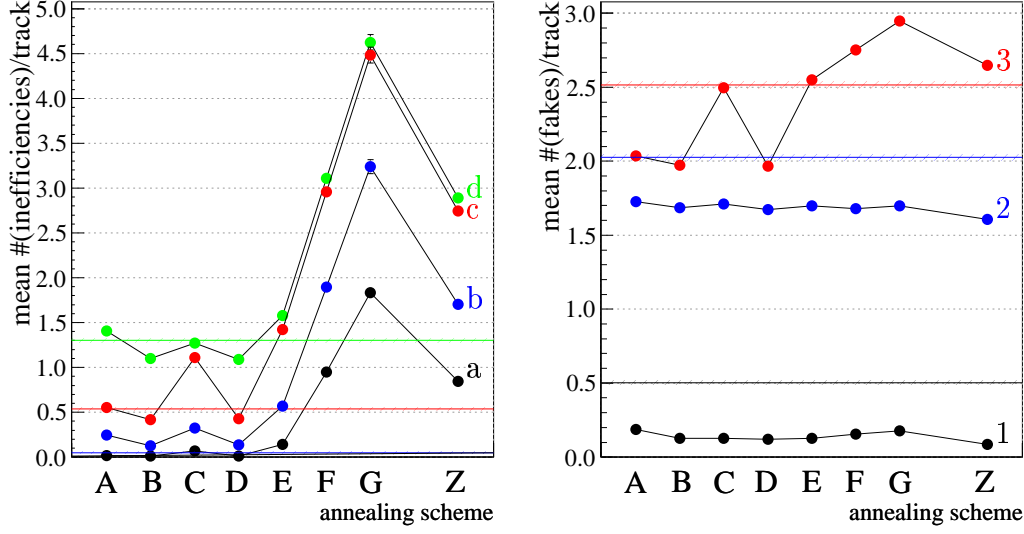


Figure 6.20: *Inefficiencies (left) and fake measurements (right) in the TRT for different annealing schemes and 3 GeV muon events:* The cumulative inefficiency and fake classes are described on page 56. The DAF was used with $\sqrt{\lambda} = 2.58$ and modified normalization; annealing schemes are described in the text.

G. $T = 1 \rightarrow 1 \rightarrow 1$

Additionally the Deterministic Annealing Filter was used in combination with the standard algorithm for pattern recognition in the TRT (using the `TRT_TrackExtensionTool_xk`). This algorithm already does the ambiguity solution in the TRT and its proposed track extensions into the TRT are usually taken as input for the standard Kalman filter (`KalmanFitter`). The sequence of `TRT_TrackExtensionTool_xk` and `KalmanFitter` is denoted as “standard algorithm” throughout the text and its results are often given for comparison. The proposed extension of the `TRT_TrackExtensionTool_xk` can also be used as input for the DAF as mentioned. In this case the DAF automatically transforms single TRT measurements into groups of two new measurements, corresponding to the left and right solution. Measurements which were already dropped from the extended track candidate can not be reintroduced in this process, but the ambiguity solution and outlier identification is redone and may yield a better result than taking the same extension candidates as input for the `KalmanFitter`. Exemplarily the DAF was run with the annealing scheme $T = 9 \rightarrow 1 \rightarrow 1$ on proposed extensions of the `TRT_TrackExtensionTool_xk`, which is indicated as Z in the diagrams.

The mentioned annealing schemes were investigated with 3 GeV and 10 GeV muon tracks with a larger intrinsic roadwidth of $\sqrt{\lambda} = 2.58$, all results therefore are slightly worse than in the previous sections. The “slow” schemes A to D do not show big

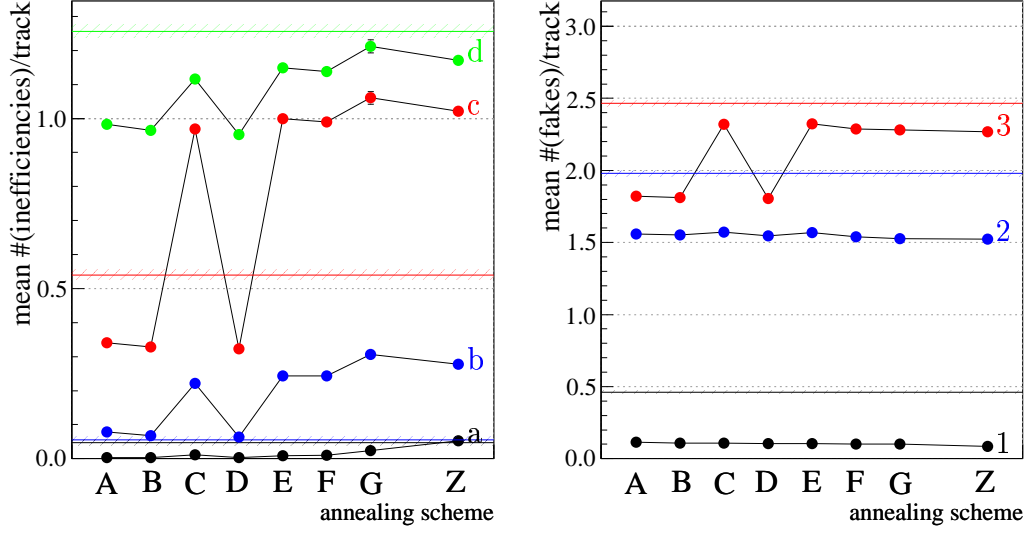


Figure 6.21: Inefficiencies (left) and fake measurements (right) in the TRT for different annealing schemes and 10 GeV muon events: The cumulative inefficiency and fake classes are described on page 56. The DAF was used with $\sqrt{\lambda} = 2.58$ and modified normalization; annealing schemes are described in the text. The same values are given for the standard algorithm by the dashed lines.

differences in their qualitative behavior between 3 GeV and 10 GeV tracks. The “fast” schemes F and G and the additional test Z have rather different behavior for 3 GeV and 10 GeV tracks, though. The number of inefficiencies and fakes are presented for 3 GeV and 10 GeV tracks in figure 6.20 and figure 6.21, respectively. The scheme B ($T = 200 \rightarrow 81 \rightarrow 9 \rightarrow 4 \rightarrow 1 \rightarrow 1 \rightarrow 1$) and scheme D ($T = 81 \rightarrow 9 \rightarrow 4 \rightarrow 1 \rightarrow 1 \rightarrow 1$) perform identically within the errors, i. e. the additional iteration of scheme B cannot improve the assignment. Too many iterations with very high temperature at the beginning may even destabilize the fit and yield worse results, as can be seen from scheme A ($T = 1000 \rightarrow 200 \rightarrow 81 \rightarrow 9 \rightarrow 4 \rightarrow 1 \rightarrow 1 \rightarrow 1$). The degradation compared to schemes B and D is even stronger in the p_T resolution (figure 6.22).

The temperature should not be lowered below the nominal value $T = 1$ to keep the smooth transition between measurements and outliers and avoid a hard cut. Scheme C ($T = 200 \rightarrow 81 \rightarrow 9 \rightarrow 4 \rightarrow 1 \rightarrow 0.1 \rightarrow 0.1$) contains a phase with very low temperature, which introduces more or less a hard cut in the end. This “deep-freezing” particularly affects the ambiguity solutions. The range around 0 mm of drift radii in which no decision is made between left and right solution (cp. figure 6.11) is getting smaller the lower the temperature is. Therefore the probability of making the wrong decision increases. Figure 6.20 and 6.21 show a strong increase in the number of inefficiencies and fakes in the red class (class c in the inefficiency plot and class 3 in the

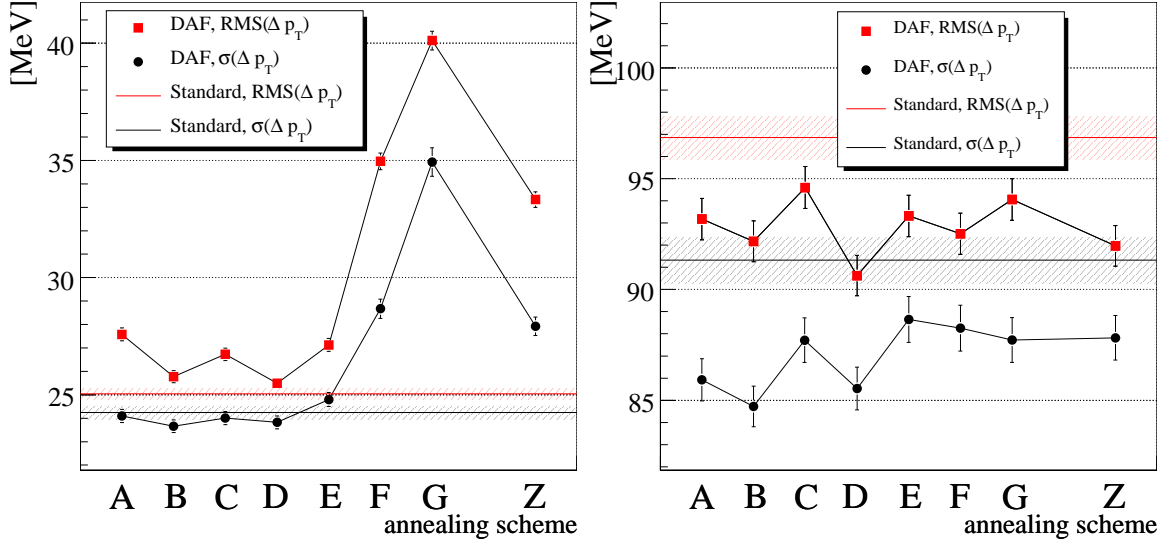


Figure 6.22: p_T resolution for different annealing schemes: The p_T resolution is given as standard deviation of a Gaussian fit and root mean square (RMS) for 3 GeV muon tracks (left) and 10 GeV muon tracks (right) using $\sqrt{\lambda} = 2.58$ and modified normalization. The used annealing schemes are described in the text.

fake plot) due to the wrong left/right solutions. But also the number of downweighted measurements (class 2, blue in the inefficiency plot) increases, because more measurements further away from the track prediction are downweighted and used sparse in the fit. The p_T resolution deteriorates accordingly.

One aims at avoiding unnecessary annealing iterations during the track fit for speed reasons. Each iteration embodies a whole track fit, so the number of iterations should be as small as possible. The momentum of the tracks is the crucial factor whether the number of iterations is sufficient or not. Schemes F ($T = 9 \rightarrow 1 \rightarrow 1$) and G ($T = 1 \rightarrow 1 \rightarrow 1$) are not sufficient for 3 GeV tracks, because the number of missing measurements increases rapidly, but can be alternatives for 10 GeV tracks. The difference between 3 GeV and 10 GeV tracks can be understood by effects of multiple scattering. The predicted path of the particle through the TRT based on the measurements in the silicon layers is much more precise for high momentum tracks, because the effect of multiple scattering is smaller. If the initial track prediction is better, less iterations with lower temperatures can be used. Bad track predictions on the other hand need higher temperatures at the beginning and therewith more iterations since far-off measurements would be immediately downweighted otherwise.

The number of wrongly downweighted ($\sum_i p_k^i < 0.5$, class b and blue in the inefficiency plot, figure 6.20) and completely dropped ($\sum_i p_k^i < 1 \cdot 10^{-20}$, class a, black) measurements is strongly enhanced for 3 GeV tracks using schemes F and G, whereas the number of fakes does not change significantly, beside an increase in the number

of wrong left/right decisions. These are clear indications that the initial track prediction is not good enough for the fast annealing. The p_T resolution degrades from approximately 24 MeV to 35 MeV at the same time.

Inefficiencies and fakes for 10 GeV tracks on the other hand have only minor differences between the faster schemes E, F and G and are comparable to the frozen scheme C. This means some more measurements are downweighted compared to the slow schemes A, B and D and the left/right decision is not as good as for those, but no big loss of quality of the measurement selection is found. The p_T dependency is likewise marginal.

Using the DAF in combination with the standard `TRT_TrackExtensionTool_xk` seems not to be helpful (see scheme Z). The results are not much better than using the same scheme (F) for extension candidates by the `TRT_TrackExtensionTool_DAF`. For 3 GeV tracks the DAF fit of the standard extension is even worse than the fit using the `KalmanFitter`. The reason is again the insufficient prediction from the silicon layers, which leads to false downweights.

Recapitulating one can draw the conclusion that the annealing scheme should be chosen according to the expected momentum of the reconstructed tracks. It might be possible to adapt the annealing scheme automatically during the fitting process to the momentum. The momentum estimate of the silicon-only part of the reconstruction may serve as a criterion here. This extension would need some changes in the implementation of the Deterministic Annealing Filter code, though. The changes have to be done extremely carefully to avoid an unpredictable behavior of the DAF, because they affect a rather critical point of the algorithm.

6.2.7 Noise Occupancy in the TRT

Pile-up events and dense jets can result in very high occupancies in the ATLAS Transition Radiation Tracker. The Deterministic Annealing Filter therefore was especially developed to cope with high occupancies and ambiguities. The studies presented in the previous sections were mostly conducted with a TRT occupancy of 20%; in this section the reconstruction performance for different occupancies of up to 70% is investigated.

A noise occupancy of $\rho_{\text{Pixel}} = 0.001\%$ in the Pixel and $\rho_{\text{SCT}} = 0.10\%$ in the SCT detector was simulated for all values of the TRT noise occupancy, besides the nominal value of $\rho_{\text{TRT}} = 1.9\%$, where $\rho_{\text{Pixel}} = 0.001\%$ and $\rho_{\text{SCT}} = 0.05\%$ was used. Additionally events were simulated without noise ($\rho_{\text{TRT}} = \rho_{\text{Pixel}} = \rho_{\text{SCT}} = 0.0\%$). Section 5.5.2 describes the noise creation in detail.

It was not possible to simulate very high noise levels in the Pixel and SCT detector, because the silicon pattern recognition produces too many track candidates. The enormous number of track candidates due to combinatorics slows down reconstruction too much. Most of the candidates cannot be extended into the TRT and are rejected, though, but they sometimes cause numerical problems which stop the reconstruction. One can conclude in either case from these problems that a specialized and adapted

6.2 Performance of the TRT local pattern recognition in fatRas simulated events

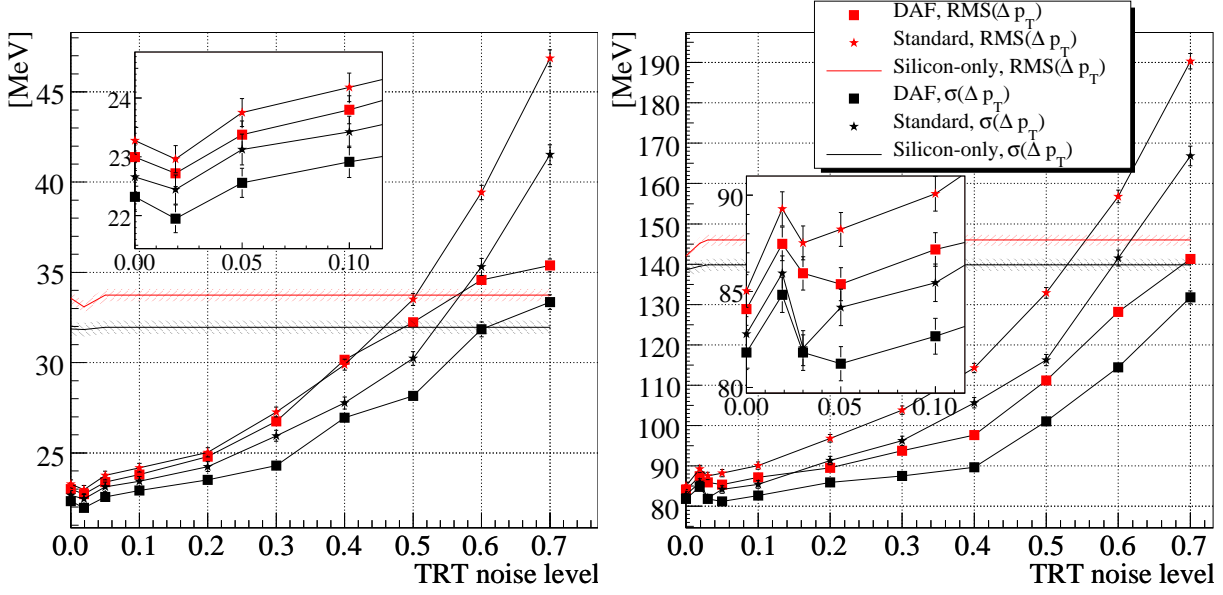


Figure 6.23: p_T resolution vs. TRT occupancy: The p_T resolution is given as standard deviation of a Gaussian fit and root mean square (RMS) for 3 GeV muon tracks (left) and 10 GeV muon tracks (right) using $\sqrt{\lambda} = 1.96$ and modified normalization. A noise occupancy of $\rho_{\text{Pixel}} = 0.001\%$ in the Pixels and $\rho_{\text{SCT}} = 0.10\%$ in the SCT was used for all values of the TRT noise occupancy, beside the nominal value of $\rho_{\text{TRT}} = 1.9\%$ where $\rho_{\text{Pixel}} = 0.001\%$ and $\rho_{\text{SCT}} = 0.05\%$ was used and the simulation without noise ($\rho_{\text{TRT}} = \rho_{\text{Pixel}} = \rho_{\text{SCT}} = 0.0\%$).

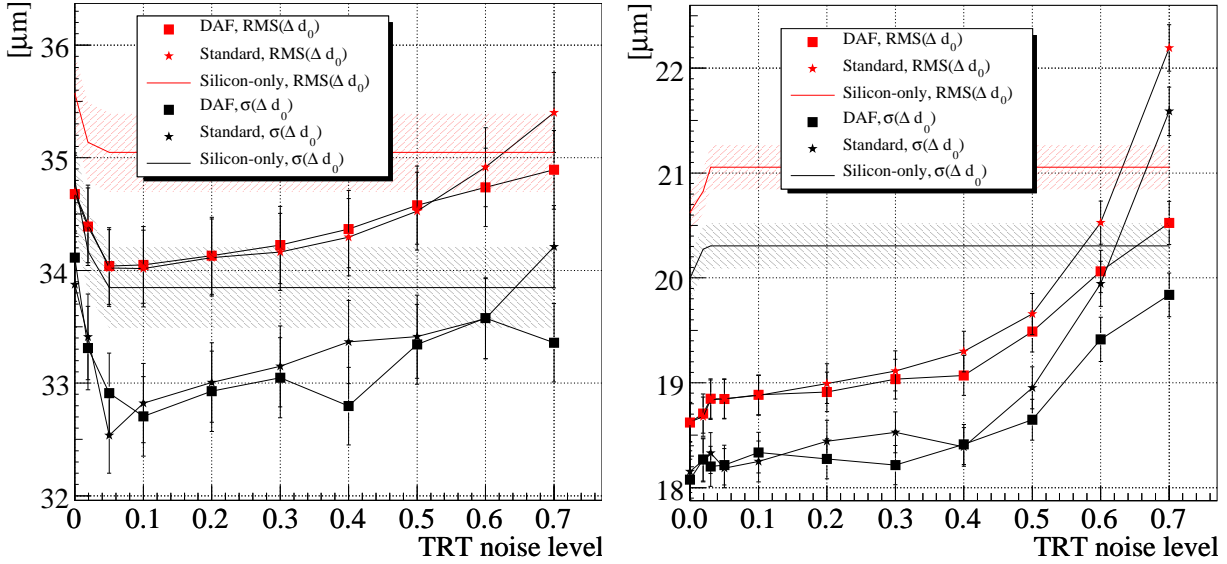


Figure 6.24: d_0 resolution vs. TRT occupancy: The d_0 resolution is given as standard deviation of a Gaussian fit and root mean square (RMS) for 3 GeV muon tracks (left) and 10 GeV muon tracks (right) using $\sqrt{\lambda} = 1.96$ and modified normalization.

silicon pattern recognition is needed for very high occupancies. A former version of the ATLAS reconstruction software started pattern recognition in the TRT as outside-in reconstruction for the same reason. Due to these problems the noise in the Pixel and SCT detector was kept at the same level.

Figure 6.23 presents the p_T resolution for 3 GeV and 10 GeV muon tracks. Resolutions are given for the DAF with annealing scheme $T = 81 \rightarrow 9 \rightarrow 4 \rightarrow 1 \rightarrow 1 \rightarrow 1$, $\sqrt{\lambda} = 1.96$ and the modified normalization and for the standard algorithm. The resolution of the silicon-only reconstruction using just the measurements in the Pixel and SCT detector is given for comparison. Again the improvement of the reconstruction due to the DAF is larger for 10 GeV tracks. In this case it is clear to see how the relative improvement grows with increasing occupancy. Even for 70% noise occupancy in the TRT – i. e. nearly three-quarter of the true measurements are replaced by noise – the p_T resolution can still be improved compared to the silicon-only reconstruction. The results of the standard algorithm are much worse than the silicon-only results at those occupancies, because outliers cannot be reliably identified anymore.

At very small occupancies the DAF can improve the standard result only slightly. This is expected, as the DAF and the standard Kalman Filter-based algorithm should be equivalent in situations without noise and mirror hits. But even without noise a very small improvement nearly within the errors is observed which may be the result of a better ambiguity solution. The results for the resolution of the transverse impact parameter d_0 are similar for the DAF and the standard algorithm. Especially for low momentum tracks the TRT measurements can improve the silicon result only slightly. This is expected, because multiple scattering smears the TRT information at the perigee. At higher momentum the estimate of the impact parameter can be improved by the TRT measurements and the DAF in general seems to perform marginally better. The results for all track parameters can be found in the appendix (figure B.5 and B.6).

6.2.8 Momentum dependency and comparison of two kind of measurement groupings in the TRT

The p_T resolution has a strong dependency on the momentum of the tracks mainly due to multiple scattering. The analytic result for the track parameter resolution can be approximated by

$$\sigma(q) = A_\sigma \oplus \frac{B_\sigma}{p_T} \quad (6.2)$$

where q is one of the track parameters $\frac{1}{p_T}$, ϕ , d_0 , $\cot \theta$ or $z_0 \sin \theta$; A_σ and B_σ are parameter specific coefficients. In general the equation $\mathbf{C} = \mathbf{A} \oplus \mathbf{B}/p_T$ holds for the covariance matrix \mathbf{C} of the track parameters in the asymptotic limits $p_T \rightarrow 0$ or $p_T \rightarrow \infty$.

The ATLAS Inner Detector Technical Design Report [ATL97a, sec. 4.5] quotes the coefficients A_σ and B_σ of the track parameters for different η ranges, based on analytical calculations. Studies presented in the TDR investigate the track reconstruction

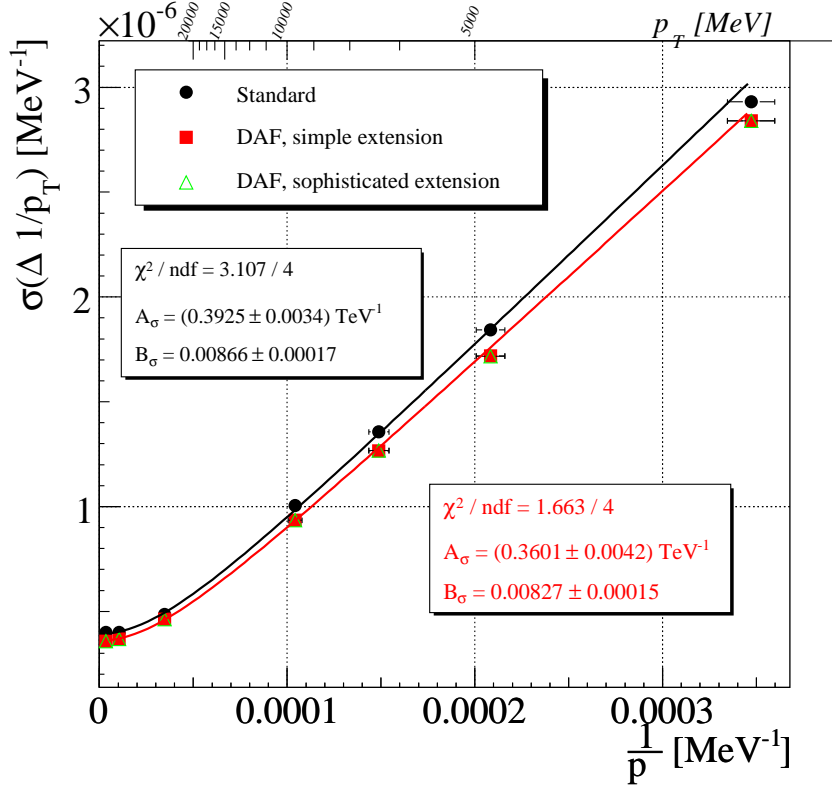


Figure 6.25: $1/p_T$ resolution vs. $1/p_T$: The $1/p_T$ resolution is determined by the standard deviation of a Gaussian fit to the track parameter residuals and is shown for the standard Kalman-based algorithm, the DAF with simple measurement grouping and sophisticated grouping, respectively. The expected p_T dependency $\sigma\left(\frac{1}{p_T}\right) = A_\sigma \oplus \frac{B_\sigma}{p_T}$ was fitted to the data points.

performance in terms of muon single track events. Single track events are chosen to get process independent results and muons are frequently used for resolution studies since they are in most cases only affected by multiple scattering and ionization losses. The TDR assumes a former detector layout, which has been slightly modified in the meantime. The results therefore are not directly comparable, but can at least serve as a guideline.

Resolutions were determined for seven values of the total momentum ($|p| = 3, 5, 7, 10, 30, 100, 300$ GeV) at 20% noise occupancy in the TRT. Due to the η range of the simulated tracks ($|\eta| < 0.5$) the mean p_T slightly deviates from these values. The simulated events were reconstructed with the standard Kalman-based algorithm and the DAF using the simple and the sophisticated grouping of TRT measurements (see section 5.4 for a description of both methods). Furthermore the annealing scheme $T = 81 \rightarrow 9 \rightarrow 4 \rightarrow 1 \rightarrow 1 \rightarrow 1$ and $\sqrt{\lambda} = 1.96$ were used here. The observed behavior of the p_T resolution follows the prediction in good agreement (figure 6.25). The following coefficients were determined by fitting $\sigma\left(\frac{1}{p_T}\right) = A_\sigma \oplus \frac{B_\sigma}{p_T}$:

	A_σ/TeV^{-1}	B_σ
Standard	0.3925 ± 0.0034	0.00866 ± 0.00017
DAF	0.3601 ± 0.0042	0.00827 ± 0.00015
TDR [ATL97a, p. 116]	0.364 - 0.365	0.0123 - 0.0127

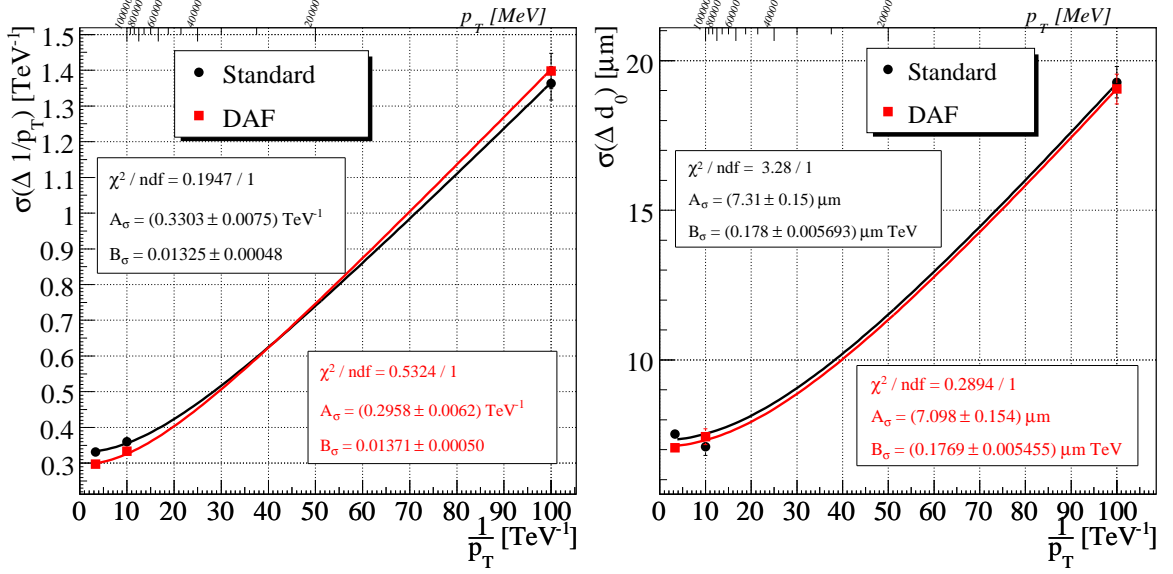


Figure 6.26: $1/p_T$ and d_0 resolution vs. $1/p_T$ for single muon events using full simulation: Resolutions are given for the DAF with annealing scheme $T = 81 \rightarrow 9 \rightarrow 4 \rightarrow 1 \rightarrow 1 \rightarrow 1$ and $\sqrt{\lambda} = 2.58$ taking only tracks with $|\eta| < 0.5$ into account. $\sigma(q) = A_\sigma \oplus \frac{B_\sigma}{p_T}$ was fitted to the points.

A_σ and B_σ of the DAF and the standard algorithm are at least in the same range as the values quoted in the TDR and show that the results are somehow consistent. The simple and the sophisticated measurement grouping produce no differences in the p_T resolution within the errors. This is expected for only slightly bent tracks in the TRT and differences will not be visible until very small transverse momenta are considered. However, DAF results are better than the results of the standard algorithm.

6.3 Performance tests with full simulation

Several reasons were mentioned for the choice of the fatRas simulation for the preceding studies. FatRas is particularly suitable for validation and performance tests of track reconstruction algorithms in ATLAS, but it cannot – and is not intended to – simulate each aspect of the tracking system’s response for a given physics event. The full Geant-based simulation on the other hand tries to be as realistic as possible and uses a much more detailed detector description. It is therefore needed to cross-check the fatRas results with results from full simulation.

Muon single track events are again the starting point of all studies. The muon events were taken from the validation sample simulated with ATHENA 11.0.4 and using geometry tag ATLAS-DC3-02 (the same reconstruction geometry as used in the

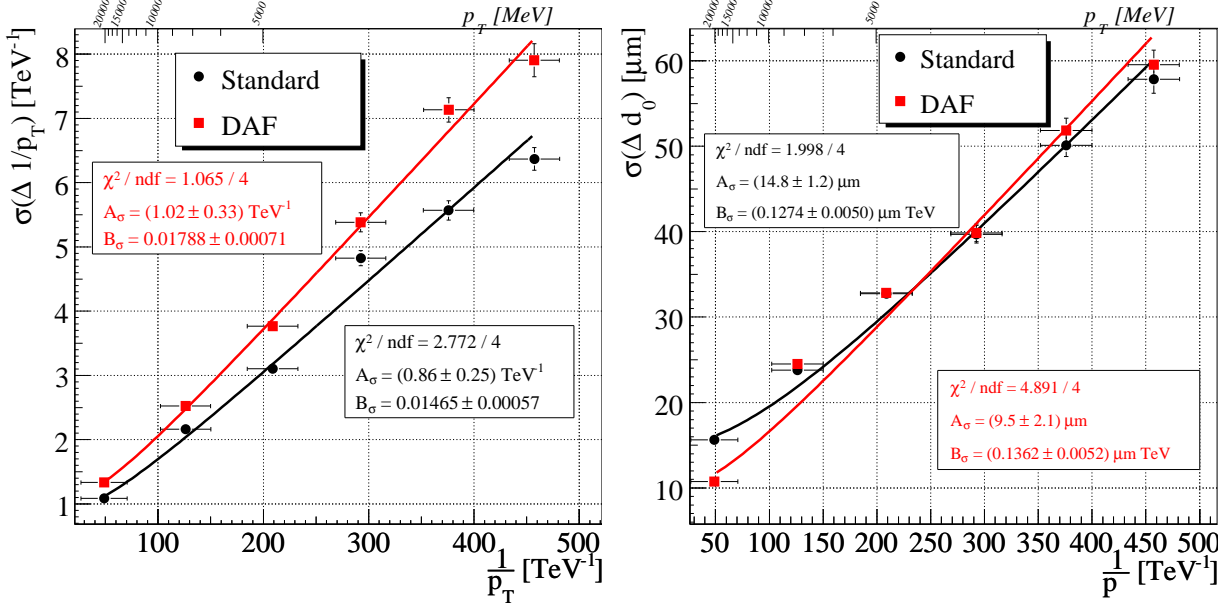


Figure 6.27: $1/p_T$ and d_0 resolution vs. $1/p_T$ for inclusive top events using full simulation: Resolutions are given for the DAF with annealing scheme $T = 200 \rightarrow 81 \rightarrow 9 \rightarrow 4 \rightarrow 1 \rightarrow 1 \rightarrow 1$ and $\sqrt{\lambda} = 2.58$ taking only tracks with $|\eta| < 0.8$ into account. $\sigma(q) = A_\sigma \oplus \frac{B_\sigma}{p_T}$ was fitted to the points.

fatRas studies). Unfortunately just muon events with $p_T = 10, 100, 300$ GeV could be used. From the 10000 events in each of the samples only about 1100 tracks are within the considered η range of $|\eta| < 0.5$; the statistical significance is therefore much smaller than in the fatRas studies where always 5000 tracks within this range were simulated for each parameter value. The events were reconstructed with the DAF using the annealing schemes $T = 200 \rightarrow 81 \rightarrow 9 \rightarrow 4 \rightarrow 1 \rightarrow 1 \rightarrow 1$ and $T = 81 \rightarrow 9 \rightarrow 4 \rightarrow 1 \rightarrow 1 \rightarrow 1$ with $\sqrt{\lambda} = 2.58$ and $\sqrt{\lambda} = 3.29$. The differences in the track parameter resolutions between these four parameter combinations lie within the errors and therefore only the results of one parameter set are presented.

Figure 6.26 contains the p_T and d_0 resolutions using the DAF with $T = 81 \rightarrow 9 \rightarrow 4 \rightarrow 1 \rightarrow 1 \rightarrow 1$ and $\sqrt{\lambda} = 2.58$ and the results of the standard algorithm. The DAF performs slightly better here and the following coefficients A_σ and B_σ were determined by a fit to the data points:

	$A_\sigma(1/p_T)/\text{TeV}^{-1}$	$B_\sigma(1/p_T)$	$A_\sigma(d_0)/\mu\text{m}$	$B_\sigma(d_0)/\mu\text{m TeV}$
Standard	0.3303 ± 0.0075	0.01325 ± 0.00048	7.31 ± 0.15	0.1779 ± 0.0067
DAF	0.2958 ± 0.0062	0.01371 ± 0.00050	7.10 ± 0.15	0.1769 ± 0.0055
TDR	0.364 - 0.365	0.0123 - 0.0127	10.9	0.0572 - 0.0590

The coefficients are comparable to the values given in the TDR, beside $B_\sigma(d_0)$ which is much bigger than the TDR value. A direct comparison to the values of the fatRas

simulation shows that the resolution is a little better for 100 and 300 GeV tracks, but nearly 40% worse for the 10 GeV tracks which can be seen in the plots. Simulated events do not contain pile-up, but only the nominal noise, which may be the reason for the high- p_T results. The relative improvement of the DAF compared to the standard algorithm is similar to fatRas simulated events for 100 and 300 GeV tracks. The discrepancy at 10 GeV on the other hand cannot be easily explained, but one should keep in mind that statistics are much inferior to the fatRas simulation.

As a first study with realistic physics events a data sample of inclusive top events was chosen. The events belong to the validation sample simulated with ATHENA 12.0.2 and geometry tag **ATLAS-DC3-07**. The studies suffer again from low statistics especially for very high momentum tracks. Results deviate rather strongly from previous results and especially the DAF performance is degraded (figure 6.27). The reason for this behavior could not be identified yet. The fact that DAF and standard algorithm are both affected may serve as a hint for problems in the general setup of the reconstruction using this detector geometry version. The plots shown here include even tracks where the extension into the TRT failed. In this case the track fit includes silicon measurements only yielding worse momentum resolutions. The extension may fail in about 10 - 15% of the tracks for $t\bar{t}$ -events for various reasons. It is possible that no road in the TRT was found at all, the fit using TRT measurements was worse than the one without TRT or the fit itself failed. The extension processing which decides whether the proposed extension is accepted, is a critical point and may need adjustments to the DAF behavior. A detailed investigation of each reconstruction step on individual tracks will certainly provide hints how to solve the problem.

Further investigations using full simulation are needed in any case and the ones presented here have to be seen as a starting point. The analyses of the track reconstruction performance have to split up the whole $t\bar{t}$ - or other physics events to study electron tracks, dense jets or different η ranges separately. The parameters of the DAF, like the intrinsic roadwidth λ and the annealing scheme, have to be adjusted for each sub-sample to find a general setup in the end yielding the best reconstruction performance.

7 Conclusion and Outlook

The Deterministic Annealing Filter (DAF) was implemented as an alternative track fitting method in the ATLAS offline reconstruction software including a matched global pattern recognition in the Transition Radiation Tracker (TRT). Belonging to the class of adaptive track fitters the DAF performs local pattern recognition for noise suppression and ambiguity solution directly within the track fit. Several software tools for the validation of the track reconstruction have been developed additionally.

The ATLAS fast track simulation (fatRas) was employed as a testbed for the DAF to acquire a clean and controllable environment where simulation parameters can easily be changed. The fatRas studies suggested a small modification of the DAF formulae, more precisely the normalization of assignment probabilities. Improvements were made in the outlier handling and various parameters of the DAF could be adjusted to yield the best resolutions of the estimated track parameters. Results are very promising especially for high occupancies in the TRT, but even without additional noise the track reconstruction performance of the DAF is superior to the standard algorithm due to better solutions of the ambiguities of the TRT measurements. Especially the momentum resolution of the track fit could be improved. The optimal choice of the annealing scheme, i. e. a small number of iterations at high track parameter resolution, is found to be dependent on the transverse momentum of the tracks. A self-acting adaptation of the annealing scheme according to the first estimate of the track momentum as an enhancement of the current implementation is suggested.

Complementary to the fatRas studies events generated by the full ATLAS simulation have been investigated. First analysis of single muon events confirm the results of the fatRas studies, but tests using top quark events are controversial and need further investigation. The adjustment of the DAF parameters has to be re-done using full simulation on restricted event shapes, for example electron tracks or dense jets. Afterwards physics events including pile-up can be used as benchmarks for studies of the reconstruction performance.

Up to now studies were concentrated on the extension of tracks from the layers of the silicon detectors into the TRT, because its ambiguities make the TRT a showcase application of the DAF. But the DAF may also be advantageous for second stage pattern recognition in the TRT, when searching for tracks with less or without measurements in the silicon detectors, e. g. from conversions. Furthermore local pattern recognition in the Pixel and SCT layers may also profit from the DAF and should be studied in the future. The Multi-Track Fitter (MTF) as an extension of the DAF may be valuable

for very dense jets with nearby or overlapping tracks. A future implementation of the MTF will be able to use many components of the current implementation of the DAF.

A Details on the track reconstruction algorithms

A.1 Kalman filter in gain matrix formalism

The update step of the Kalman Filter can be rewritten in the Kalman gain matrix formalism, replacing equations (4.17) and (4.18) on page 21. The predicted state is then *updated* with the measurement from layer k using the residual between the expected measurement and the true measurement on layer k – the so-called *innovations* – which are weighted by the *Kalman gain matrix* \mathbf{K}_k

$$\mathbf{K}_k = \mathbf{C}_{k|k-1} \mathbf{H}_k^\top (\mathbf{H}_k \mathbf{C}_{k|k-1} \mathbf{H}_k^\top + \mathbf{V}_k)^{-1} \quad (\text{A.1})$$

giving the *updated state*

$$\vec{x}_{k|k} = \vec{x}_{k|k-1} + \mathbf{K}_k \cdot (\vec{m}_k - \mathbf{H}_k \cdot \vec{x}_{k|k-1}) \quad (\text{A.2})$$

with the covariance $\mathbf{C}_{k|k}$ of the updated state

$$\mathbf{C}_{k|k} = (\mathbf{1} - \mathbf{K}_k \mathbf{H}_k) \mathbf{C}_{k|k-1} \quad (\text{A.3})$$

A.2 Properties of assignment probabilities

This appendix illustrates some properties of the assignment probabilities used by the Deterministic Annealing Filter. The dependency of the assignment probabilities on the pull between estimated track position and measurement is shown. The pull is defined as $\text{pull}(x) = \frac{x^{\text{track}} - x^{\text{measurement}}}{\sqrt{(\sigma_x^{\text{track}})^2 + (\sigma_x^{\text{measurement}})^2}}$.

Figure A.1: *Assignment probability for a single measurement:* The plot shows the assignment probability for a single, 1-dimensional measurement (i. e. no competition between hits) vs. the pull for different temperatures T . λ was chosen to be 10.8275 ($\sqrt{\lambda} = 3.29$), which corresponds to a cut-off probability of 0.0010

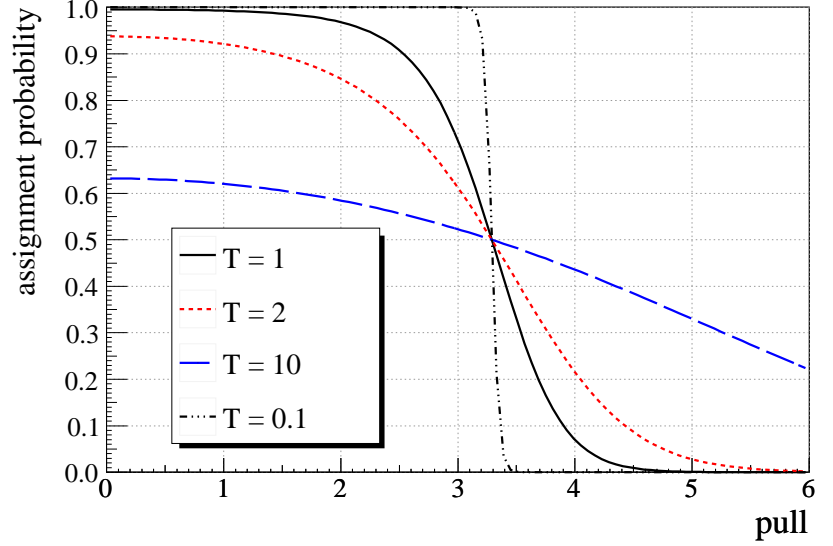
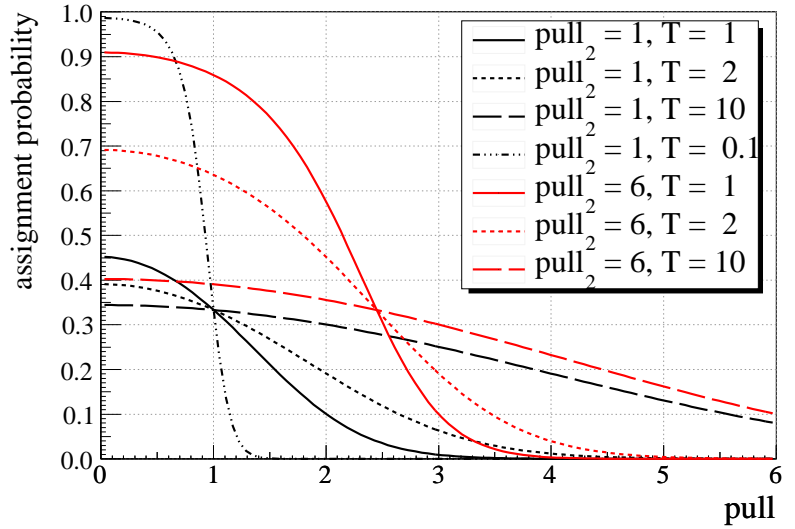


Figure A.2: *Assignment probability for one of two measurements:* The plot shows the assignment probability for a 1-dimensional measurement in presence of another competing one vs. the pull for different temperatures T and two pulls of the second measurement. λ was chosen to be 10.8275.



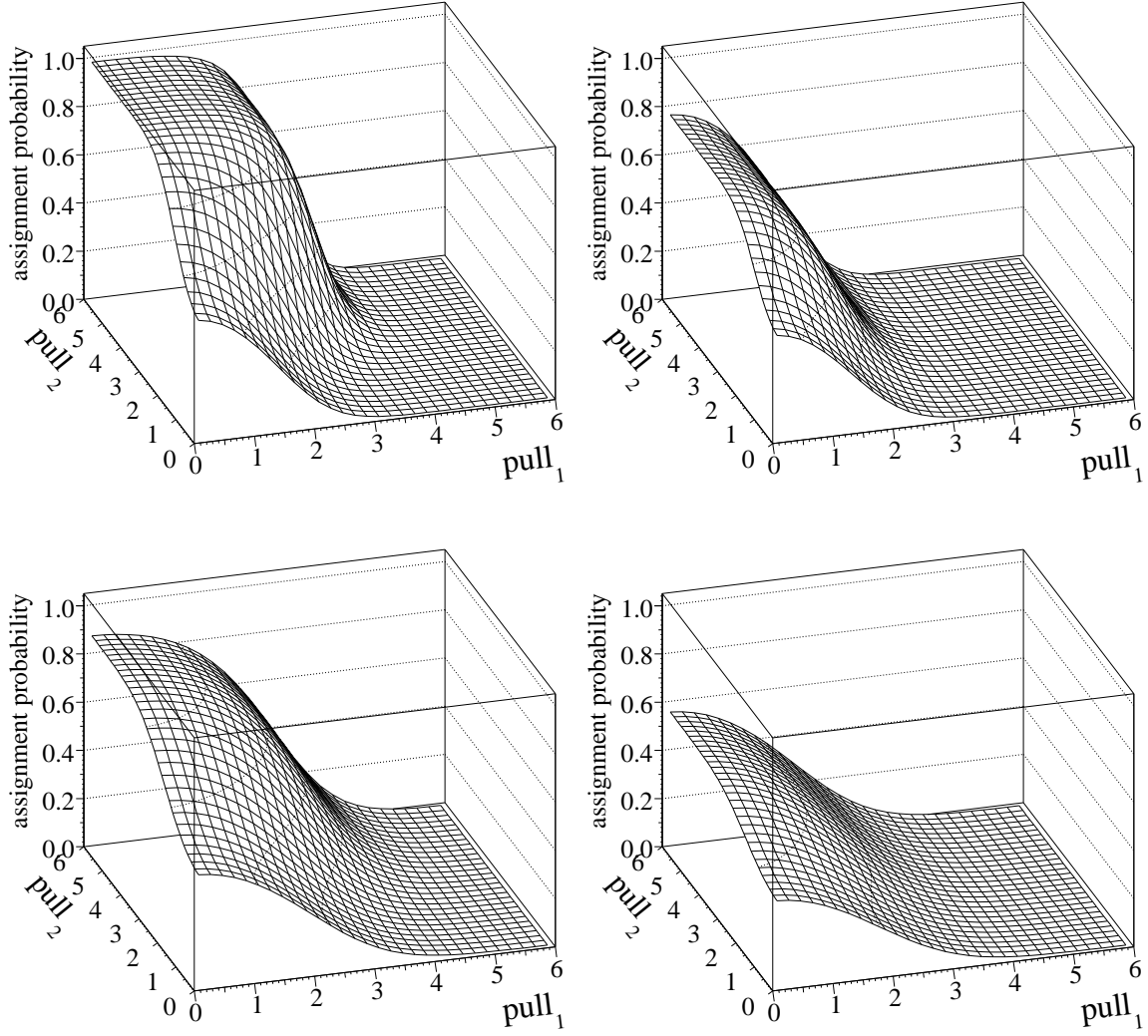


Figure A.3: Assignment probability for one of two measurements vs. pull of both measurements: Above: $T = 1$, below: $T = 2$; left: $\lambda = 10.8275$, right: $\lambda = 3.8414$.

B Supplements to the DAF studies

B.1 List of extra packages used in the studies and reconstruction parameters

All studies were performed with ATHENA release 12.0.2 using some additional package versions:

- InDetCompetingRIOsOnTrackTool-00-00-08
- InDetMC_SimAlgs-00-00-23
- TrkDetDescrSvc-00-02-03 (for fatRas studies only)
- TrkDeterministicAnnealingFilter-00-00-13
- TrkCompetingRIOsOnTrackTool-00-00-05
- TrkMeasurementUpdater-00-00-29
- TrkValTools-00-00-30

The fatRas studies used the version ATLAS-DC3-02 of the ATLAS detector geometry and restricted the track simulation to the barrel part of the Inner Detector by demanding $|\eta| < 0.5$ for the perigee parameters of the simulated tracks.

Full simulation data samples used in the studies:

single muon events simulated with ATHENA 11.0.4 and using geometry tag ATLAS-DC3-02¹.

inclusive top events MC@NLO generator simulated with ATHENA 12.0.2 and using geometry tag ATLAS-DC3-07².

B.2 Additional figures

The following figures extend the studies presented in chapter 6.

¹From /castor/cern.ch/atlas/csc/valiproduct/sampleA/mc11/004934.mu_pt100/digit/v11000401/.

²From /castor/cern.ch/grid/atlas/caf/testIdeal_07/testIdeal_07.005200.T1_McAtNlo_Jimmy.digit.RD0.v12000201_tid002760/.

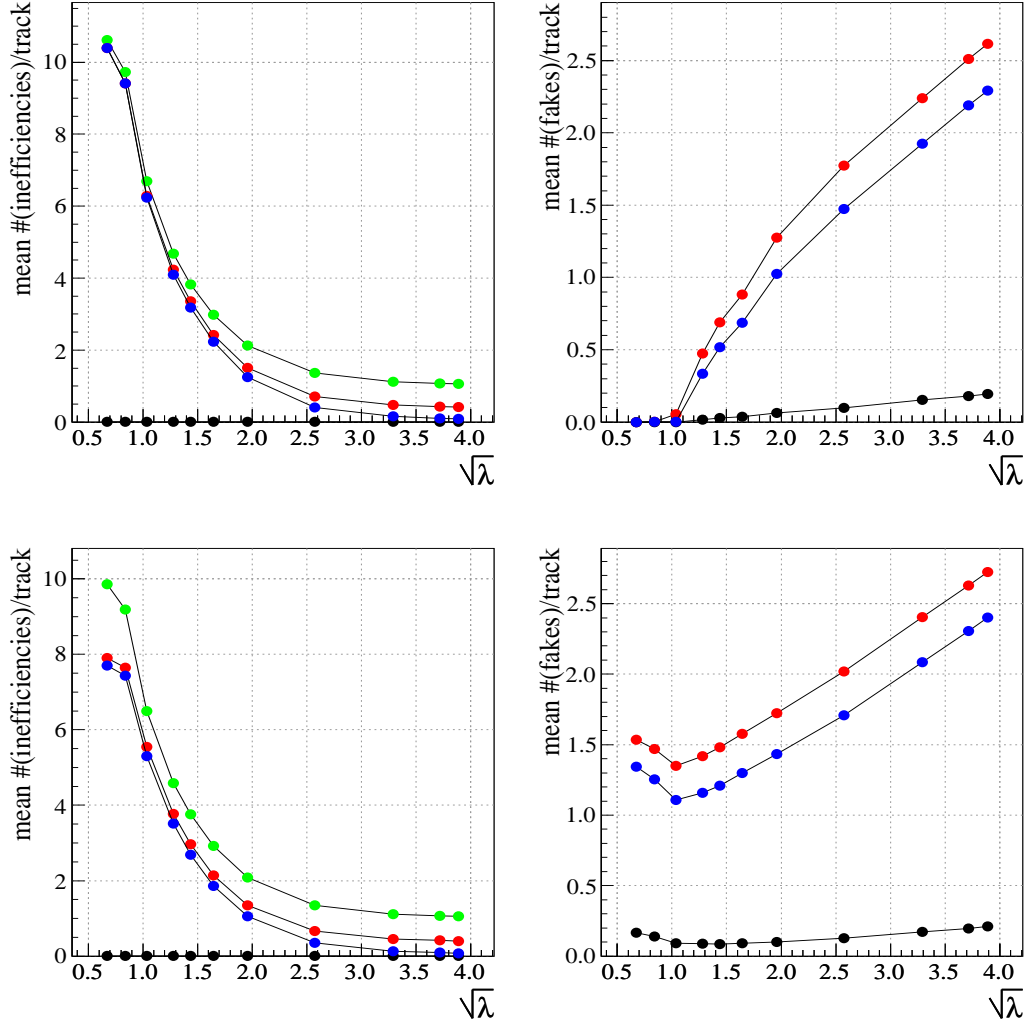


Figure B.1: *Inefficiencies and fake measurements in the TRT vs. $\sqrt{\lambda}$ with different outlier cuts: 3 GeV single muon events using the DAF with annealing scheme $T = 81 \rightarrow 9 \rightarrow 4 \rightarrow 1 \rightarrow 1 \rightarrow 1$. The different inefficiency and fake classes (see page 56) are cumulative for each track. In the diagrams above an outlier cut of $\sum_i p_k^i < 0.5$ was used and in the diagrams below a cut of $\sum_i p_k^i < 0.2$.*

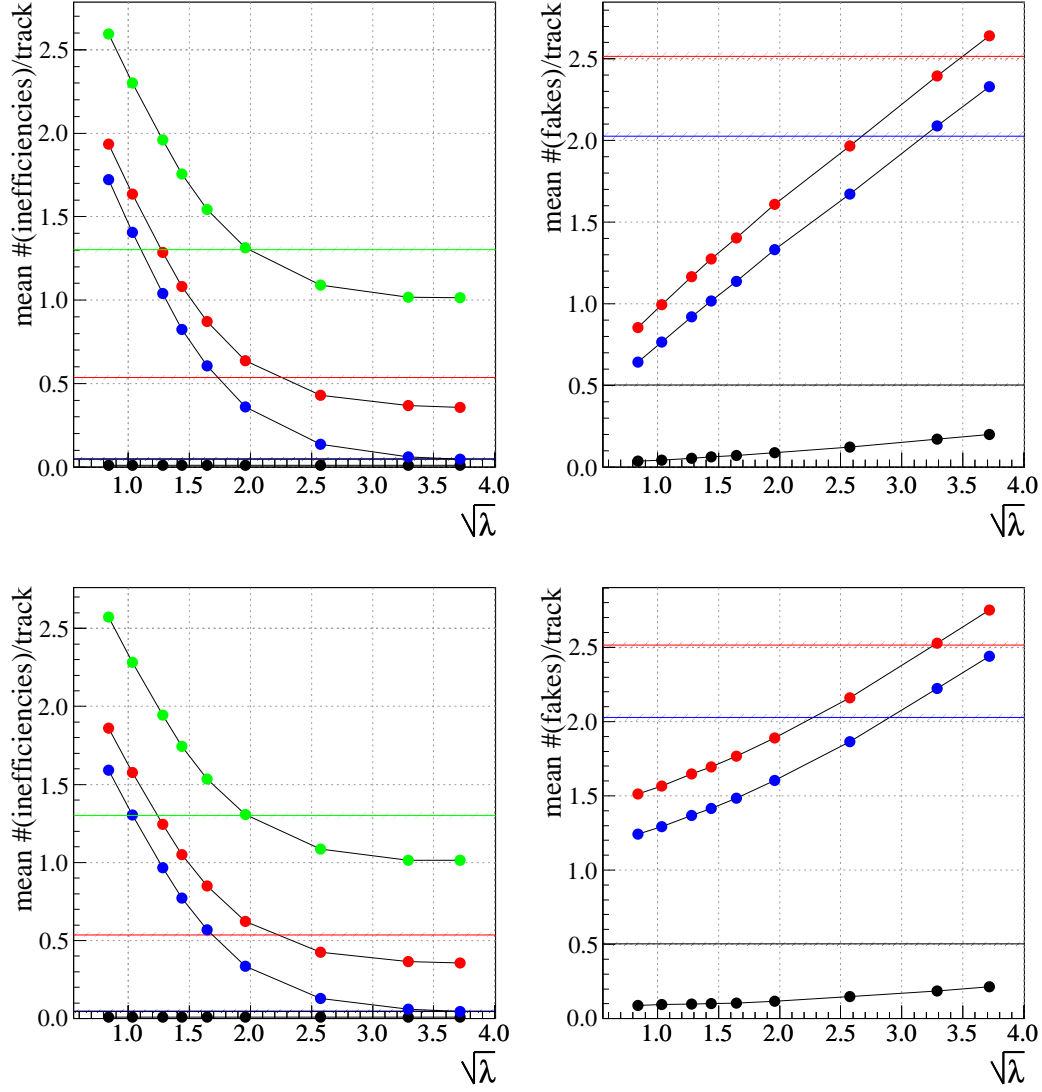


Figure B.2: *Inefficiencies and fake measurements in the TRT vs. $\sqrt{\lambda}$ with different outlier cuts using the modified normalization: 3 GeV single muon events using the DAF with annealing scheme $T = 81 \rightarrow 9 \rightarrow 4 \rightarrow 1 \rightarrow 1 \rightarrow 1$. The different inefficiency and fake classes (see page 56) are cumulative for each track. In the diagrams above an outlier cut of $\sum_i p_k^i < 0.5$ was used and in the diagrams below a cut of $\sum_i p_k^i < 0.2$.*

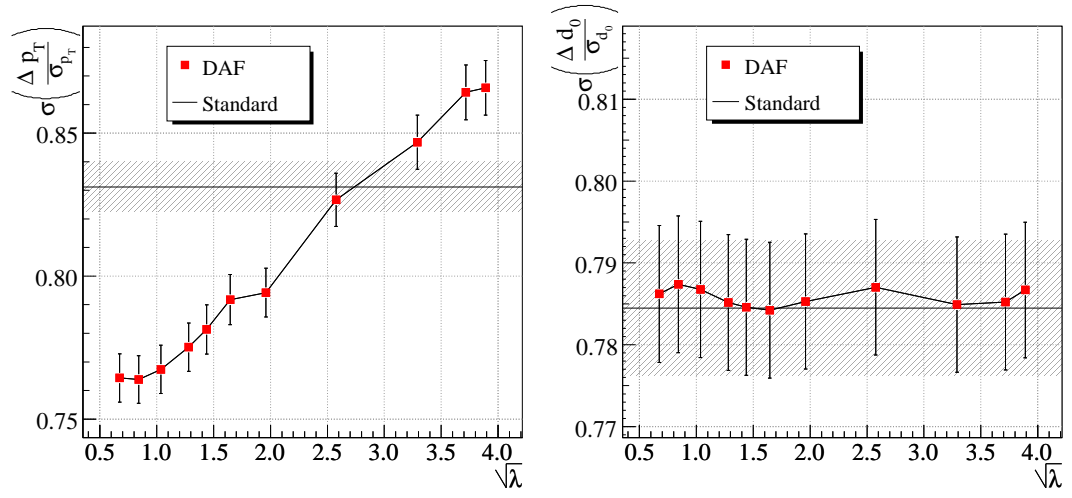


Figure B.3: Standard deviation of p_T and d_0 pull vs. $\sqrt{\lambda}$ using standard normalization of assignment probabilities: p_T pull (left) and d_0 pull (right) for 3 GeV muon tracks. The respective values of the standard Kalman-based algorithm are given by the dashed lines for comparison.

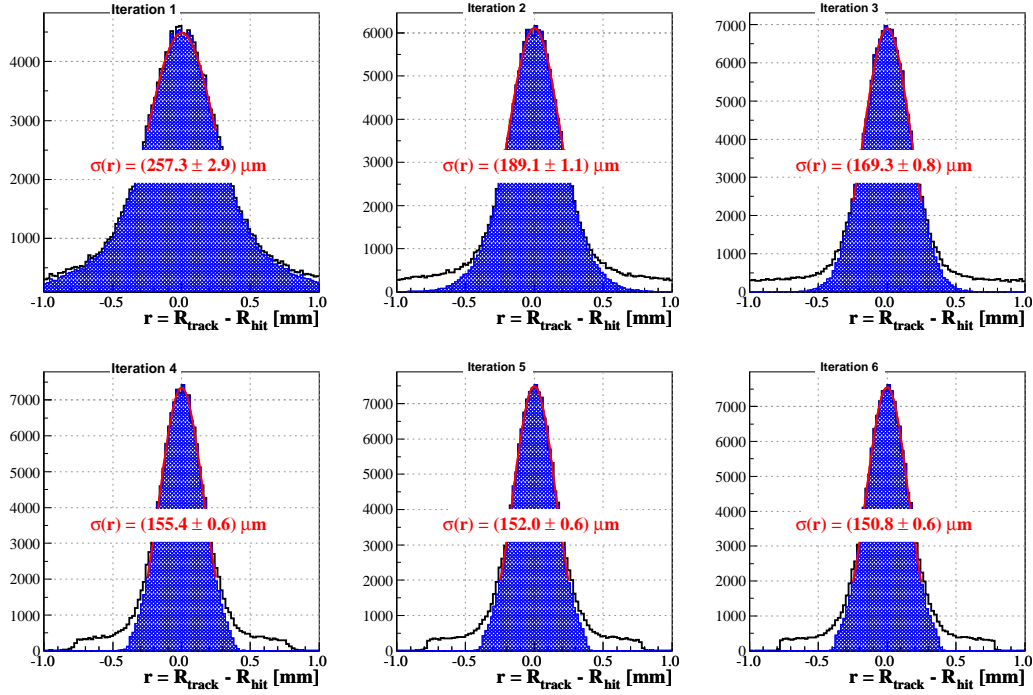


Figure B.4: *Measurement residuals in the TRT in course of the annealing iterations with small outlier cut:* Residuals $r = R_{\text{track}} - R_{\text{measurement}}$ for 3 GeV muon tracks using the modified normalization with $\sqrt{\lambda} = 1.6448$. The histograms are related to the iterations $T = 81 \rightarrow 9 \rightarrow 4 \rightarrow 1 \rightarrow 1 \rightarrow 1$. The black line corresponds to all groups of competing measurements (using the measurement with highest assignment probability for each group), even the ones downweighted by the DAF and the shaded area to groups with $\sum_i p_k^i > 0.2$ (in contrast to figure 6.16 where $\sum_i p_k^i > 0.5$ was used).

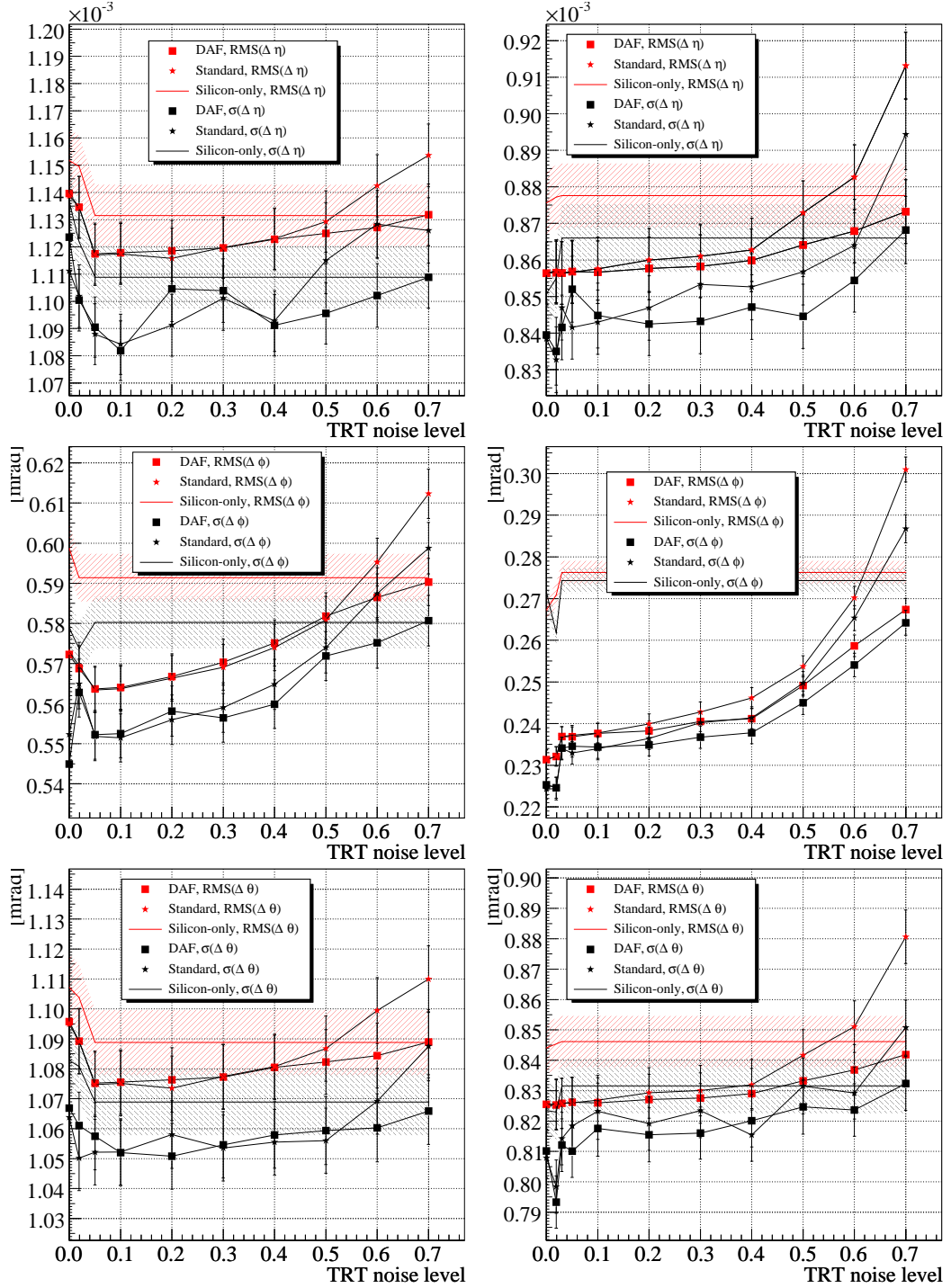


Figure B.5: *Track parameter resolution vs. TRT occupancy I:* The track parameter resolutions of η , ϕ and θ are given as standard deviation of a Gaussian fit and root mean square (RMS) for 3 GeV muon tracks (left) and 10 GeV muon tracks (right) using $\sqrt{\lambda} = 1.96$ and modified normalization. A noise occupancy of $\rho_{\text{Pixel}} = 0.001\%$ in the Pixels and $\rho_{\text{SCT}} = 0.10\%$ in the SCT was used for all values of the TRT noise occupancy, besides the nominal value of $\rho_{\text{TRT}} = 1.9\%$ where $\rho_{\text{Pixel}} = 0.001\%$ and $\rho_{\text{SCT}} = 0.05\%$ was used and the simulation without noise ($\rho_{\text{TRT}} = \rho_{\text{Pixel}} = \rho_{\text{SCT}} = 0.0\%$).

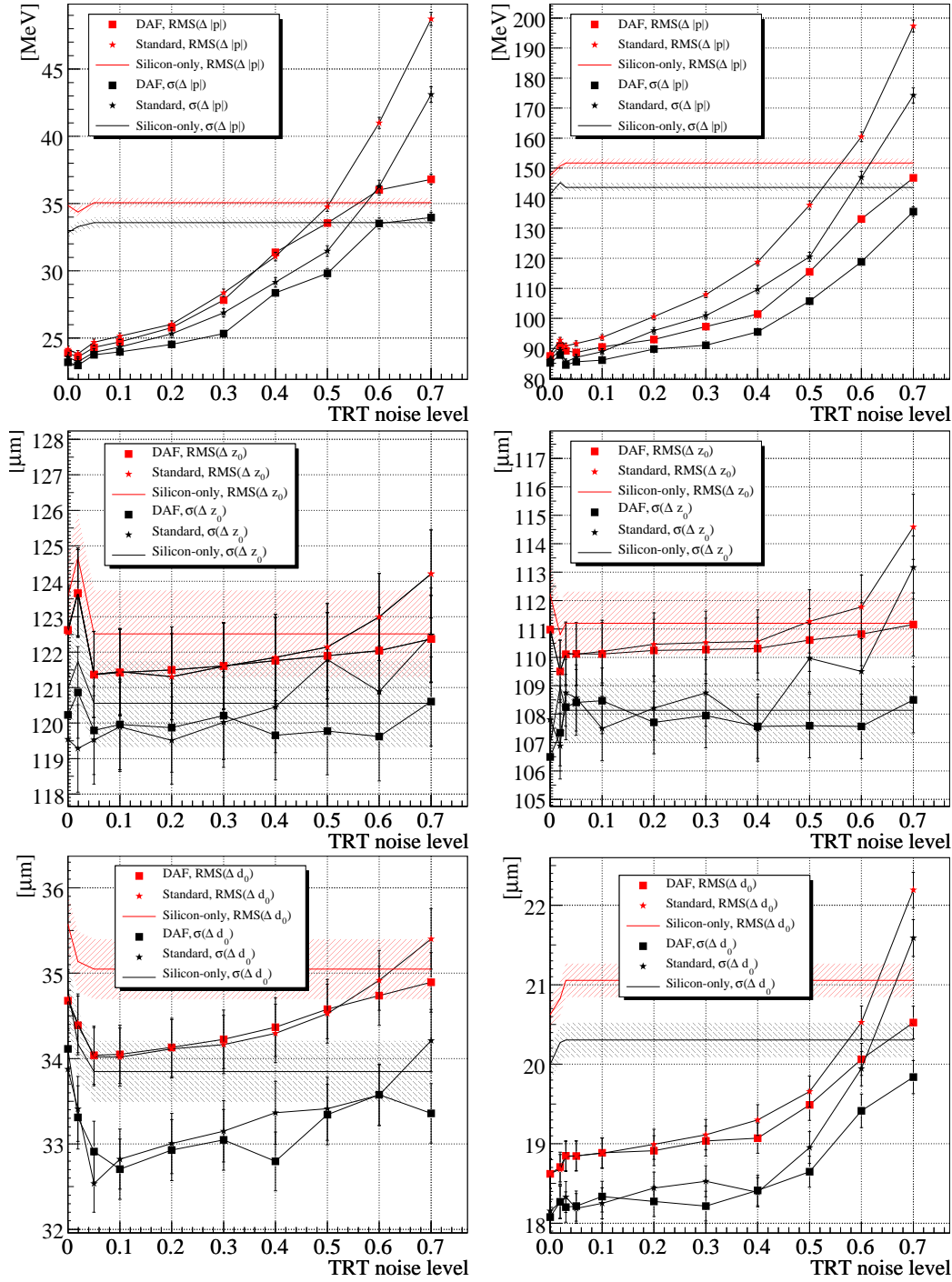


Figure B.6: *Track parameter resolution vs. TRT occupancy II:* The track parameter resolutions of p , z_0 and d_0 are given as standard deviation of a Gaussian fit and root mean square (RMS) for 3 GeV muon tracks (left) and 10 GeV muon tracks (right) using $\sqrt{\lambda} = 1.96$ and modified normalization. A noise occupancy of $\rho_{\text{Pixel}} = 0.001\%$ in the Pixels and $\rho_{\text{SCT}} = 0.10\%$ in the SCT was used for all values of the TRT noise occupancy, besides the nominal value of $\rho_{\text{TRT}} = 1.9\%$ where $\rho_{\text{Pixel}} = 0.001\%$ and $\rho_{\text{SCT}} = 0.05\%$ was used and the simulation without noise ($\rho_{\text{TRT}} = \rho_{\text{Pixel}} = \rho_{\text{SCT}} = 0.0\%$).

C Reference of the developed ATHENA packages

This chapter provides a short reference of the different packages of the ATLAS reconstruction software ATHENA developed within the course of this thesis.

C.1 Reconstruction algorithms

C.1.1 TrkDeterministicAnnealingFilter

The `TrkDeterministicAnnealingFilter` package implements the deterministic annealing filtering technique for track fitting, as proposed by Frühwirth and Strandlie [FS99].

This package contains the high-level steering algorithms of the DAF. The actual calculations are performed by several other packages which depend in many cases on detector-dependent knowledge.

The `TrkDeterministicAnnealingFilter` package contains the following classes:

`Trk::DeterministicAnnealingFilter` DAF steering algorithm, prepares the fit and performs the annealing iterations

`Trk::DAF_WeightCalculator` Tool for calculating the assignment probabilities according to the DAF formulae, using equation (4.36) and (4.37).

`Trk::DAF_SimpleWeightCalculator` Tool for calculating the assignment probabilities according to the DAF formulae with modified normalization, equation (4.40).

C.1.2 TRT_TrackExtensionTool_DAF

This package contains a tool to produce a vector of `CompetingTRT_DriftCirclesOnTrack` which can be used by the `InDetExtensionProcessor` to extend silicon tracks into the TRT. `TRT_DriftCircles` lying on a road around the track prediction are chosen and grouped into `CompetingTRT_DriftCirclesOnTrack` containing measurements which are not compatible with each other. The `DeterministicAnnealingFilter` will then decide in an iterative annealing procedure which `TRT_DriftCircleOnTracks` are assigned to the extended track. As the DAF `TRT_TrackExtensionTool` just produces a vector of `MeasurementBase` (resp. `CompetingTRT_DriftCirclesOnTrack`) without

actually deciding which measurements belong to the track (i. e. just doing a course assignment) this tool can only be used in combination with the `Deterministic-AnnealingFilter`.

This tool has two modes of operation. The first (simple) one just groups all measurements (`TRT_DriftCircles`) on a single TRT detector element into the same `CompetingTRT_DriftCirclesOnTrack`. The more sophisticated mode groups measurements on “pseudo-detector surfaces” which are perpendicular to the track prediction for the Barrel part of the track. In the TRT endcaps the measurements are always grouped by the detector elements because polar coordinates in the wheel plane are used. Both modes are almost identical if the tracks are nearly perpendicular to the detector element planes as it is the case for high momentum tracks.

C.1.3 TrkMeasurementUpdater

The `TrkMeasurementUpdater` package implements the core mathematics for Kalman filter-based track fitters. It provides the calculations to add or remove a measurement to/from the state vector of a track. Just the `Trk::KalmanWeightUpdater` was developed in the course of this thesis which is based on existing code of the `Trk::KalmanUpdater` developed by Wolfgang Liebig and Markus Elsing. The weighted means formalism was implemented additionally, because it is more appropriate for the DAF, which is using the weight matrices instead of the covariance matrices.

The `TrkMeasurementUpdater` package contains the following classes:

`Trk::KalmanUpdater` Measurement updater using gain matrix formalism (see section A.1)

`Trk::KalmanWeightUpdater` Measurement updater using weighted means formalism (see section 4.3.2)

C.2 Event Data Model classes and their related tools

C.2.1 TrkCompetingRIOsOnTrack

This package contains the base class for all `CompetingRIOsOnTrack` that extends the `Trk::MeasurementBase` class.

This class is used by the Deterministic Annealing Filter to handle several `RIO_OnTracks` on one “effective detector layer” (might be more than one `DetectorElement`), which compete against each other in being assigned to a track. The main functions `localParameters()` and `localErrorMatrix()` defined by the base class return the mean values according to the weights (assignment probabilities). `CompetingRIOsOnTrack` are characterized by a vector of `Trk::RIO_OnTrack` objects they hold, by

a `Surface` the `CompetingRIOsOnTrack` is expressed to and a vector of assignment probabilities.

The `TrkCompetingRIOsOnTrack` package contains the following class:

`Trk::CompetingRIOsOnTrack` abstract base class for all `CompetingRIOsOnTrack` implementations

C.2.2 TrkCompetingRIOsOnTrackTool

This package contains the tools to create `Trk::CompetingRIOsOnTrack`. This includes creation of the `RIO_OnTrack` objects with the corresponding tools. The actual calculations are not done in this package, but are delegated to the detector-specific packages, i. e. this tool just acts as a wrapper.

The `TrkCompetingRIOsOnTrackTool` package contains the following classes:

`Trk::ICompetingRIOsOnTrackTool` Interface class for `CompetingRIOsOnTrackTools`.

`Trk::CompetingRIOsOnTrackTool` creates `Trk::CompetingRIOsOnTrack` objects using a given track hypothesis and a list of `Trk::PrepRawData` using the detector specific sub-tool. The tool also allows to update the assignment probabilities of a given `Trk::CompetingRIOsOnTrack`.

`Trk::IWeightCalculator` Interface class for `WeightCalculators`, which compute the assignment probabilities of competing measurements to a track.

C.2.3 InDetCompetingRIOsOnTrack

This package contains the Inner Detector classes which inherit from `CompetingRIOsOnTrack` that extends the `MeasurementBase` class.

The `InDetCompetingRIOsOnTrack` package contains the following classes:

`InDet::CompetingPixelClustersOnTrack` Pixel specific implementation of `CompetingRIOsOnTrack` containing `PixelClusterOnTrack`

`InDet::CompetingSCT_ClustersOnTrack` SCT specific implementation of `CompetingRIOsOnTrack` containing `SCT_ClusterOnTrack`

`InDet::CompetingTRT_DriftCirclesOnTrack` TRT specific implementation of `CompetingRIOsOnTrack` containing `TRT_DriftCircleOnTrack`

C.2.4 InDetCompetingRIOsOnTrackTool

This package contains the tools to create `Trk::CompetingRIOsOnTrack` for the `InDet` realm (i.e. `InDet::CompetingTRT_DriftCirclesOnTrack`, `InDet::CompetingPixelClustersOnTrack`). This includes creation of the `RIO_OnTrack` objects with the corresponding tools.

The `InDetCompetingRIOsOnTrackTool` package contains the following classes:

`InDet::ICompetingPixelClustersOnTrackCreator` Interface class for `CompetingPixelClustersOnTrackTools`.

`InDet::ICompetingSCT_ClustersOnTrackCreator` Interface for `CompetingSCT_ClustersOnTrackTools`.

`InDet::ICompetingTRT_DriftCirclesOnTrackCreator` Interface class for `CompetingTRT_DriftCirclesOnTrackTools`.

`InDet::CompetingPixelClustersOnTrackTool` creates `CompetingPixelClustersOnTrack` objects using a given track hypothesis and a list of `PixelCluster` (given as `PrepRawData`). It creates the `PixelClusterOnTrack` objects with the `PixelClusterOnTrackTool`. All `PixelCluster` have to belong to the same detector element.

`InDet::CompetingSCT_ClustersOnTrackTool` creates the `CompetingSCT_ClustersOnTrack` objects using a given track hypothesis and a list of `SCT_Cluster`. All `SCT_Cluster` have to belong to the same detector element.

`InDet::CompetingTRT_DriftCirclesOnTrackTool` creates `CompetingTRT_DriftCirclesOnTrack` objects using a given track hypothesis and a list of `TRT_DriftCircles` (given as `PrepRawData`). It creates the `TRT_DriftCircleOnTrack` objects with the `TRT_DriftCircleOnTrackTool`. From each `TRT_DriftCircle` (RIO) two `TRT_DriftCircleOnTrack` (ROTs) are created. This corresponds to the left and the right solution of the `DriftCircle`.

C.3 Validation tools

C.3.1 TrkValInterfaces

This package contains the interfaces for common tracking validation tools.

`Trk::IValidationNtupleTool` Interface for main validation ntuple tools which steer `Trk::IValidationNtupleHelperTools`.

`Trk::IValidationNtupleHelperTool` Interface for helper tools which add special data to the validation ntuple.

Trk::IResidualPullCalculator Interface for residual and pull calculation tools.

Trk::ITrackDiff Interface for track diff tools.

C.3.2 TrkValAlgs

This package contains algorithms to validate the common tracking. This includes an algorithm to fill validation ntuples with track data. The algorithm is based on the tools in the **TrkValTools** package.

The following classes of the **TrkValAlgs** package were developed within this thesis (other classes not related to this thesis are not listed):

Trk::TrackValidationNtupleWriter Algorithm for filling a validation ntuple with Track information using **IValidationNtupleTools**. It retrieves a track collection from **StoreGate** and loops over all contained tracks.

Trk::SingleTrackDiffAlg Algorithm for a simple track diff. The **ITrackDiff** tool is used to perform the comparison. This algorithm can just be used for single track events, because only the first track of the reference collection will be compared with the best matching track of the comparison collection.

C.3.3 TrkValTools

This package contains tools to validate the common tracking. This includes tools to fill validation ntuples e. g. with track data. The scheme for filling the ntuple is based on track-wise entries. Every instance of the steering tool (**Trk::BasicValidationNtupleTool**) can fill an own ntuple tree (also in the same ntuple file). This allows to produce one tree e.g. with track data from pattern recognition or simplified simulation and one tree with refitted tracks to compare them with ROOT afterwards. The ntuples created with the tools of this package can be used by the stand-alone ROOT application **TrackPlotter** which is also distributed with this package. The **TrackPlotter** allows to plot the track and measurement positions in the Inner Detector to check the performance of track fitters track by track. A tool for the calculation of residuals and pulls of measurements is also provided by this package.

Validation ntuple scheme

The main steering of the ntuple entries is performed by the **Trk::BasicValidationNtupleTool**, which can book the ntuple, create the tree directory and add basic entries. This tool is also able to write the current record to the ntuple file and start a new entry. One can also use an existing ntuple tree (which has to have the same track-wise structure) and just use the **Trk::BasicValidationNtupleTool** to add some ntuple variables. Every entry (track) contains the event number, a track ID (numbering the

tracks within one event) and an optional iteration index, which can be used if different intermediate results of a track are produced in the refit procedure (as it is the case for the `Trk::DeterministicAnnealingFilter`). The track ID is the same for all tracks generated within one iteration process and reset to 0 every time a new event is started. Perigee parameters and χ^2 are filled for every track if available.

For fitter validation information about the measurements on the track and the related track states is especially needed. Therefore the total number of measurements on the track and the numbers of measurements within a certain sub-detector type are stored. The tool writes array variables with columns for every measurement into the ntuple. One can provide a list of `IValidationNtupleHelperTool` for each detector type by job options which are called by the `BasicValidationNtupleTool` if a measurement of the related detector is found on the track. Those `IValidationNtupleHelperTools` can add items to the ntuple and fill special data needed for validation. The `IValidationNtupleHelperTools` may also reside in a detector-specific namespace (e. g. `lnDetFitterValidation`) to be able to add information which need a dynamic cast of the `MeasurementBase` to the specific implementations.

Each list of detector-specific helper tools may contain several tools and some tools may even be contained in more than one list, if they fill data for different detector types. There exists also a general list, which tools are called for every type of measurement.

The `TrkValTools` package contains the following classes:

`Trk::BasicValidationNtupleTool` Tool to fill basic information about a track into a ntuple. Calls given `IValidationNtupleHelperTools` to write special data.

`Trk::ResidualValidationNtupleHelper` Helper tool for the `BasicValidationNtupleTool` which writes residual and pull information for Pixels, SCT and TRT using the `ResidualPullCalculator`.

`Trk::HitPositionNtupleHelper` Helper tool for the `BasicValidationNtupleTool` which writes statistics about measurement and surface positions.

`Trk::TrackPositionNtupleHelper` Helper tool for the `BasicValidationNtupleTool` which writes information about track positions.

`Trk::DAF_ValidationNtupleHelper` Helper tool for the `BasicValidationNtupleTool` which writes data from `CompetingRIOsOnTrack`.

`Trk::ResidualPullCalculator` Tool for the calculation of residuals and pulls. Detector-specific specialties like the SCT endcap residuals are taken into account by calling tools in the sub-detector realm.

`Trk::ResidualPull` Output class of the `ResidualPullCalculator`. Beside the values of residual and pull this class stores information about the type of the residual (unbiased/biased, etc.).

Trk::TrackDiff Tool to compare two tracks (e. g. simulated and reconstructed track). Differences in the **TrackStateOnSurfaces** are listed in the messages and a summary for each track is written to a ntuple.

The most convenient way to use the validation ntuple tools is to run the **TrackValidationNtupleWriter** algorithm from the **TrkValAlgs** package, which retrieves a track collection from **StoreGate** and loops over all contained tracks. It needs a configured instance of the **BasicValidationNtupleTool**. It is also possible to run the **BasicValidationNtupleTool** directly by calling it from other algorithms or tools to write data of complete tracks or to add data of measurements successively. An example for this use case is the **DeterministicAnnealingFilter** which uses the validation tools to write data from each annealing iteration to a ROOT ntuple.

C.3.4 InDetTrackValidation

This package contains tools to validate the tracking in the Inner Detector. This includes tools to fill validation ntuples e. g. with measurement data and a tool for the calculation of SCT residuals and pulls.

The **InDetTrackValidation** package contains the following classes:

InDet::TRT_DriftTimeNtupleHelper Helper tool for the **BasicValidationNtupleTool** which writes measurement data for the TRT (i. e. data from **TRT_DriftCircles** and **TRT_DriftCircleOnTrack**).

InDet::SCT_ResidualPullCalculator Sub-detector specific tool for the **ResidualPullCalculator**. For the "artificially" two-dimensional SCT measurements in the endcap modules the coordinates and covariance matrices are rotated to return the residual perpendicular to the strip.

InDet::SCT_ClusterValidationNtupleWriter Algorithm to write the positions of **SCT_Clusters** into a ROOT ntuple. It is needed for the **TrackPlotter** to visualize the position of SCT measurements which are not assigned to a track.

InDet::TRT_DriftCircleValidationNtupleWriter Algorithm to write information about **TRT_DriftCircles** into a ROOT ntuple. The **TrackPlotter** can use this data to visualize the position of TRT measurements which are not assigned to a track.

C.4 *fatRas* simulation

The packages of the *fatRas* simulation will not be described in detail here, because the *fatRas* packages will be restructured. Just the algorithms with contributions in the course of this thesis will be briefly presented in the following.

- InDet::MC_TrackCreator** One of the core classes of fatRas. The measurements are created according to the extrapolated track positions by this tool including measurement smearing (see section 5.5.1). Measurements and track parameters are translated into a **Track**.
- InDet::MC_PostProcessor** Algorithm for the extraction of raw measurements from the simulated tracks. The measurements are collected from all tracks in an event and sorted according to the sub-detector type.
- InDet::MC_PixelPostProcessor** Tool to sort **PixelClusters** into **PrepRawDataCollections** and for noise creation in the Pixel layers.
- InDet::MC_SCT_PostProcessor** Tool to sort **SCT_Clusters** into **PrepRawDataCollections** and for noise creation in the SCT layers.
- InDet::MC_TRT_PostProcessor** This tool sorts **TRT_DriftCircles** and eliminates multiple measurements in the same TRT tube. Noise is created which can mask **TRT_DriftCircles** from the track simulation (see section 5.5.2).

List of Figures

3.1	Sketch of the ATLAS detector	8
3.2	Drawing of the ATLAS Inner Detector	9
3.3	Cross-sectional view of the Inner Detector	10
3.4	Barrel TRT module	12
4.1	Histogramming for pattern recognition in the ATLAS TRT	16
4.2	Functional principle of the Kalman filter for track fitting	20
4.3	Track finding with a Combinatorial Kalman Filter	24
4.4	Functional principle of the Deterministic Annealing Filter	27
4.5	Hit selection using Deterministic Annealing	29
5.1	UML diagram of <code>CompetingRIOsOnTrack</code> objects	36
5.2	UML sequence diagram for the <code>DeterministicAnnealingFilter</code>	37
5.3	Strategies for the grouping of mutually exclusive measurements in the barrel TRT	39
5.4	Calculation of the mean measurement in the TRT end-caps	40
5.5	Simplified UML sequence diagram for the fatRas simulation	43
5.6	Track plots of a top event	44
5.7	Track plots ($X - Y$) in the barrel TRT	45
6.1	Distribution of the maximum and minimum assignment probability for each group of competing measurements in the TRT	48
6.2	Drift radius versus maximum assignment probability for each group of competing measurements in the TRT	50
6.3	p_T resolution	51
6.4	Impact of local z -cut on positions of fake measurements in the TRT . .	53
6.5	Impact of extrapolation problems on p_T resolution	55
6.6	Inefficiencies and fake measurements for 2 and 4 mm initial roadwidth .	57
6.7	Inefficiencies and fake measurements vs. initial roadwidth	58
6.8	p_T resolution vs. $\sqrt{\lambda}$ for 3 GeV muon tracks	59
6.9	Generalized variance vs. cut (from [FS99])	60
6.10	Inefficiencies and fake measurements vs. $\sqrt{\lambda}$	61
6.11	Drift radius vs. assignment probability with $\sqrt{\lambda} = 1.6448$	62
6.12	Drift radius vs. assignment probability with $\sqrt{\lambda} = 1.6448$ after last iteration	62

6.13	Drift radius vs. assignment probability after last iteration with modified normalization	63
6.14	p_T resolution vs. $\sqrt{\lambda}$ for 3 GeV muon tracks with modified normalization	63
6.15	Inefficiencies and fakes vs. $\sqrt{\lambda}$ with modified normalization	64
6.16	TRT residuals in annealing iterations	65
6.17	Standard deviation of p_T and d_0 pull vs. $\sqrt{\lambda}$	66
6.18	p_T resolution vs. $\sqrt{\lambda}$ for 10 GeV muon tracks with modified normalization	67
6.19	Standard deviation of p_T and d_0 pull vs. $\sqrt{\lambda}$ for 10 GeV muon tracks .	68
6.20	Inefficiencies and fake measurements for different annealing schemes and 3 GeV muon events	69
6.21	Inefficiencies and fake measurements for different annealing schemes and 10 GeV muon events	70
6.22	p_T resolution for different annealing schemes	71
6.23	p_T resolution vs. TRT occupancy	73
6.24	d_0 resolution vs. TRT occupancy	73
6.25	$1/p_T$ resolution vs. $1/p_T$	75
6.26	$1/p_T$ and d_0 resolution vs. $1/p_T$ for single muon events using full simulation	76
6.27	$1/p_T$ and d_0 resolution vs. $1/p_T$ for inclusive top events using full simulation	77
A.1	Assignment probability for a single measurement	82
A.2	Assignment probability for a one of two measurements	82
A.3	Assignment probability for a one of two measurements (2-dim.)	83
B.1	Inefficiencies and fake measurements vs. $\sqrt{\lambda}$ with different outlier cuts	86
B.2	Inefficiencies and fake measurements vs. $\sqrt{\lambda}$ with different outlier cuts using modified normalization	87
B.3	Standard deviation of p_T and d_0 pull vs. $\sqrt{\lambda}$ using standard normalization	88
B.4	TRT residuals in annealing iterations with small outlier cut	89
B.5	Track parameter resolution vs. TRT occupancy I	90
B.6	Track parameter resolution vs. TRT occupancy II	91

Abbreviations

This list contains the abbreviations used throughout this thesis and references to the pages where those abbreviations are explained in more detail.

- ATLAS A Toroidal Lhc ApparatuS – multi-purpose experiment in high energy physics at the Large Hadron Collider at CERN, page 7
- CERN European Organization for Nuclear Research and European Laboratory for Particle Physics, page 7
- CKF Combinatorial Kalman Filter, page 23
- CMS Compact Muon Solenoid – multi-purpose experiment in high energy physics at the Large Hadron Collider at CERN, page 7
- DAF Deterministic Annealing Filter, page 26
- EAA Elastic Arms Algorithm, page 25
- EDM Event Data Model, page 35
- ETA Elastic Tracking Algorithm, page 25
- fatRas ATLAS **fast track** simulation, page 41
- LEP Large Electron-Positron Collider – former lepton collider at CERN, page 7
- LHC Large Hadron Collider – proton-proton collider at CERN, page 7
- LSM Least Squares Method, page 18
- MTF Multi Track Fitter, page 30
- PRD `PrepRawData` alias `ReconstructionInputObjects`. Data object representing a cluster of `PrepRawData` on a single module (e. g. a cluster of neighboring pixels), page 32
- RDO `RawDataObject`. Data object representing a single measurement (e. g. a single pixel), page 32
- RIO `ReconstructionInputObjects`, other name for `PrepRawData`, see PRD, page 32
- ROT `RIO_OnTrack`. Data object representing a `PrepRawData` being assigned to a track. May include calibrations which are only possible when a track prediction is known, page 33
- RTTI run-time type identification, page 35

List of Figures

SCT Semiconductor Tracker – Part of the Inner Detector of ATLAS , page 11

TRT Transition Radiation Tracker, page 12

Bibliography

- [A⁺04] Torsten Akesson et al. Status of design and construction of the Transition Radiation Tracker (TRT) for the ATLAS experiment at the LHC. *Nuclear Instruments and Methods in Physics Research A*, 522:131–145, April 2004.
- [AAC⁺06] Fredrik Akesson, Tom Atkinson, Maria Jose Costa, Markus Elsing, Sebastian Fleischmann, Andrei Gaponenko, Wolfgang Liebig, Edward Moyse, Andreas Salzburger, and Martin Siebel. Atlas tracking event data model. ATLAS Note ATL-SOFT-PUB-2006-004, ATLAS Collaboration, July 2006.
- [AH03] Ian J. R. Aitchison and Anthony J. G. Hey. *Gauge theories in particle physics*, volume I, From Relativistic Quantum Mechanics to QED of *Graduate student series in physics*. Institute of physics publishing, Bristol, 3rd edition, 2003.
- [AH04] Ian J. R. Aitchison and Anthony J. G. Hey. *Gauge theories in particle physics*, volume II, QCD and the Electroweak Theory of *Graduate student series in physics*. Institute of physics publishing, Bristol, 3rd edition, 2004.
- [ATL96a] *ATLAS Liquid Argon Calorimeter Technical Design Report*, December 1996. CERN/LHCC/96-41.
- [ATL96b] *ATLAS Tile Calorimeter Technical Design Report*, December 1996. CERN/LHCC/96-42.
- [ATL97a] *ATLAS Inner Detector Technical Design Report — Volume I and II*, April 1997. CERN/LHCC/97-16 and CERN/LHCC/97-17.
- [ATL97b] *ATLAS Muon Spectrometer Technical Design Report*, June 1997. CERN/LHCC/97-22.
- [ATL99] *ATLAS Detector and Physics Performance Technical Design Report — Volume II*, May 1999. CERN/LHCC/99-15.
- [ATL04] *Athena – The ATLAS Common Framework – Developer Guide*, February 2004. Version 8.0.0.

- [ATL05] *ATLAS Computing Technical Design Report*, July 2005. CERN/LHCC/2005-022.
- [Cor06] Thijs Cornelissen. CTBTracking: track reconstruction for the testbeam and cosmics. ATLAS Internal Note ATL-INDET-INT-2006-001, ATLAS Collaboration, April 2006.
- [Dre96] Manuel Drees. An Introduction to Supersymmetry. *ArXiv High Energy Physics*, hep-ph/9611409, November 1996.
- [Frü87] Rudolf Frühwirth. Application of Kalman filtering to track and vertex fitting. *Nuclear Instruments and Methods in Physics Research A*, 262:444–450, December 1987.
- [FS99] Rudolf Frühwirth and Are Strandlie. Track fitting with ambiguities and noise: a study of elastic tracking and non-linear filters. *Computer Physics Communications*, 120:197–214, August 1999.
- [FS06] Rudolf Frühwirth and Are Strandlie. Application of adaptive filters to track finding. *Nuclear Instruments and Methods in Physics Research A*, 559:162–166, April 2006.
- [Gel74] Arthur Gelb, editor. *Applied optimal estimation*. The M.I.T. Press, Cambridge, Mass., 1st edition, 1974.
- [GH91] Miklos Gyulassy and Magnus Harlander. Elastic tracking and neural network algorithms for complex pattern recognition. *Computer Physics Communications*, 66:31–46, July 1991.
- [Jac02] John David Jackson. *Klassische Elektrodynamik*. De Gruyter, Berlin, 3. edition, 2002.
- [Lin95] Magnus Lindström. Track reconstruction in the ATLAS detector using elastic arms. *Nuclear Instruments and Methods in Physics Research A*, 357:129–149, February 1995.
- [Man97] Rainer Mankel. A concurrent track evolution algorithm for pattern recognition in the HERA-B main tracking system. *Nuclear Instruments and Methods in Physics Research A*, 395:169–184, February 1997.
- [Man04] Rainer Mankel. Pattern recognition and event reconstruction in particle physics experiments. *Reports of Progress in Physics*, 67:553–622, April 2004.

- [OPY92] Mattias Ohlsson, Carsten Peterson, and Alan L. Yuille. Track finding with deformable templates — the elastic arms approach. *Computer Physics Communications*, 71:77–98, August 1992.
- [RF00] Meinhard Regler and Rudolf Frühwirth, editors. *Data Analysis Techniques for High-Energy Physics*. Number 11 in Cambridge Monographs on Particle Physics, Nuclear Physics and Cosmology. Cambridge University Press, Cambridge, 2nd edition, 2000.
- [Sal04] Andreas Salzburger. The track extrapolation package in the new ATLAS tracking realm. In *Proceedings of the CHEP04 conference*, Interlaken, September 2004.
- [SF00] Are Strandlie and Rudolf Frühwirth. Adaptive multitrack fitting. *Computer Physics Communications*, 133:34–42, December 2000.
- [Str] Are Strandlie. Private communication.
- [SWFL06] Andreas Salzburger, Andreas Wildauer, Sebastian Fleischmann, and Tatjana Lenz. The new ATLAS fast track simulation engine (fatras). In *Proceedings of the CHEP06 conference*, Mumbai, February 2006.
- [SZ99] Are Strandlie and Josiane Zerubia. Particle tracking with iterated Kalman filters and smoothers: the PMHT algorithm. *Computer Physics Communications*, 123:77–86, December 1999.
- [Y⁺06] W.-M. Yao et al. Review of Particle Physics. *Journal of Physics G*, 33:1+, 2006.